IEC TR 61000-2-15

Edition 1.0 2023-02

TECHNICAL REPORT

colour inside

Electromagnetic compatibility –
Part 2-15: Description of the characteristics of networks with high penetration of power electronic converters

IEC TR 61000-2-15:2023-02(en)

IEC Secretariat
3, rue de Varembé
CH-1211 Geneva 20
Switzerland

Tel.: +41 22 919 02 11
info@iec.ch
www.iec.ch

About the IEC
The International Electrotechnical Commission (IEC) is the leading global organization that prepares and publishes International Standards for all electrical, electronic and related technologies.

About IEC publications
The technical content of IEC publications is kept under constant review by the IEC. Please make sure that you have the latest edition, a corrigendum or an amendment might have been published.

IEC publications search - webstore.iec.ch/advsearchform
The advanced search enables to find IEC publications by a variety of criteria (reference number, text, technical committee, …). It also gives information on projects, replaced and withdrawn publications.

IEC Just Published - webstore.iec.ch/justpublished
Stay up to date on all new IEC publications. Just Published details all new publications released. Available online and once a month by email.

IEC Customer Service Centre - webstore.iec.ch/csc
If you wish to give us your feedback on this publication or need further assistance, please contact the Customer Service Centre: sales@iec.ch.

IEC Products & Services Portal - products.iec.ch
Discover our powerful search engine and read freely all the publications previews. With a subscription you will always have access to up to date content tailored to your needs.

Electropedia - www.electropedia.org
The world's leading online dictionary on electrotechnology, containing more than 22 300 terminological entries in English and French, with equivalent terms in 19 additional languages. Also known as the International Electrotechnical Vocabulary (IEV) online.

IEC TR 61000-2-15

Edition 1.0 2023-02

TECHNICAL REPORT

colour inside

Electromagnetic compatibility –
Part 2-15: Description of the characteristics of networks with high penetration of power electronic converters

INTERNATIONAL
ELECTROTECHNICAL
COMMISSION

ICS 29.240.01; 33.100.01

ISBN 978-2-8322-6550-5

CONTENTS

INTERNATIONAL ELECTROTECHNICAL COMMISSION

_____

ELECTROMAGNETIC COMPATIBILITY –

Part 2-15: Description of the characteristics of networks with high penetration of power electronic converters

FOREWORD

1) The International Electrotechnical Commission (IEC) is a worldwide organization for standardization comprising all national electrotechnical committees (IEC National Committees). The object of IEC is to promote international co-operation on all questions concerning standardization in the electrical and electronic fields. To this end and in addition to other activities, IEC publishes International Standards, Technical Specifications, Technical Reports, Publicly Available Specifications (PAS) and Guides (hereafter referred to as "IEC Publication(s)"). Their preparation is entrusted to technical committees; any IEC National Committee interested in the subject dealt with may participate in this preparatory work. International, governmental and non-governmental organizations liaising with the IEC also participate in this preparation. IEC collaborates closely with the International Organization for Standardization (ISO) in accordance with conditions determined by agreement between the two organizations.
2) The formal decisions or agreements of IEC on technical matters express, as nearly as possible, an international consensus of opinion on the relevant subjects since each technical committee has representation from all interested IEC National Committees.
3) IEC Publications have the form of recommendations for international use and are accepted by IEC National Committees in that sense. While all reasonable efforts are made to ensure that the technical content of IEC Publications is accurate, IEC cannot be held responsible for the way in which they are used or for any misinterpretation by any end user.
4) In order to promote international uniformity, IEC National Committees undertake to apply IEC Publications transparently to the maximum extent possible in their national and regional publications. Any divergence between any IEC Publication and the corresponding national or regional publication shall be clearly indicated in the latter.
5) IEC itself does not provide any attestation of conformity. Independent certification bodies provide conformity assessment services and, in some areas, access to IEC marks of conformity. IEC is not responsible for any services carried out by independent certification bodies.
6) All users should ensure that they have the latest edition of this publication.
7) No liability shall attach to IEC or its directors, employees, servants or agents including individual experts and members of its technical committees and IEC National Committees for any personal injury, property damage or other damage of any nature whatsoever, whether direct or indirect, or for costs (including legal fees) and expenses arising out of the publication, use of, or reliance upon, this IEC Publication or any other IEC Publications.
8) Attention is drawn to the Normative references cited in this publication. Use of the referenced publications is indispensable for the correct application of this publication.
9) Attention is drawn to the possibility that some of the elements of this IEC Publication may be the subject of patent rights. IEC shall not be held responsible for identifying any or all such patent rights.

IEC TR 61000-2-15 has been prepared by subcommittee 77A: EMC – Low frequency phenomena, of IEC technical committee 77: Electromagnetic compatibility. It is a Technical Report.

The text of this Technical Report is based on the following documents:

Draft	Report on voting
77A/1153A/DTR	77A/1159/RVDTR

Full information on the voting for its approval can be found in the report on voting indicated in the above table.

The language used for the development of this Technical Report is English.

This document was drafted in accordance with ISO/IEC Directives, Part 2, and developed in accordance with ISO/IEC Directives, Part 1 and ISO/IEC Directives, IEC Supplement, available at www.iec.ch/members_experts/refdocs. The main document types developed by IEC are described in greater detail at www.iec.ch/publications.

A list of all parts in the IEC 61000 series, published under the general title *Electromagnetic compatibility*, can be found on the IEC website.

The committee has decided that the contents of this document will remain unchanged until the stability date indicated on the IEC website under webstore.iec.ch in the data related to the specific document. At this date, the document will be

- reconfirmed,
- withdrawn,
- replaced by a revised edition, or
- amended.

IMPORTANT – The "colour inside" logo on the cover page of this document indicates that it contains colours which are considered to be useful for the correct understanding of its contents. Users should therefore print this document using a colour printer.

INTRODUCTION

IEC 61000 is published in separate parts according to the following structure:

Part 1: General

General considerations (introduction, fundamental principles)

Definitions, terminology

Part 2: Environment

Description of the environment

Classification of the environment

Compatibility levels

Part 3: Limits

Emission limits

Immunity limits (insofar as these limits do not fall under the responsibility of the product committees)

Part 4: Testing and measurement techniques

Measurement techniques

Testing techniques

Part 5: Installation and mitigation guidelines

Installation guidelines

Mitigation methods and devices

Part 6: Generic standards

Part 9: Miscellaneous

Each part is further subdivided into several parts, published either as international standards or as technical specifications or technical reports, some of which have already been published as sections. Others will be published with the part number followed by a dash and a second number identifying the subdivision (example: IEC 61000-6-1).

This part of IEC 61000-2 describes the main phenomena which affect the power quality of modern distribution systems with high penetration of power electronics converters.

It focuses on the following main aspects: resonances in LV network, impact of increased number of power electronic converters, instability issues for the equipment to be connected to the LV networks.

Those new aspects, organized and described in this document, can lead to new IEC specifications; that is why a state of the art on this topic is necessary.

ELECTROMAGNETIC COMPATIBILITY –

Part 2-15: Description of the characteristics of networks with high penetration of power electronic converters

1 Scope

This part of IEC 61000, which is a Technical Report, addresses in particular the following main phenomena, which affect the power quality in modern distribution systems with high penetration of power electronics converters. As some aspects of the subject have already been addressed in the past, considering the evolution of the LV and MV networks, this document focuses on the following aspects:

- resonances in the network, modelling and on-site validation;
- supraharmonics and measurements issues;
- impact of increased number of power electronic converters;
- stability and instability issues for the equipment to be connected

The target phenomena and conditions of this document are the following:

- frequency: ≤ 2 kHz, 2 kHz to 9 kHz, ≥ 9 kHz;
- voltage levels: LV, MV;
- harmonic sources: all types of converters (EV battery chargers, appliances, etc.…).

Some of these frequency ranges have already been standardized in some countries (Japan, Germany, Switzerland, etc.), but the resulting phenomena developed will benefit being described in more details, with a focus on the interaction between the converters and the electrical networks. The case of the presence of a large number of converters is also at stake. Some complex phenomena can also arise when the full system is not stable anymore.

NOTE Whereas it is expected that the models and derived calculations form this document can be applied to the Americas electrical systems its formal validation studies are still pending.

2 Normative references

There are no normative references in this document.

3 Terms and definitions

No terms and definitions are listed in this document.

ISO and IEC maintain terminology databases for use in standardization at the following addresses:

- IEC Electropedia: available at https://www.electropedia.org/
- ISO Online browsing platform: available at https://www.iso.org/obp

4 Resonance phenomena with network and power electronics equipment based on actual cases

4.1 Operation of overvoltage protection of earth leakage circuit breaker in Japanese LV systems

4.1.1 General

- Overview

  In Japanese LV systems, power outages due to the operation of the earth leakage circuit breaker (ELCB) with an overvoltage protection function, and due to the abnormal acoustic noises generated by peripheral appliances can occur when particular appliances with power electronics technologies are operating [1][1].

  In some cases, the overvoltages exceed the rated voltage in the same LV system, caused by harmonics within the frequency band of 2 kHz to 9 kHz in the LV line.

  As a result of investigating these phenomena through verification tests and simulations, the overvoltage was confirmed as attributable to a harmonic resonance between the harmonic current produced by the power electronics appliance and the network circuit including the MV/LV transformer inductance, the LV line inductance and the line capacitances with peripheral appliances. These resonance phenomena are also addressed in [7] [27].

  The case is addressed in detail in the following paragraphs, and other cases are mentioned in 4.2.

- Description of the conditions and their verification

  In Figure 1, when a particular power electronics appliance in a home (source) connected to a public LV system is in operation [1], an ELCB in another home (neighbour) connected to the same LV system acted and trips or acoustic noise from appliances occurred. The ELCB has functions not only to detect the earth leakage current but also to protect against overvoltages. That overvoltage protection operates when its amplitude exceeds 130 % of the nominal voltage.

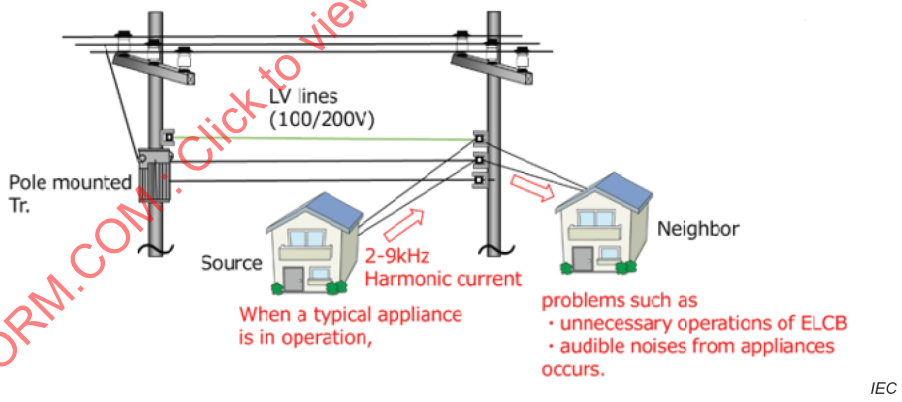

Figure 1 – Schematic illustration of a harmonic resonance issue in a LV system

The peak voltage in the waveform given by Figure 2 [1] exceeds 141 V_p of the normal peak voltage at 100 V_{rms} and includes harmonics in the higher frequency band. The overvoltage level at the neighbour location is higher than the one at the source because of a harmonic resonance.

[1] Numbers in square brackets refer to the Bibliography.

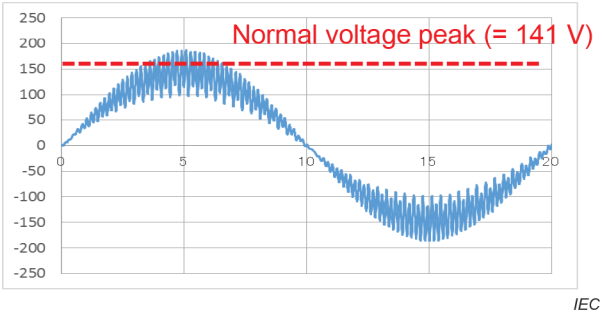

Figure 2 – Waveform of the overvoltage at the neighbour side

4.1.2 Circuit modelling

In Figure 3, the equivalent circuit of this parallel resonance consists of a harmonic current source I_n with a particular power electronics appliance, an MV/LV transformer inductance L_{tr}, an LV distributed line inductance L_{line}, a phase-to-phase capacitance C_0 connected to the appliance at the source side and a C_1 connected to appliances at the neighbour side. The voltage at the neighbor side is given by V_c as shown in Figure 2 [1].

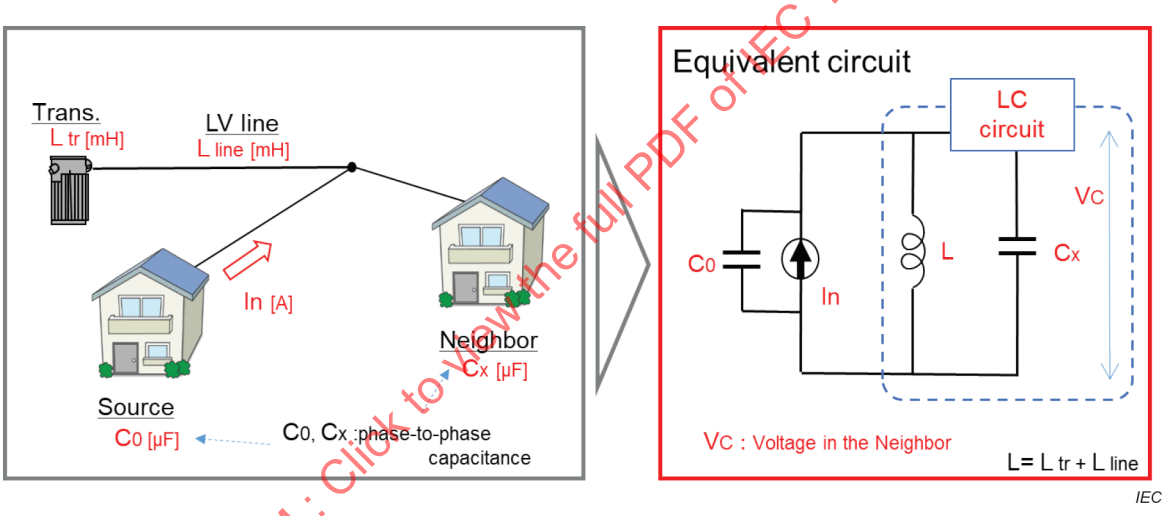

Figure 3 – Description of an equivalent circuit modelling for harmonic resonances

- Determination of the frequency dependent grid impedance (FdGI)

  From the equivalent circuit of an L, C parallel resonance, the resonance magnification factors (RMFs) (V/A) have been determined by simulations [1]. It can be seen in Figure 4 , using the frequency dependent impedance with the inductance of the LV system and the capacitor of the phase-to-phase capacitances with appliances.

  As the analytical parameters are in the frequency range from 2 kHz to 9 kHz, C_0 = 0,1～1 000 μF and L_0 = 50 mH～1 000 mH, are used on the source side with the power electronics appliance and C_1 = 1 μF～2 0 μF is used on the neighbour side corresponding to the damaged equipment. The voltage when given by a current source of 1 A in the frequency band is defined as RMF.

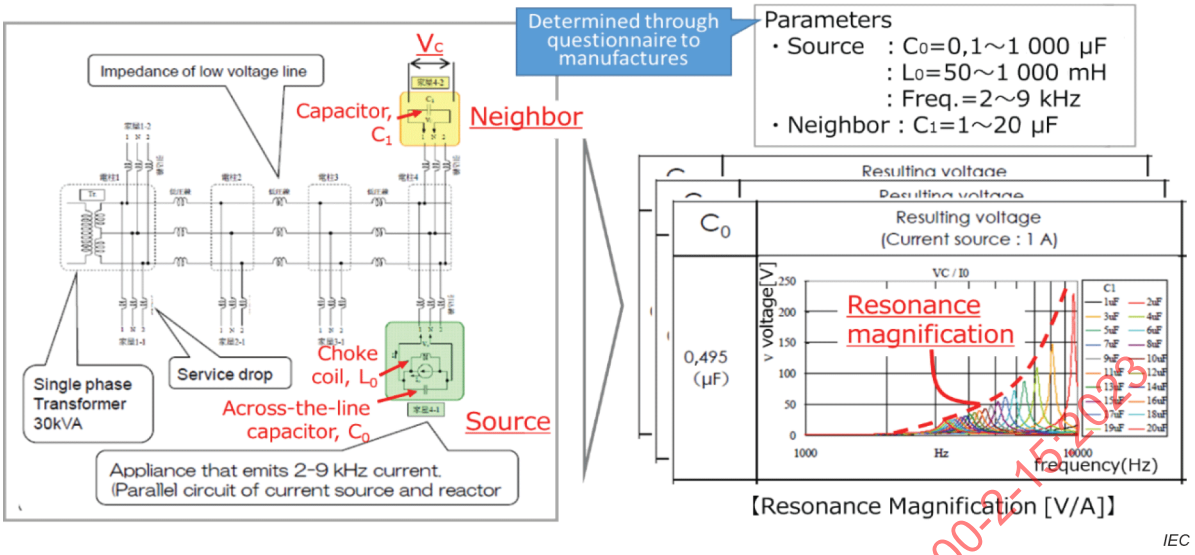

Figure 4 – Electrical circuit used in simulations, and results of resonance magnification factors (RMFs)

4.1.3 Measurements on site

The experimental tests which simulate the impedance of a typical LV system are performed in order to reproduce these resonance phenomena [1]. The capacitors at the connection point assumed for each household are connected to the emitted and the damaged devices, respectively, in Figure 5. In those tests, an appliance emitting harmonics at a terminal house and capacitors simulating the appliances of other houses are connected to the LV system. The voltages and currents at each connection point have been measured.

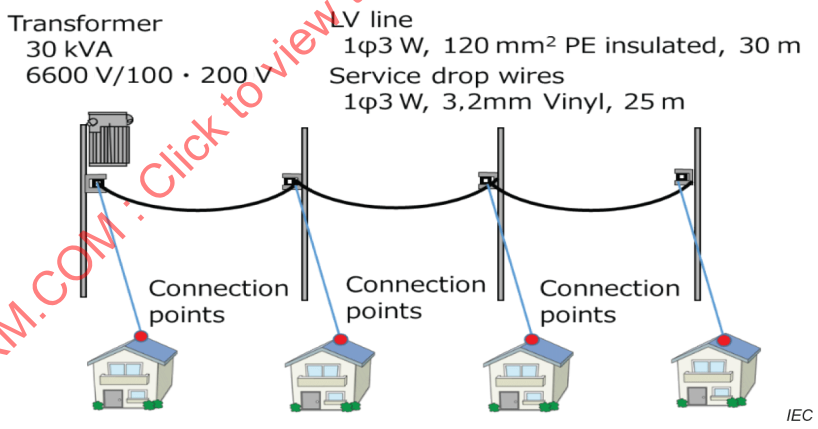

Figure 5 – Description of the experimental test configuration

As measured on site [1], a high-order harmonic voltage propagates to all the devices connected to the same system as the source. The resonance conditions depend on the impedance characteristics, so that the voltages are different depending on the measured location as shown in Figure 6:

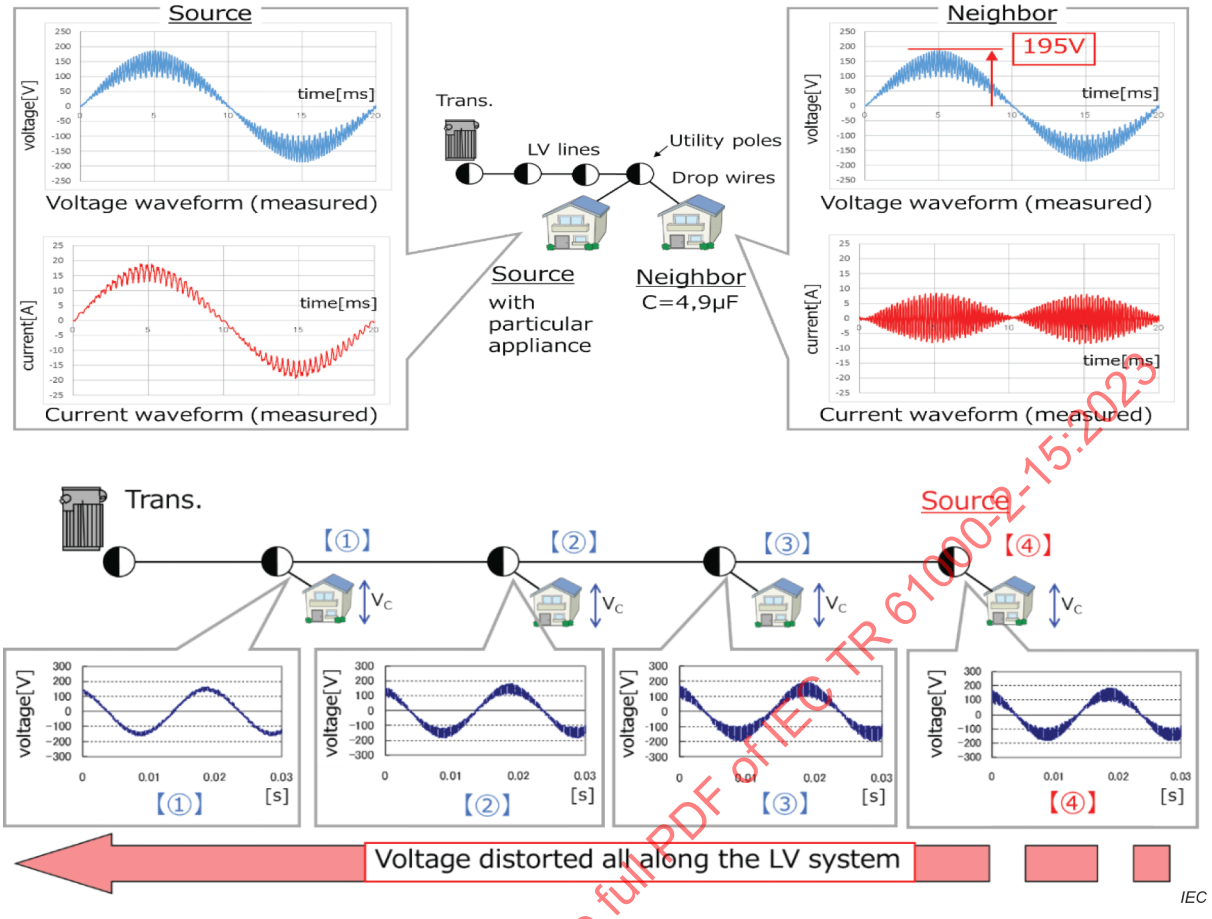

Figure 6 – Measurement performed during the experimental tests

In Figure 7, the voltage peak measured on site and the one obtained by simulation, under the same conditions, are in good agreement with a peak value equal to 65 V at 4,5 kHz [1].

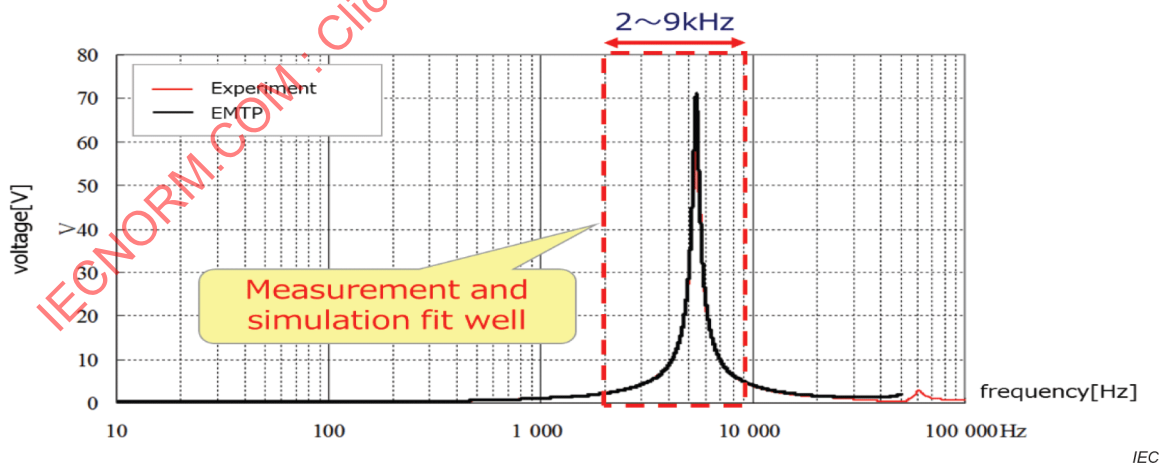

Figure 7 – Resonance magnification factors (RMFs) using measurement and simulation

The line resistances in the experimental LV system are considered as similar to those in the real LV system. However, the resistance loads contributing to the damping are not considered because there are many LV systems with almost no load.

4.1.4 Technical or regulatory aspects

To establish countermeasures for these issues, the Japanese Industrial Standard on Technical Specifications JIS TS C 0058 [2] stipulates the emission limit values and assessment methods for harmonic currents in the range of 2 kHz to 9 kHz.

Reference [2] is intended to prevent the performance degradation and disturbances of other electric or electronic devices connected to public LV distribution system. The current emission limits of 2 kHz to 9 kHz are determined so that the voltage distortion does not exceed the immunity level of appliances. In addition, the overvoltage level is assumed by multiplying the harmonic current (A) by the resonance magnification factor (V/A).

The emission limits are calculated by using the capacity of the phase-to-phase capacitance built into the EUT (equipment under test) as a parameter. The measurement value would be lower than this limit value for each frequency of harmonics. The emission limit of the EUT that causes trouble is converted from “current value” to “power value” and can be assessed from the EUT design information (inverter control method, maximum input power, line capacitor capacity).

The flowchart in Figure 8 shows two types of assessments: “Design assessment” and “Measurement assessment” in order to reduce the cost for manufacturers. “Design assessment” is adopted so that the appliance complying with [2] can be assessed from the design information of the EUT to know in advance without measurements the switching frequency, the capacitance C_0 of the phase-to-phase capacitance with or without the interleaved mode. For instance, in the case where the switching frequency of the EUT is above 9 kHz or below 2 kHz, the EUT complies with [2] at the “Design assessment” stage.

Even if it does not satisfy the “Design assessment” conditions, the EUT complies [2] provided the measurement results satisfy the harmonic current limits in Figure 9 [2]:

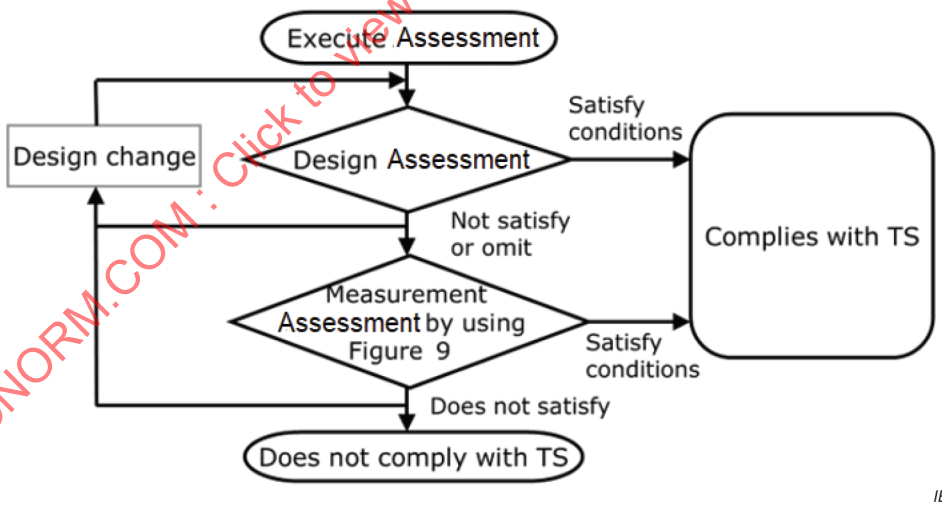

Figure 8 – Flowchart to assess an appliance’s compliance with JIS TS C 0058 [2]

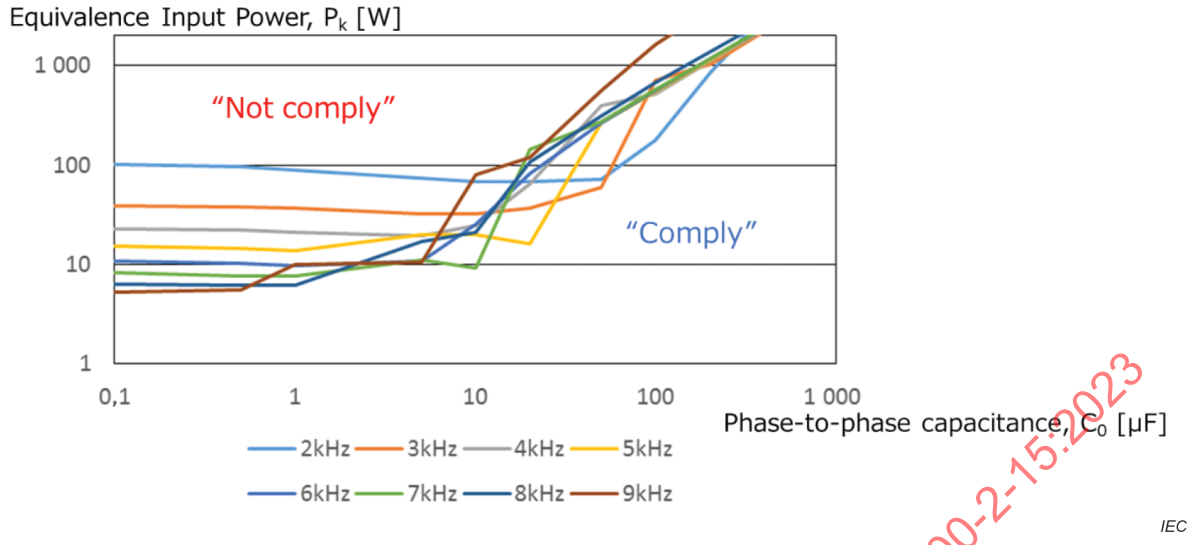

Figure 9 – Harmonic current limits for measurement assessment

- Impact on the equipment

  Reference [2] which stipulates the current emission limits in the range of 2 kHz to 9 kHz, is significant not only for sustaining the power quality for ten Japanese DSOs ("distribution system operators"), but also for producing the power electronics appliances for manufacturers [1]. The number of inquiries to DSOs regarding this issue decreased year after year thanks to the effort on [2] as shown in Figure 10. The appliance, which has harmonic current sources of 2 kHz to 9 kHz, was improved by the manufacturers before publishing reference [2].

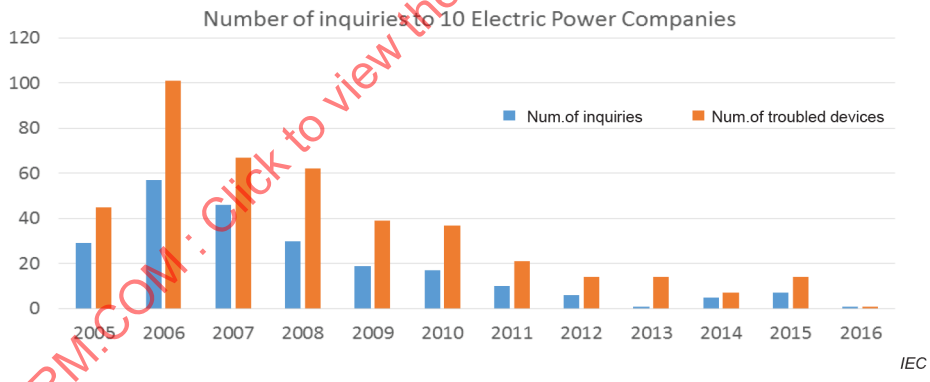

Figure 10 – Trends of the number of inquiries regarding current emission limits in Japan

Finally, these japanese technical specifications have been upgraded to a JIS Standard in 2020 [3].

4.2 Analysis and modelling of an EV charging hub with PV production

A measurement campaign has been carried out in a commercial building with an EV charging infrastructure and photovoltaic installations [4] (see Figure 11). High current peaks of up to 1,3 A on the 8th harmonic were measured at the fast charging stations during the transmission of ripple control signals transmitted at a frequency of 396 Hz. Although there were no problems with the transmission of the ripple control signal in this case, the parallel connection of several charging stations can affect communication. A high current due to a voltage harmonic generated by another converter at a resonance frequency could also damage the EMC filter capacitors at the input of one EV charger. This kind of effects can be considered when planning large EV charging hubs.

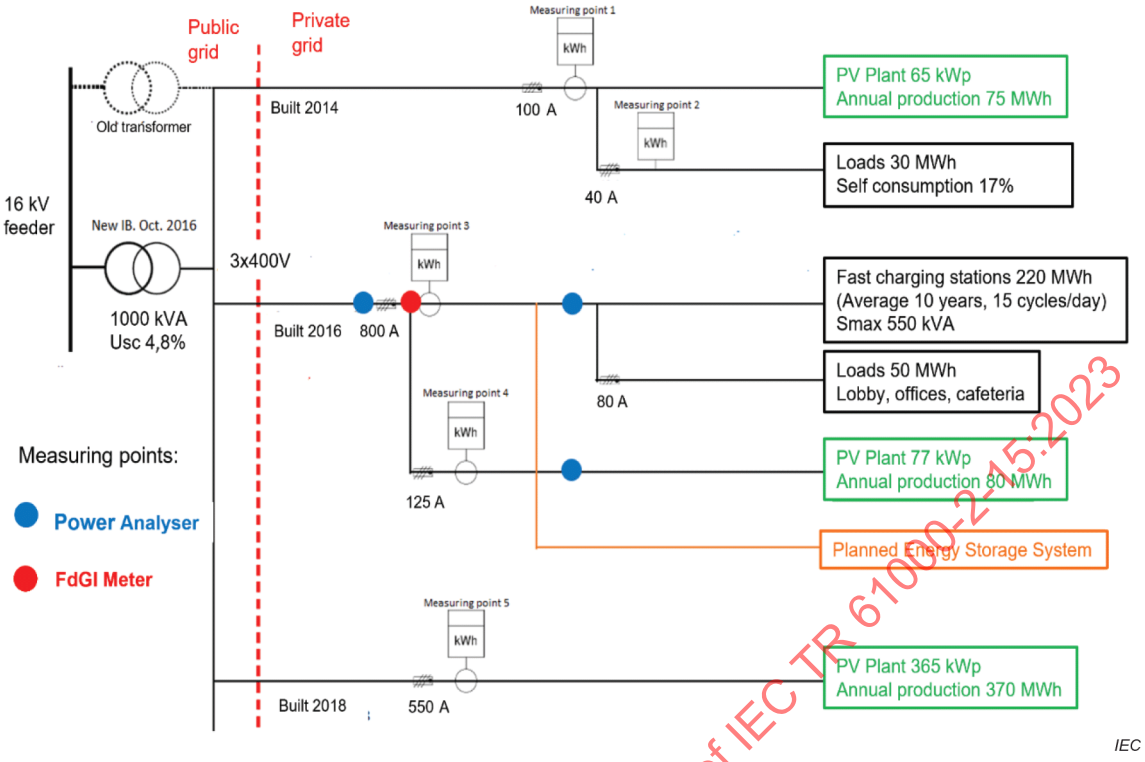

Figure 11 – Bloc scheme of the measured EV charging hub with PV production

These reflections motivated the modelling and the analysis of the situation with parallel connection of several converters with different types. The frequency-dependent grid impedance (FdGI) was in the frequency range between 150 Hz and 500 Hz, and was first measured on the busbar of the main distribution board of the installation as well as on individual feeders to different consumers, see Figure 12. The impact of FdGI was considered in both frequency ranges, below 2,5 kHz and above 2,5 kHz. A simplified electrical model of the system could be created based on the measured FdGI profiles (see Figure 13). The whole system with distribution to the 50 kW and 110 kW fast charging stations, to 22 kW charging stations for on-board chargers, and to the PV inverters showed a behaviour of the impedance, which was almost independent of the connected loads.

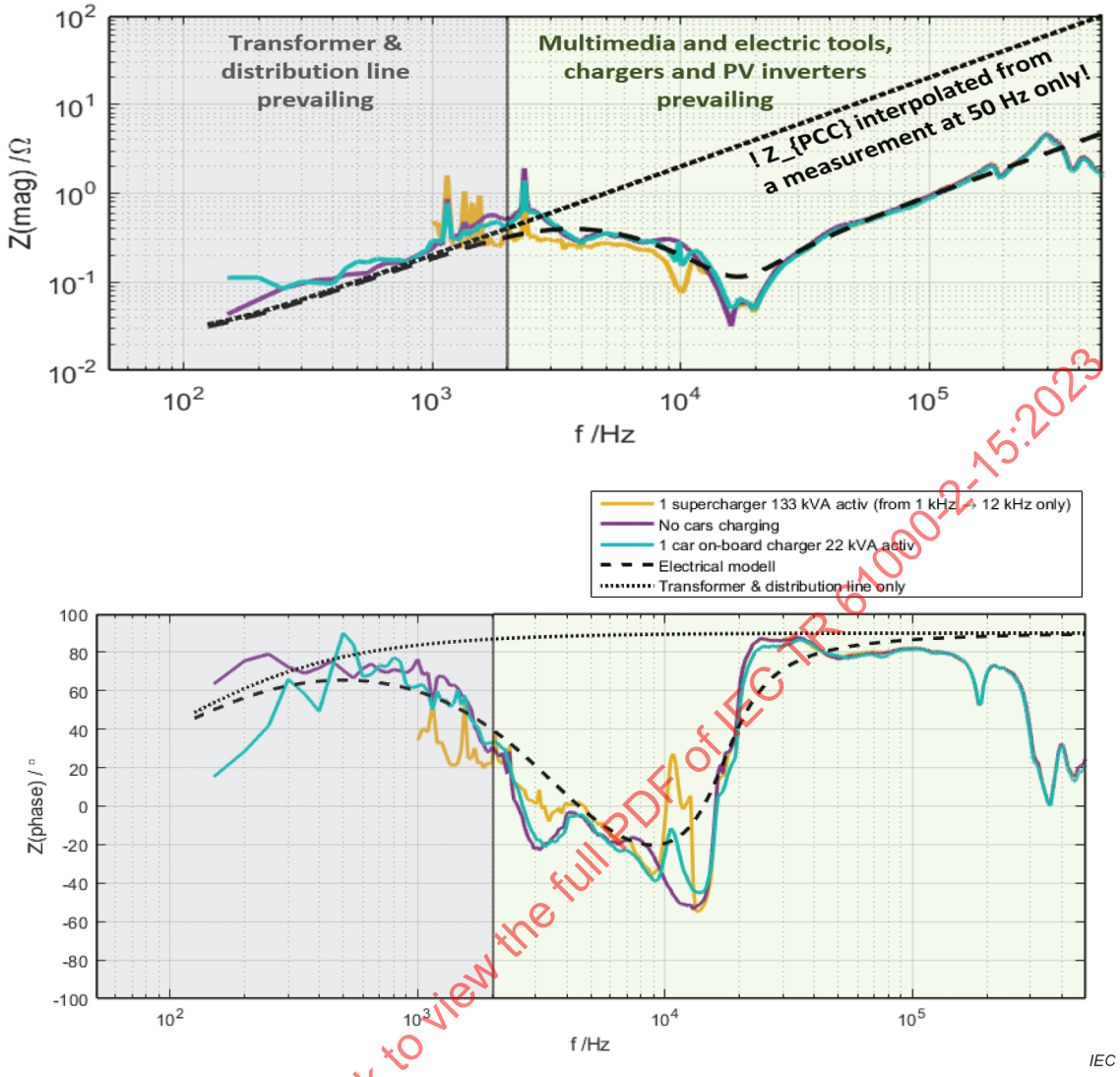

Figure 12 – Power line impedance magnitude (top) and phase (bottom) measured at the point of common connecting (PCC) of an EV charger hub with PV production

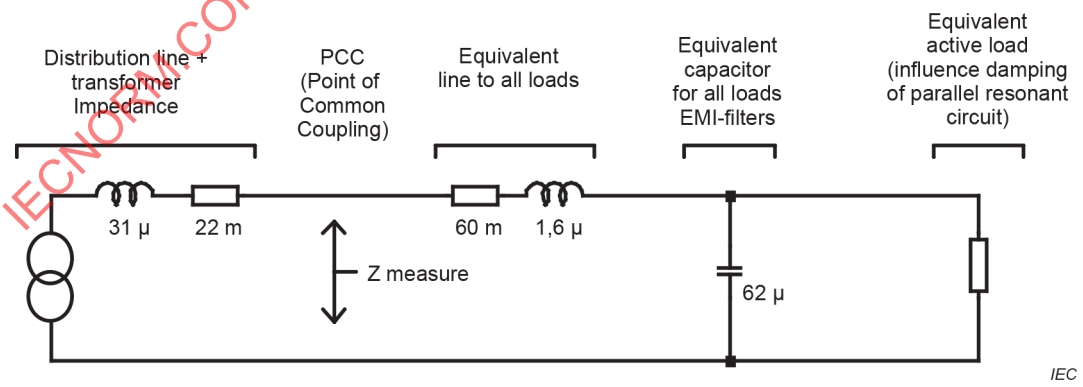

Figure 13 – Resulting simplified model of the charging hub with distribution lines and feeder

The connected charging stations and photovoltaic system only slightly influence the grid impedance in the frequency range from 50 Hz to 2 450 Hz. This can be explained by the very short connection to the local transformer station (about 80 m away), the high-power rating of the transformer (1 MVA) and its low short-circuit voltage (U_k = 4,6 %). The influence of the transformer on the FdGI is in this case dominant in comparison to the individual consumers.

In the lower frequency range (150 Hz to 2 kHz) and in the upper high frequency range (50 kHz to 150 kHz), the FdGI is mainly shaped by the supply line to the transformer and by the outgoing feeders to the loads, respectively. In the frequency range from 2 kHz to 50 kHz, resonances can be recognized (see Figure 14). The series resonance at about 16 kHz is due to the inductances of the feeders to the connected loads with the EMC filters. The parallel resonance at about 3,5 kHz is due to the supply line of the transformer station in connection with the same EMC filter capacitors.

Figure 12 confirms the assumption that the low frequency range is influenced by the short-circuit power of the transformer, while the high frequency range is influenced by the EMC filters of all devices connected to the main busbar. Thanks to the absence of residual current protections, larger devices such as chargers and PV inverters with large C_x and C_y capacitors are likely to have even more influence than smaller household appliances (especially multimedia and computers). Small household appliances can affect the impedance with possible resonance from 150 kHz onward, due to smaller C_x and C_y capacitors in their EMC filters. However, in the case of the connection of hundreds of such devices, the resulting capacitance is considerably larger, thus shifting possible resonances to much lower frequency ranges.

The larger active loads connected to the busbar (e.g. fast charging stations) are damping the parallel resonance in the lower frequency range. The impact of a super-fast EV charger is presented in Figure 14 as an example:

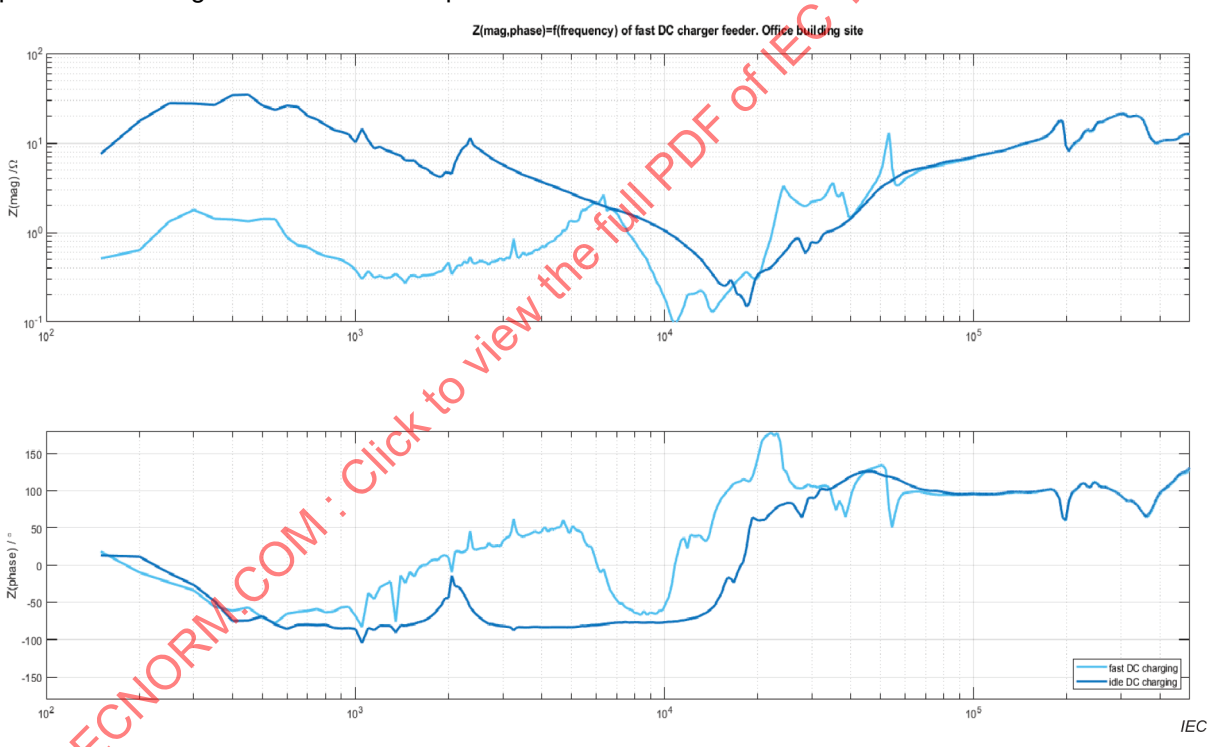

Figure 14 – Impact of a super-fast EV charger on grid impedance

The analysis of Figure 12 leads to the following conclusion: The current harmonics generated by an inverter by PWM modulation hardly flow to the transformer when the transformer station is relatively far away, because the impedance to the transformer station is much higher than the impedance to other devices connected to the same busbar.

Even though conducted emissions are very low at that frequency, current distribution between loads and sources can be predicted and verified at 8,1 kHz, where both the current harmonics and power line impedance of the individual feeders are measured. At that frequency, small current emissions can be traced with long-term measurements back to one of the inverters. The impedance and current running through the feeders are displayed in Table 1. The current drawn from the PV system at 8,1 kHz runs into the feeder with the lowest impedance. Since the measurements in the feeders are performed one after the other, the sum of the currents of all feeders deviates slightly from the total current of the PV system. Figure 14 shows that the current drawn by the PV inverter mainly flows into the offices and workshops, i.e. where the impedance is lowest at 8,1 kHz. As described in Clause 4, the phase angle of currents and impedances can be considered for more accurate analysis.

Table 1 – Relation between measured current and respective impedance for each feeder

Feeder	Impedance, Z_h at 8,1 kHz, in Ω	Measured current at 8,1 kHz in mA
PV-installation (source for the emission)	-	29
Fast EV charger (no charging car)	1,51	5,9
On-board chargers	2,69	6,8
Feeder from transformer station	1,55 (estimated from the model)	7,1
Office and workshop facilities	0,41	28

In conclusion, a simplified circuit model of the installations, including the transformer, lines EMC filters and power converters can be obtained on the basis of FdGI measurements. Computer simulations in the frequency domain analysis can help predict resonances and excessive current flowing from one converter to the other as described in 4.1.1. A standardized indication of converter input capacitance and switching frequency can make a preliminary assessment about compatibility between a new converter and an existing grid section.

4.3 Impact of power electronic household equipment on the impedance characteristics in residential networks

The input impedance of power electronic (PE) equipment often has capacitive characteristics [5],[7]. Large amounts of such equipment (i.e. in households or office buildings) can consequently introduce a significant capacitance into the public low voltage networks, which can form a resonance with the inductances of the lines and the supply transformer. To study this impact, different combinations of typical household devices, which are further referred to as load scenarios, have been defined. For each load scenario, the input impedance characteristic up to 2 kHz has been measured using the method described in [6], [8] Based on the measured impedances, a suitable equivalent (impedance) circuit model is introduced, and its parameters are identified based on a vector-fitting approach. The equivalent models for the load scenarios are finally integrated into a residential LV network simulation model and different evolution stages of PE penetration, namely past, present, and future have been simulated [5], [6].

The device topologies in the load scenarios vary according to the evolution stages as shown in Table 2. Lighting loads (D3 to D5) have been transformed from incandescent lamps in the past to CFLs (compact florescent lamps) and LEDs (light-emitting diodes) at present, and exclusively LEDs in the future. A similar transition can be considered for refrigerators and vacuum cleaners, which have evolved from simple capacitive-start induction-run motor devices to devices with PE front-ends including active power factor correction (aPFC) over the last few decades. The three distinct evolution stages are considered to elucidate the increased proliferation and replacement of several passive loads by PE-based loads for most common household devices as per [9] In the “past”, the share of passive loads was higher, and the only PE-based loads were computers (PCs) and televisions (TVs). The PE-based devices in all load scenarios can be categorized into non-power factor corrected (nPFC), passive-power factor corrected (pPFC), and active-power factor corrected (aPFC) circuit topologies.

Table 2 – Devices and topologies used in the different evolution stages

Device (D)	Device name	Past (A)	Present (B)	Future (C)
1	Refrigerator	Passive	Passive/aPFC	aPFC
2	Router	N/A	nPFC	nPFC
3	Incandescent lamps	Passive	N/A	N/A
4	CFL	N/A	nPFC	N/A
5	LED	N/A	nPFC/aPFC	nPFC/aPFC
6	PC	n-pfc	pPFC/aPFC	aPFC
7	Laptop	N/A	nPFC	nPFC
8	Hotplate/ Water cooker	Passive	Passive	Passive
9	Induction stove	N/A	aPFC	aPFC
10	TV	nPFC	nPFC/aPFC	aPFC
11	Hair dryer	Passive	Passive	Passive
12	Vacuum cleaner	Passive	Passive/nPFC	nPFC

The methodology proposed in [9] is used to identify the set of devices connected at a given time instance of the day. In this study, three different time instances in a day depending on the power demand at the fundamental frequency are considered, namely peak demand (evening), average demand (morning and afternoon) and low demand (after midnight). In combination with the three different evolution stages past (A), present (B) and future (C), this results in a total of nine load scenarios (IA, IB, IC, IIA, …), as shown in Table 3 for which the individual sets of devices are given. In all the device sets, passive devices, which transition into PE-based devices, are equi-proportionately replaced across various evolution stages.

Table 3 – Load scenarios depending on the evolution stages and loading conditions

	Set of devices		
Evolution stage (*k*)	**I (low demand)**	**II (average demand)**	**III (peak demand)**
Past (A)	$D_{A1}+D_{A3}$	$D_{A1}+D_{A3}+D_{A6}$	$D_{A1}+D_{A3}+D_{A6}+D_{A8}$
Present (B)	$D_{B1}+D_{B2}+D_{B4}+D_{B5}$	$D_{B1}+D_{B2}+D_{B4}+D_{B5}+D_{B6}$	$D_{B1}+D_{B2}+D_{B4}+D_{B5}+D_{B6}+D+D_{B9}$
Future (C)	$D_{C1}+D_{C2}+D_{C5}$	$D_{C1}+D_{C2}+D_{C5}+D_{C6}$	$D_{C1}+D_{C2}+D_{C5}+D_{C6}+D_{C9}$

The measured frequency-dependent input impedance of each load scenario has been fitted into an RL||RLC equivalent circuit. Table 4 provides the equivalent parameters for all nine-load scenarios.

Table 4 – Equivalent $R_{L1}L_1||R_{L2}L_2C_2$ parameter values

Scenario #	R_{L1} · (Ω)	L_1 (mH)	R_{L2} (Ω)	L_2 (mH)	C_2 (µF)
IA	340	0	0	0	0
IB	400	0	30	0	4,5
IC	230	0	40	0	3,1
IIA	30	0	28	1	7,5
IIB	100	0	20	0	7,5
IIC	50	0	15	0,6	15
IIIA	28	0	28	0	10
IIIB	36	8,83	9,5	6,33	12,3
IIIC	50	0	14	0	12

The equivalent load models and the corresponding parameters derived are implemented in an urban residential LV network (single-fed, radial structure). The urban network supplies 180 households with a 630 kVA MV/LV-transformer. The respective load scenarios are applied to all customers representing an “average device scenario” although in practical cases the load scenarios most likely differ between different customers even at one considered time instant (i.e. peak load). This distribution of various load scenarios amongst various households is considered as a scope of future work.

Figure 15 shows the magnitude and the phase angle of network harmonic impedances simulated at the LV busbar of the MV/LV transformer $\underline{Z}_{\mathrm{B\,Dk}}$ and the customer-side harmonic impedances $\underline{Z}_{\mathrm{C\,Dk}}$ (part of the network impedance representing all impedances downstream the LV busbar) for the nine load scenarios. The presence of a resonance can be identified, if the simulated magnitude of the nodal impedance curve for the load scenario is above the impedance line $\underline{Z}_{\mathrm{B\,ext}}$ extrapolated based on the impedance at fundamental frequency. The resonance does not exist for all “past” scenarios. This can be attributed to the lower capacitances or absence of capacitances and higher damping provided by the passive devices in the respective load scenarios (IA, IIA, IIIA) as shown in Figure 15 (c) and (d). As the number of PE-based devices increases and the number of passive devices decreases, the possibility of resonance increases for the present and future evolution stage. It can be seen from Figure 15 (c) and (d), that the customer-side phase angles are decreasingly capacitive for “present” and “future” evolution stages.

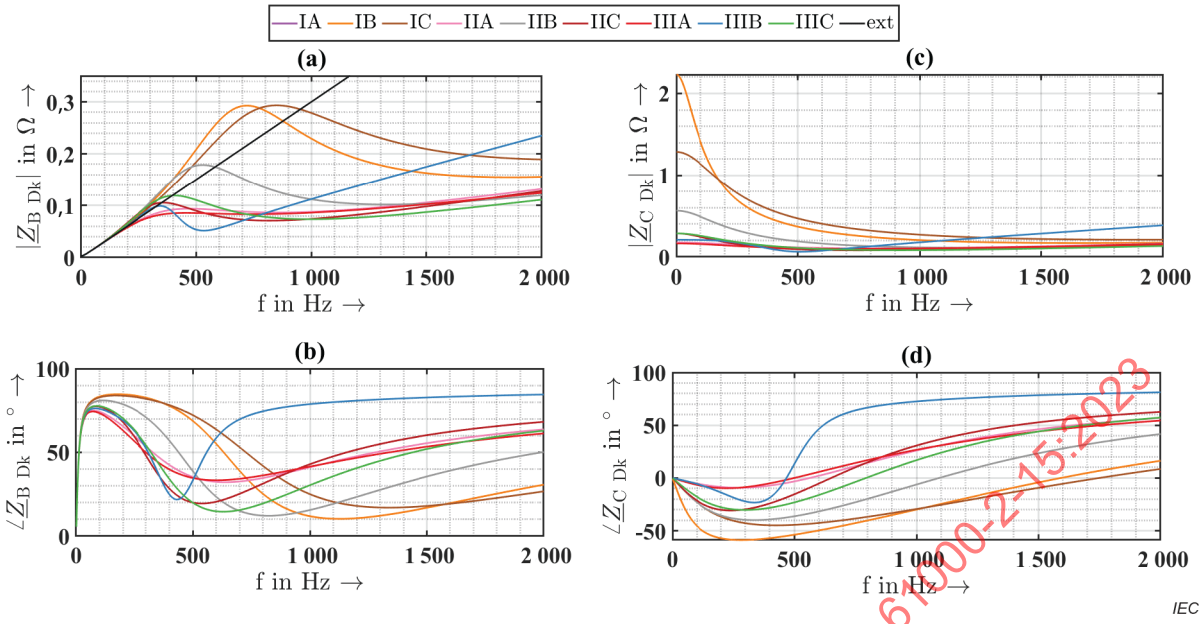

Busbar: (a) magnitude, (b) phase angle; customer-side: (c) magnitude, (d) phase angle.

Figure 15 – Impedance characteristics of an urban LV network,

The intensity of the resonances is characterized by the magnitude ratio ($k_{A\,Dk}$) between the network harmonic impedance and the extrapolated impedance based on the value at the fundamental frequency. Table 5 shows the resonance frequency and the magnitude of the ratio ($k_{A\,Dk}$) for the nine scenarios.

Table 5 – Ratio between network harmonic impedance and extrapolated impedance for various cases

Scenario #	f_r (Hz)	$k_{A\,Dk}$
IA	N/A	N/A
IB	608	1,47
IC	656	13

Scenario #	f_r (Hz)	$k_{A\,Dk}$
IIA	N/A	N/A
IIB	412	1,27
IIC	251	1,15

Scenario #	f_r (Hz)	$k_{A\,Dk}$
IIIA	N/A	N
IIIB	N/A	N/A
IIIC	284	1,15

In case of low power demand (device set I), in the future, this can lead to higher resonance frequency and lower value of $k_{A\,Dk}$ due to lower capacitive and higher resistive characteristics of the customer-side impedance compared to the “present” (see Figure 15 (d)). It can be seen from Table 5 for low load demand (scenarios Ik) and average load demand (scenarios IIk), that the resonance frequency and the ratio $k_{A\,Dk}$ decrease in the “future” compared to the “present” due to higher capacitive and higher resistive characteristics of the customer-side impedance.

For the peak load demand (scenarios IIIk), the urban network does not possess any resonance characteristics for the “present” and only a less pronounced resonance in the “future”. Based on the results, it can be inferred that despite higher equivalent capacitance for individual customer the value of $k_{A\,Dk}$. does not necessarily increase, but the resonance frequency tends to be reduced.

It can be further concluded that the PE-based devices increase the probability of harmonic resonance in the “present” and “future” with varied intensity levels depending on the evolution stages and load demand. The amplification level and the resonance frequency of resonances in the future are expected to be lower compared to the present situation. Further details on this study can be found in [10].

4.4 Harmonic resonance in an urban, residential low voltage grid

The LV network considered in this case study is located in a major city in Germany and its layout is presented in Figure 16. It supplies about 240 domestic customers in single-family houses and apartment houses as well as 85 streetlights. No shunt capacitor banks are connected to the network.

Each streetlight contains a grid-side shunt capacitance for power factor correction at power frequency and behaves as strongly capacitive at frequencies higher than 100 Hz. The network is operated as a meshed grid and has a high short circuit power (about 3 MVA at the three junction boxes).

The network has been built about 10 years ago on “greenfield”. Usually in such strong, newly built networks, no power quality problems are expected. This suggests that most of the domestic customers have a dominating share of modern energy-efficient power electronics, which also introduces a significant amount of shunt capacitance.

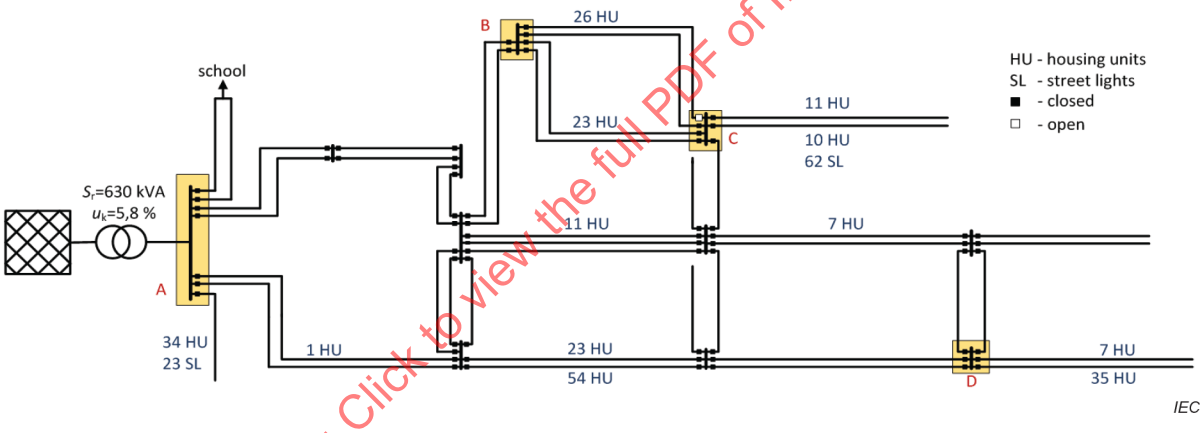

Figure 16 – Schema of the network

Routine measurements by the distribution system operator (DSO) indicated the existence of a resonance around 500 Hz. In particular, a strong amplification of mains signaling voltage by a factor of 2,5 and sudden, significant changes in harmonic levels in case of switching the streetlights have been observed.

The network harmonic impedance has been measured at the junction boxes (B, C, and D in Figure 16) and the LV busbar (A in Figure 16). Figure 17 presents an example of magnitude and phase angle of the network harmonic impedance L1-N measured at a time instant during the day, when the streetlights are switched off.

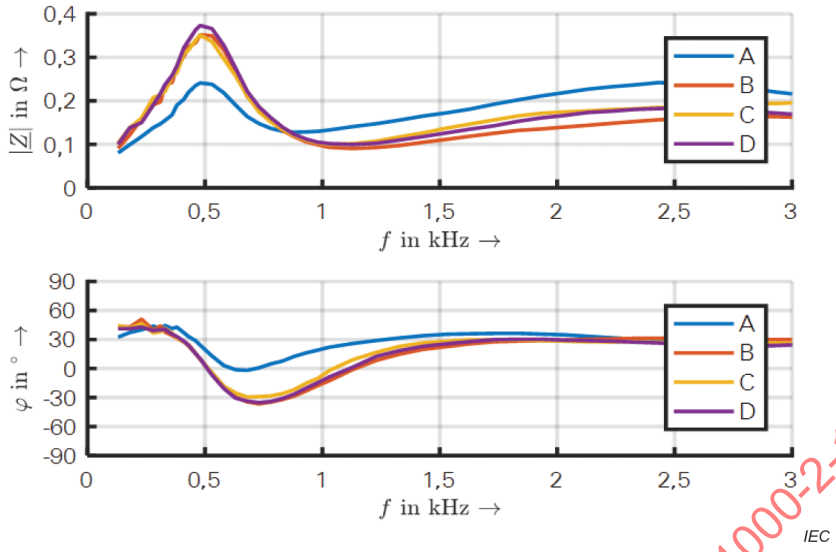

Figure 17 – Network harmonic impedance measured at different locations (L1-N)

Loop impedances L2-N and L3-N are similar, and no significant variations have been observed at different times of the day. At all locations A to D, a pronounced parallel resonance around 500 Hz is observed. As the frequency used for mains signaling is, with 482 Hz, very close to the resonance frequency, it is confirmed that the aforementioned amplification of mains signaling levels in this network is caused by the resonance. As streetlights are switched off during the day and line capacitances in LV networks are too small to cause resonances at such low frequencies, the only reason for the resonance can be the distributed capacitance of the domestic customers.

To study the reasons for the resonance, a detailed simulation of the network has been developed. At first, the network harmonic impedance at the locations A to D has been simulated using default elements, which means π-equivalence for lines, series R-L equivalence for MV/LV transformers and parallel R-L equivalence for the domestic customers. The results without streetlights are presented in Figure 18 and do not show any resonance. This confirms that line capacitances cannot be the reason for the measured resonance.

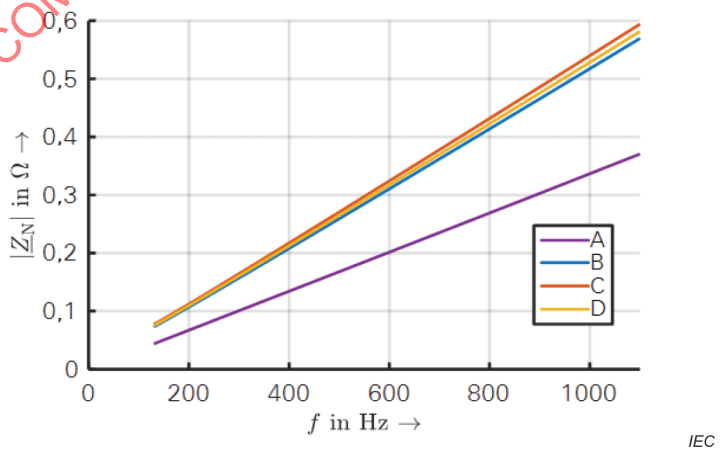

Figure 18 – Simulated network harmonic impedance at different locations (L1-N) using default element representations

In a second step, a suitable equivalent circuit has been developed and parameterized for the domestic customers to match the measured impedances as closely as possible (see Figure 19).

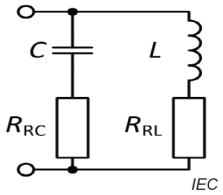

$C \approx 5$ µF; $R_{RC} \approx 0{,}5$ Ω;
$L \approx 95$ mH; $R_{RL} \approx 130$ Ω

Figure 19 – Equivalent impedance model of a domestic customer

The results are presented in Figure 20. They show a good match with the measurements (dots) for the three junction boxes, while at the LV busbar the simulation is slightly too low. It can be noted that the model is a specific harmonic load model providing satisfying results at frequencies around the first resonance but is not suitable for simulations at power frequency.

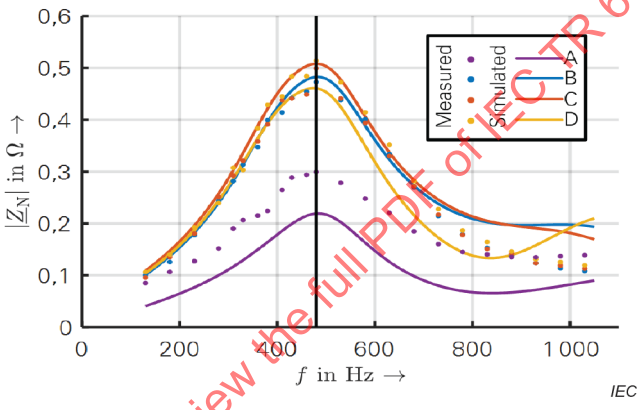

Figure 20 – Measured and simulated network harmonic impedance at different locations (L1-N) using the developed customer impedance model

The streetlights have only a minor impact on the resonance. If they are switched on during the night, the resonance shifts to slightly lower frequencies, because slightly more capacitance is connected to the grid.

The case study shows that modern power electronic converters can cause significant resonances at low harmonics in residential LV networks. Besides amplification of harmonic voltages and currents, this can also lead to harmonic instabilities together with for example PV-inverters or converters for battery storage. As these capacitances are distributed in the network, detuning as in the case of dedicated capacitor banks is not an option. In the case where resonance causes harmonic voltages above the compatibility levels (e.g. in accordance with IEC 61000-2-2 [64]), the most promising option is an impedance shaping by active filters. The presented study has clearly shown that harmonic resonances in LV networks cannot be neglected anymore. DSOs may consider including such issues already in the process of network planning. Further, resonances can also be considered when calculating harmonic emission limits for customer installations.

Further details on the presented study can be found in [5].

4.5 Harmonic distortion and impedance characteristics in an islanded microgrid

The frequency-dependent grid impedance (FdGI) forms the link between voltage and current distortion and is one of the key parameters for managing electromagnetic compatibility (EMC). In 100 % power electronic–based networks, the FdGI is expected to be considerably different compared to “traditional” interconnected grids, which might have a considerable impact on future EMC coordination strategies, especially the definition of emission limits.

In order to study the impact of the supply grid configuration on the FdGI as well as voltage and current harmonics, the laboratory setup presented in Figure 21 is used.

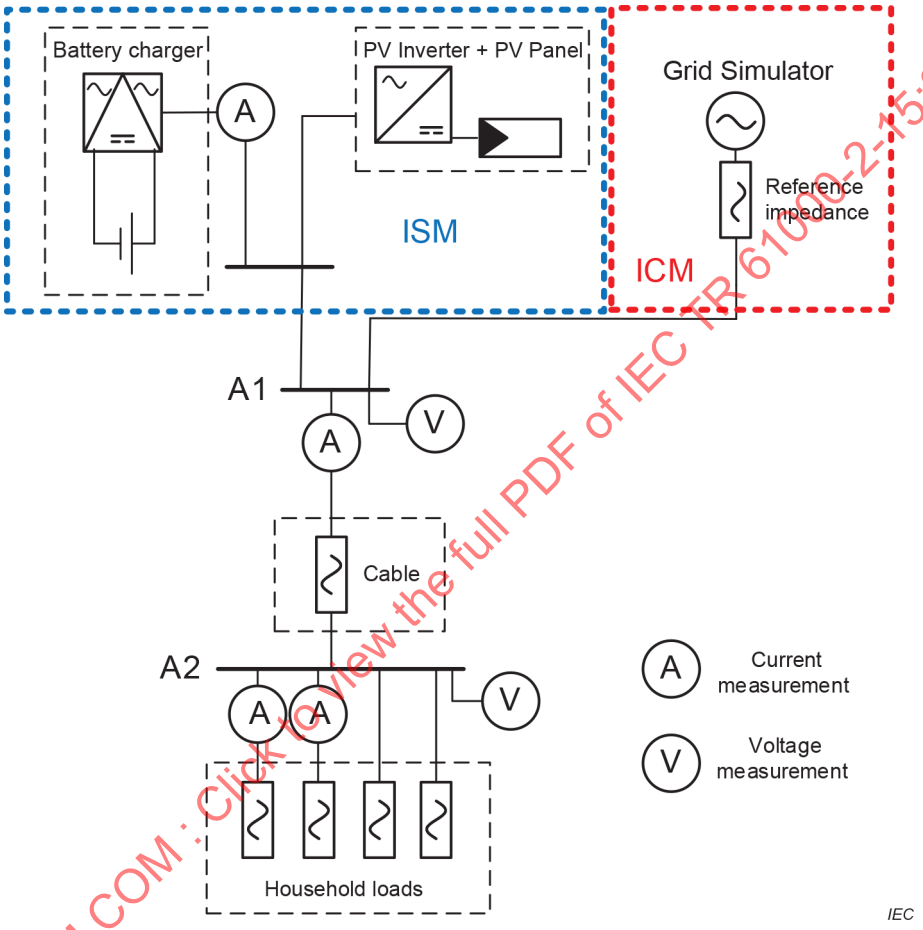

Blue box: islanded mode; red box: interconnected mode.

Figure 21 – Schematic representation of system under test

The system can operate in the islanded mode (ISM; blue dashed box) and interconnected mode (ICM; red dashed box). In ISM, the source is a combination of a battery-fed voltage-controlled converter and a PV inverter, which synchronizes to it and operates in current-controlled mode. In ICM, the source comprises a grid simulator and a reference impedance as defined in IEC 61000-4-7:2002/AMD1:2008, [65] Annex B. Various types of loads as summarized in Table 6 are connected.

Table 6 – Load scenarios

Scenario	Load type	Total power demand
Load 1 (L1)	Non-power factor corrected (nPFC)	715 VA
Load 3 (L3)	Active power factor corrected (aPFC)	390 VA
Load 4 (L4)	Passive	4 000 VA
Mixload (MI)	nPFC+aPFC+passive	4 600 VA

The loads are classified as non-power factor corrected (nPFC), active power factor corrected (aPFC), and passive. The nPFC loads (L1) are composed of a variety of lamps such as CFL and LED. The aPFC loads (L3) are composed of a laptop charger and several PC loads. Passive loads (L4) are water cookers and incandescent lamps. The mixload scenario (MI) is obtained by a combination of a variety of the above-mentioned loads.

For each of the scenarios, measurements of the FdGI (see Figure 22) as well as voltage and current harmonics in the frequency range up to 2 kHz have been carried out at the busbar A1. The network impedance in Figure 22 (e) and (f) is determined as a parallel circuit of the upstream and downstream impedance at busbar A1. The upstream impedance corresponds to the grid-side impedance in Figure 22 (a) and (b) and the downstream part to the load-side impedance in Figure 22 (c) and (d). The presentation and discussion of results is limited to those scenarios involving power electronic loads (L1, L3, and MI).

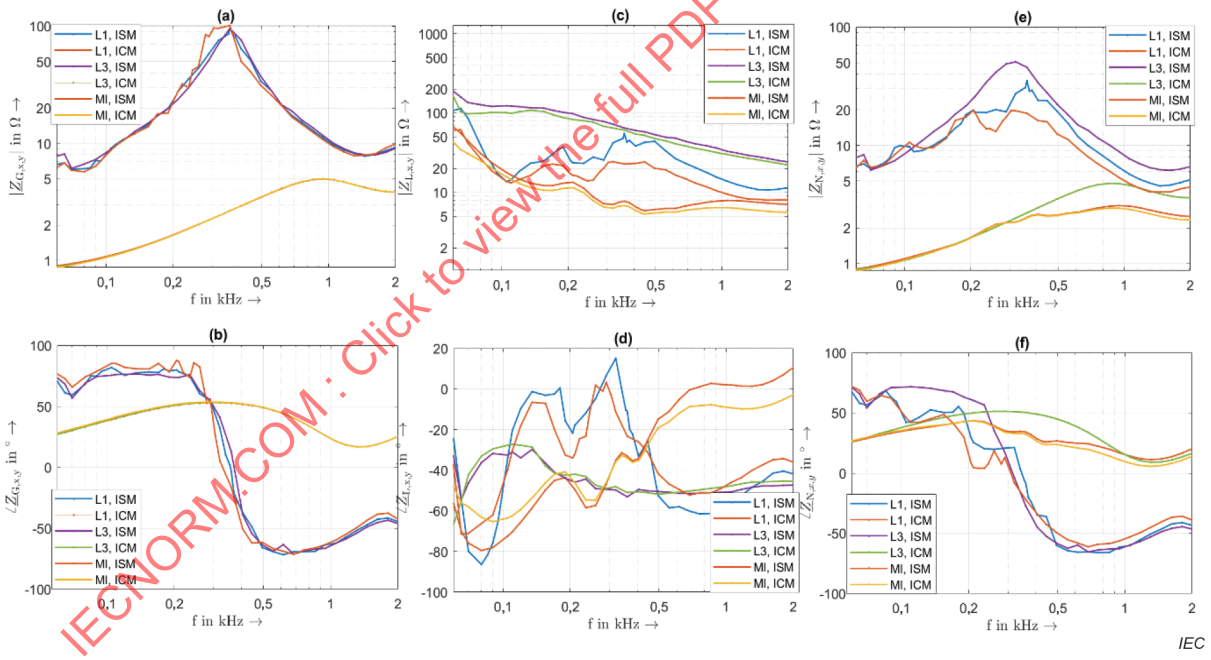

Grid-side and upstream impedance (a), (b); load-side and downstream impedance (c), (d); and network and total impedance (e), (f).

Figure 22 – Impedance characteristics (magnitude and phase angle)

The grid-side impedances as shown in Figure 22 (a) and (b) are far lower in magnitude for ICM compared to ISM. Both are virtually independent of the load scenario. The magnitude of short-circuit impedance for ISM is about 5,8 times higher than in ICM. In ISM, the grid comprises a strong resonance at around 350 Hz (7th harmonic) where the impedance is about 33 times higher than in ICM.

The origin of the resonance can be attributed to the grid-side filter circuits and closed-loop controllers in the respective sources (battery and PV) and the interaction between them. The phase angle characteristics in ICM remain resistive-inductive in the considered frequency range, while they get highly capacitive in ISM beyond the resonance frequency. Figure 22 (c) and (d) shows the load-side impedance characteristics. All presented scenarios exhibit capacitive behaviour in large ranges, which is caused by the character of the power electronic devices. As expected, the operation mode of the grid has no significant impact on their behaviour.

Figure 22 (e) and (f) presents the network impedance characteristics of ICM and ISM. While in ICM for scenario L3, due to the rather high load-side impedance, the network impedance is virtually like the grid-side impedance, for scenarios L1 and MI a visible influence at frequencies above 250 Hz can be observed. In case of ISM, although the resonance frequency remains unaffected, the resonance magnitude is reduced for the three load scenarios with the smallest reduction for scenario L3. The phase characteristics are comparable between the grid-side and network impedances for all load scenario and both operating modes. As for grid-side impedances, the magnitude of the network impedance is far higher for ISM compared to ICM.

Figure 23 presents the voltage harmonic levels for both operation modes. In ICM, the harmonic voltages are almost independent of the load scenario and are determined by the background distortion that has been set in the grid simulator in order to represent a voltage distortion typically found in residential LV networks. In ISM, the background voltage without any load connected is much lower compared to ICM, but the load scenarios have a considerable impact on the voltage harmonic levels. A favorable cancellation exists between the different devices in scenario MI, which in turn results in the lowest harmonic voltage levels.

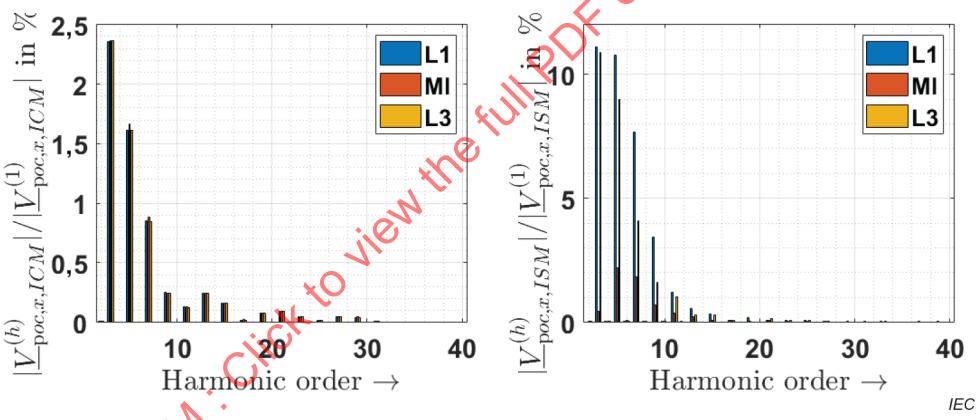

Figure 23 – Voltage harmonic levels in ICM (a) and ISM (b)

The experimental results prove that due to the higher network impedance in ISM the voltage harmonics are significantly amplified compared to ICM. The impact of background voltage is higher in case of ICM. It can be concluded that the generation of voltage distortion by the respective distorting loads is qualitatively different between ICM and ISM. Moreover, in ISM pronounced resonances will be expected in the FdGI. These results confirm that the harmonic characteristic in 100 % power electronic–based grids, particularly the smaller ones, differs considerably from the present conditions in interconnected networks. This may be considered in future EMC standardization. Further details and measurement results can be found in [6]

5 Impact of modern power electronics on the propagation and amplification of voltage distortion

5.1 Harmonic propagation in a residential LV network

5.1.1 General

In the following, the case is illustrated of a residential area where significant voltage amplitude variations of the 15th harmonic were registered. The issue was due to the operation of large heat pumps connected to the grid.

Furthermore, the voltage level at each grid point is not only influenced by the operation of such inverters, but higher harmonic voltage amplitudes can be expected, caused by the sum of all loads in the grid [27]

Figure 24 represents the single line diagram of a residential area hosting a building complex where the heat is generated by two heat pumps: a large one powered by a 150 kW inverter and a small heat pump driven by a 35 kW inverter. The grid is analyzed in the PowerFactory[2] software [28], see below:

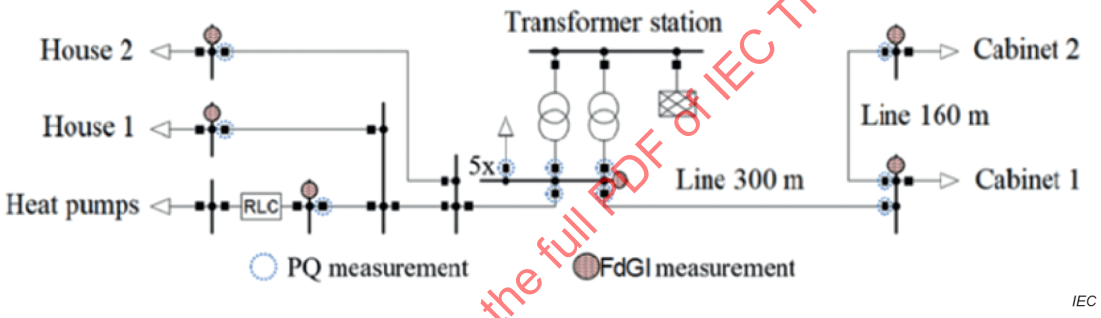

Figure 24 – Simplified line diagram of the grid with marked measuring points

5.1.2 Measurements

In two measurement campaigns, 6 grid nodes were monitored with 15 PQ measuring devices (PQ-Box 100/150/200, a-eberle). Additionally, the FdGI was measured and analyzed. The transformer stations, house 1 and house 2, belong to the building complex where the heat pumps are installed. The remote cabinets 1 and 2 are connected to the transformer station by long cables of 300 m and 160 m. In the standard situation, there was no active filter (corresponding to the node RLC in Figure 24) installed.

To measure PQ parameters, voltage sensors were connected to the three phases L1 to L3, to neutral N and to protective earth PE (see Figure 25), corresponding to measurement category CAT IV. The terminals of voltage probes connected to the feeders are equipped with fuses. The current sensing was performed by Rogowski coils or current clamps. The neutral conductor current was measured. Measurement data were saved as RMS values in 1 min intervals with Class A devices in accordance with IEC 61000-4-30 [66] to achieve sufficient accuracy.

2 PowerFactory is the trade name of a product supplied by DIgSILENT GmbH. This information is given for the convenience of users of this document and does not constitute an endorsement by IEC of the product named. Equivalent products may be used if they can be shown to lead to the same results.

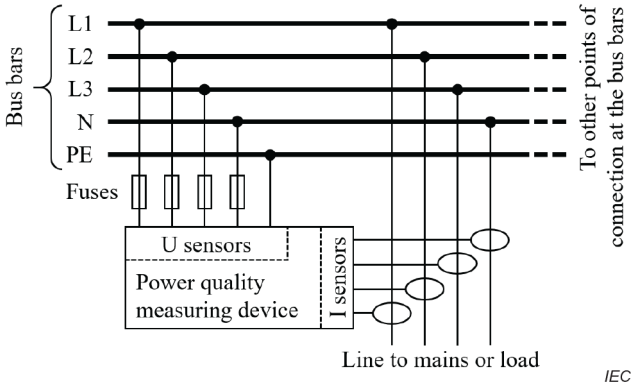

Figure 25 – Connection of a PQ measuring device

Three main operating states of the heat pumps were analyzed: operation of the large heat pump, operation of the small heat pump, and off state of both heat pumps. The simultaneous operation of both heat pumps never occurs. The heating power of both heat pumps depends on the outside temperature and it is limited by their maximum power rating of 150 kW and 35 kW, respectively. The operation of the heat pumps results in a higher 15th harmonic current amplitude, which influences the voltage drop for the 15th voltage harmonic across the grid impedance. The measurements at the connection point of the heat pumps revealed that the large heat pump has stronger influence on the voltage level, particularly when operating at maximum power (Figure 26). In contrast, the small heat pump led to voltage variation not proportional to the voltage changes induced by the larger heat pump. The variation of the current amplitude was not affecting the voltage magnitude in both cases, but rather the variation of current angle and the FdGI.

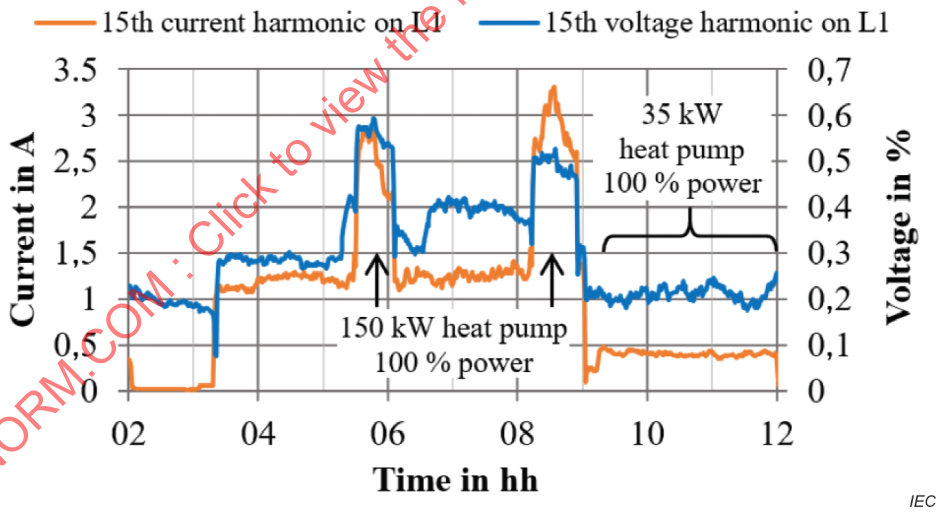

Figure 26 – Measured 15th current and voltage harmonic on phase L1 during operation of the heat pumps at the heat pumps' point of connection without active filter

A similar behaviour as at the connection point of the heat pumps also occurred for all phases at the other measuring points of the building complex (transformer station, house 1 and house 2). The lowest amplitudes were measured at the transformer station.

In contrast to the results in the building complex, a different behaviour of the three phase voltages was registered at the distribution cabinet 1 and cabinet 2, which are connected with the transformer station by long cables. The 15th voltage harmonic level at both remote cabinets was higher at L2 and L3 when only the small or no heat pump was in operation. For each measuring point, the voltage levels of the three phases are plotted in Figure 27 for a specific moment during one of the following three operating states:

- power peak of the large heat pump;
- power peak of the small heat pump;
- each heat pumps OFF.

The sum of all other loads in the grid led to an elevated voltage level at cabinet 1 and cabinet 2. Furthermore, the current angles were changing for different operating states and consequently the angles of the voltage drop across the long lines, which can lead to different phenomena on the three phases.

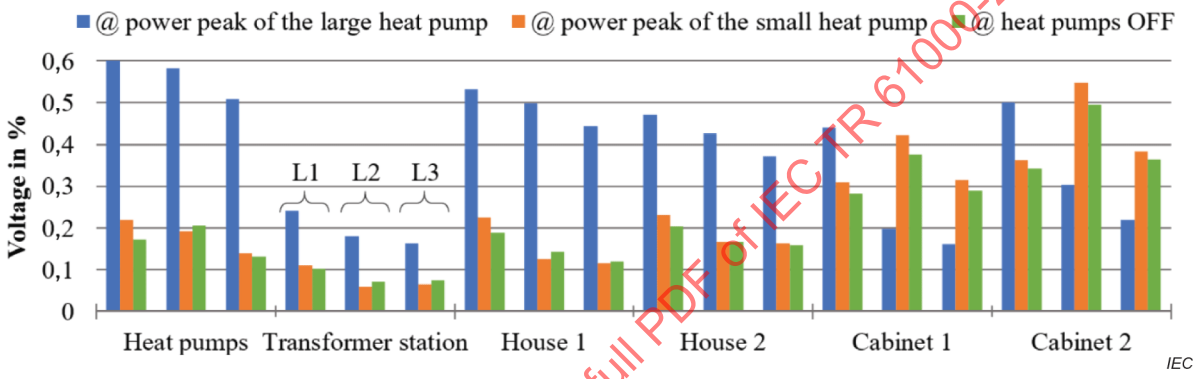

Figure 27 – Measured voltage amplitudes of the 15th harmonic for each phase L1 to L3 during three different operating states without active filter

5.1.3 Modelling issues

The investigated grid was modelled and simulated using the software PowerFactory. The measured harmonic current amplitudes and angles were set at the modelled loads. At the transformer station, a voltage source with the measured voltage was modelled. A comparison of the simulated and measured amplitudes is given in Figure 28.

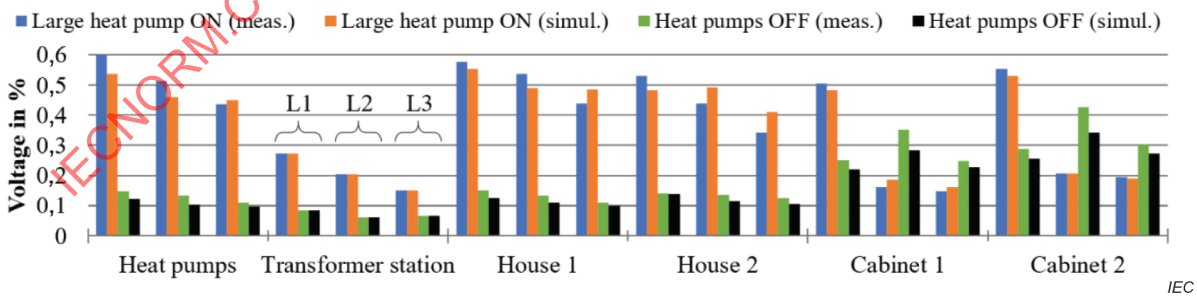

Two operating states are shown: on-state and off-state of the large heat pump. The small heat pump is always in the off state.

Figure 28 – Comparison of measured and simulated voltage levels (15th harmonic voltage) at each measuring point

The model allowed to investigate why the voltage levels of the 15th harmonic behave differently on the three phases at the remote cabinet 1 and cabinet 2. Figure 29 shows for phase L3 that the voltage angle at the transformer station is changing about 180° when the large heat pump is turned on (black phasors) or off (grey phasors), caused by the changed current flow through the transformer. The voltage at the transformer station and the voltage drops across the lines to cabinet 1 and cabinet 2 were smaller when the large heat pump was not operating. However, the voltages at the cabinet 1 and cabinet 2 are higher during the large heat pump's off state mode, because they are dependent on the angles of the line currents. In off state mode, the voltages and voltage drops add almost arithmetically, which leads to higher voltages at the remote points.

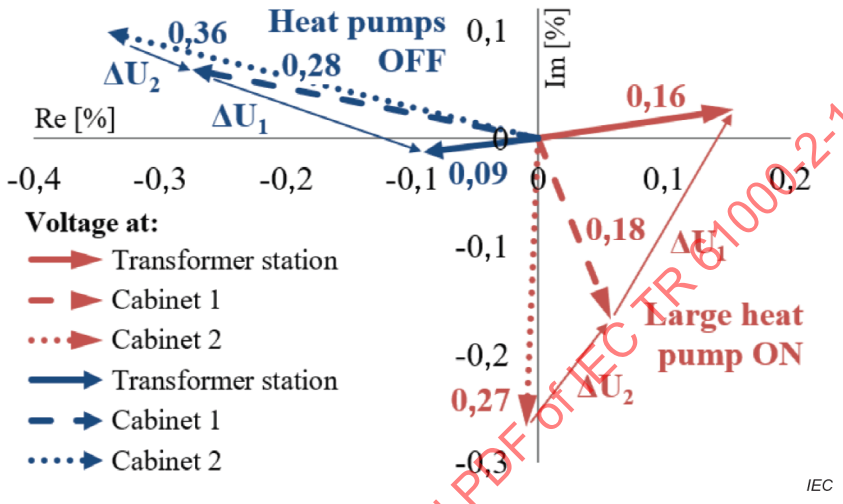

Figure 29 – Modelled voltage vectors of the 15th harmonic at on- and off-state of the large heat pump without active filtering

Power converters can influence harmonic voltage levels significantly on all points of a distribution grid. Critical harmonic amplitudes are caused not only by power converters with a high-power rating, but also by the sum of many different non-ideal loads which are supplied over long lines, as the measurements at remote points have been illustrated in agreement with the simulations of the grid model. To draw precise predictions and conclusions, current amplitudes and angles need to be measured accurately.

5.2 Supraharmonic amplification in a residential LV network with a fast charging station

5.2.1 Measurement procedures

a) Currents and voltages

Currently no mandatory standard exists for the measurement of supraharmonic voltages and currents. Proposals for such methods can be found in IEC 61000-4-30:2015 [66] Annex C, which references also to IEC 61000-4-7:2002/AMD1:2008 [65], Annex B. The supraharmonic compatibility levels provided in IEC 61000-2-2 [64] are defined in reference to CISPR 16-1-1 [67]. However, this measurement procedure has been developed for laboratory use in combination with a line impedance stabilization network (LISN) as described in CISPR 16-1-2 [68]. In [13] it is found that the method described in IEC 61000-4-7:2002/AMD1:2008, [65] Annex B provides results comparable to those obtained with the CISPR 16-1-1 and CISPR 16-1-2 method. The measurement results presented in 5.2.1 are all based on the method described in IEC 61000-4-7:2002/AMD1:2008 [65], Annex B, but partly with a grouping band other than the default one of 200 Hz. In case a modified grouping band is used, this is indicated.

b) Impedances

The impedance measurements shown in item b) are taken by injecting sinusoidal currents at different frequencies and calculating the impedance using a discrete Fourier transform (DFT). The current is injected for 10 power cycles at interharmonics frequencies at multiples of 1/10th of the network frequency. The injected current and the voltage at each respective frequency are measured before (pre) and during injection (post) and the impedance is calculated as

$$\underline{Z}(f) = \frac{\underline{U}_{\text{post}}(f) - \underline{U}_{\text{pre}}(f)}{\underline{I}_{\text{post}}(f) - \underline{I}_{\text{pre}}(f)} \quad (1)$$

Further details about the method can be found in [18].

c) Propagation

For the propagation measurements, either nonintentional or intentional emission is injected at one point of the network and the response at another point in the network is observed. With such propagation measurement, the upstream and downstream transfer characteristics can also be obtained. For the studies in item c), single-frequent sinusoidal excitations (frequency sweep) are used, as they are most accurate and as less invasive as possible.

In case existing nonintentional sources of supraharmonic emission, such as battery electric vehicle chargers or photovoltaic inverters are used, it needs to be ensured that no other sources of supraharmonic emission within the same frequency range are operated in the same grid.

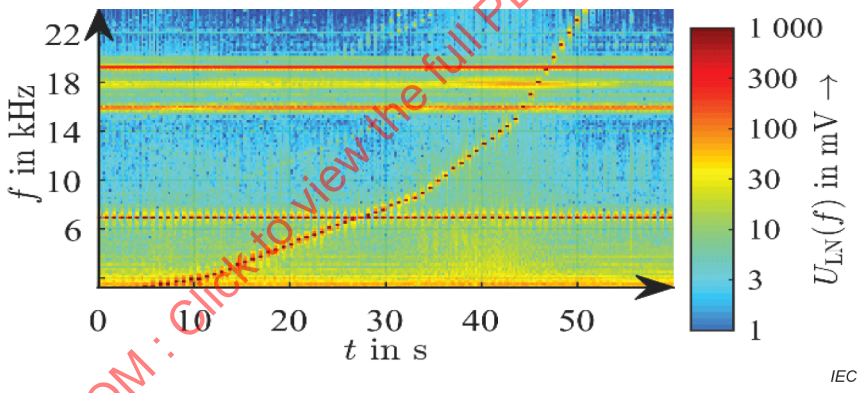

Figure 30 – Spectrogram of the voltage at the point of injection of supraharmonic currents in a residential low voltage network

For the synchronization of multiple measurement devices at different locations either accurate time synchronization (wireless or wired) or the additional injection of a pilot (trigger) signal at a frequency with low damping and low background noise can be used as. In [17], a 7 kHz injection is used for this purpose. The voltage spectrogram during a measurement in a residential low voltage network with several photovoltaic inverters is shown in Figure 30. The supraharmonic emission from photovoltaic inverters at 16 kHz, 18 kHz and 20 kHz as well as the swept injection signal can be observed.

For the assessment of supraharmonic amplifications, the frequency-dependent ratio of the voltage at any point in the grid $U_{\mathrm{L}x\mathrm{N\ pnt}}(f)$ and the voltage at the point of injection $U_{\mathrm{L}x\mathrm{N\ inj}}(f)$ in the same phase x and at the same frequency (transfer ratio) is used:

$$r_{\mathrm{T}}(f) = \frac{U_{\mathrm{L}x\mathrm{N\ pnt}}(f)}{U_{\mathrm{L}x\mathrm{N\ inj}}(f)} \tag{2}$$

For the assessment of supraharmonic coupling between phases, the ratio of the voltages in different conductors (crosstalk ratio) is used:

$$r_{\mathrm{C}}(f) = \frac{U_{\mathrm{L}x\mathrm{N\ pnt}}(f)}{U_{\mathrm{L}y\mathrm{N\ pnt}}(f)} \tag{3}$$

It is defined as the ratio of the voltage at any point in the grid $U_{\mathrm{L}x\mathrm{N\ pnt}}(f)$ and the voltage at the same point $U_{\mathrm{L}y\mathrm{N\ pnt}}(f)$ at the same frequency but in a different phase (Lx and Ly). As an estimate, in cases with connected neutral conductor and symmetrical impedances, the crosstalk ratio is $r_{\mathrm{C}} = \frac{1}{3}$. In cases without neutral conductor, the crosstalk ratio is $r_{\mathrm{C}} = \frac{1}{2}$.

5.2.2 Measurement results

In a public low voltage network in a small town in Germany the network operator noticed a supraharmonic voltage amplification along a short cable feeding a junction box with a DC charger (fast charger) and two standard AC chargers connected [17]. The layout is presented in Figure 31. The cable between the transformer busbar BB and the junction box JB is 62 m long. A supraharmonic voltage at 10 kHz is injected at the transformer busbar BB by a battery electric vehicle using its three-phase AC onboard charger. An amplification of the voltage by a factor of up to 4 at 10 kHz is measured along the cable (voltage at junction box JB 2,3 V, voltage at transformer busbar BB 0,6 V).

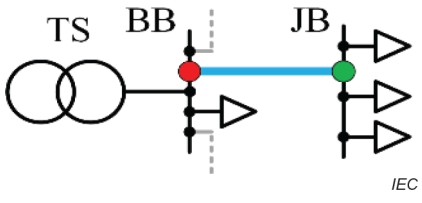

BB transformer busbar, JB junction box, TS transformer station.

Figure 31 – Single-line diagram of relevant parts of the low voltage network

a) Single-phase injection

For the measurement of the propagation of supraharmonics in the low voltage network a sinusoidal current is fed into one phase at the transformer busbar BB and the respective voltages at transformer busbar BB ($U_{\mathrm{LN\ inj}}$ in Formula (2)) and junction box JB ($U_{\mathrm{LN\ pnt}}$ in Formula (2)) in the same phase are measured. Based on the voltages the transfer ratio (see Figure 32) between the transformer busbar (BB) and junction box (JB) is assessed to determine at which frequencies amplification or damping of supraharmonic voltages occur.

The results show a significant resonance amplification of up to 2,3 at 10 kHz and 20 kHz, but only in case the DC charger is operated in idle mode. When the DC charger is disconnected, as expected, the voltage at the end of the cable is identical to the voltage at the beginning $r_T(f) = 1$. When the DC charger is charging, the resonance is damped and shifted to lower frequencies. The resonance amplifications at 10 kHz and 20 kHz are consequently not caused by the cable itself, but by the interaction of the capacitive filter impedance of the DC charger (see Figure 34) and the inductive line impedance of the cable.

Figure 33 shows the crosstalk ratio between phase L2 and L1 (injection phase) at the junction box JB. When the DC charger is disconnected, the crosstalk ratio is below 1/2, which is an expected value. When the DC charger is operated in idle mode, strong crosstalk can be observed between approximately 12 kHz and 35 kHz. At 20 kHz, the crosstalk ratio is 1 (also for the crosstalk L1-L3). Thus, at this frequency, the voltage in all three phases is nearly identical and twice the voltage injected in phase L1 at the transformer busbar. When the DC charger is charging, the frequency range with increased crosstalk widens to 5 kHz to 35 kHz, while the maximum magnitude of the crosstalk ratio is lower (r_C = 1,6) compared to idle mode (r_C = 2,4).

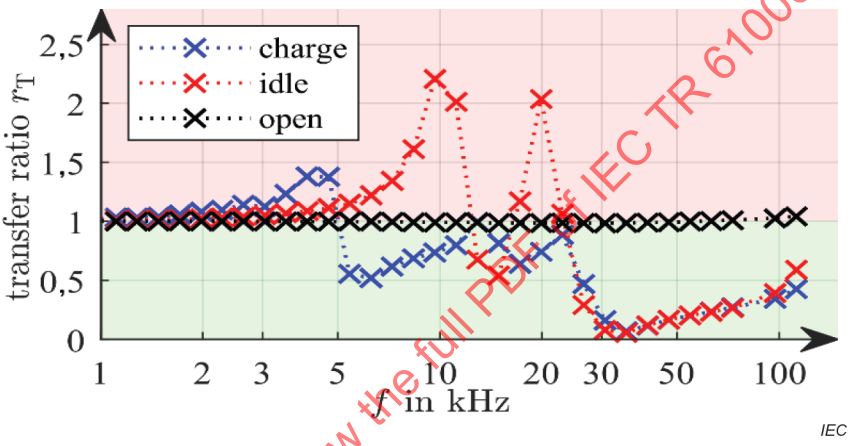

Figure 32 – Transfer ratio of supraharmonic voltage along the low voltage cable for phase L1 in case of single-phase injection at the transformer busbar BB

The following conditions apply:

- charge:
  - DC charger in charging mode
  - (other loads disconnected)
- idle:
  - DC charger in idle mode
  - (other loads disconnected)
- open:
  - DC charger and all other loads
  - disconnected

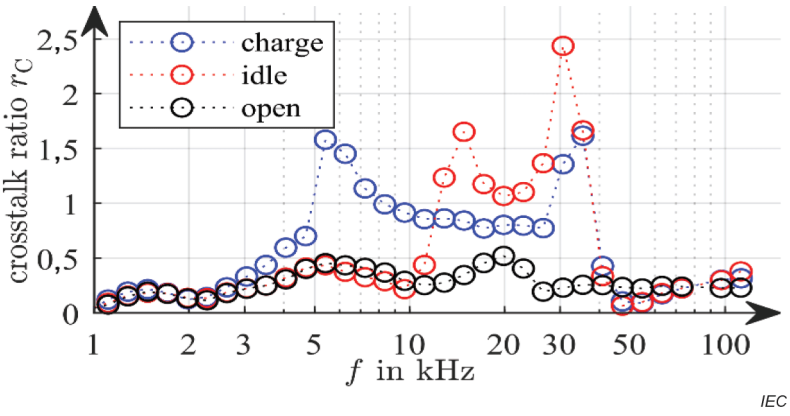

Figure 33 – Crosstalk ratio of supraharmonic voltage between phase L1 (phase of injection) and phase L2 at the junction box JB

- identical operating states as in Figure 33

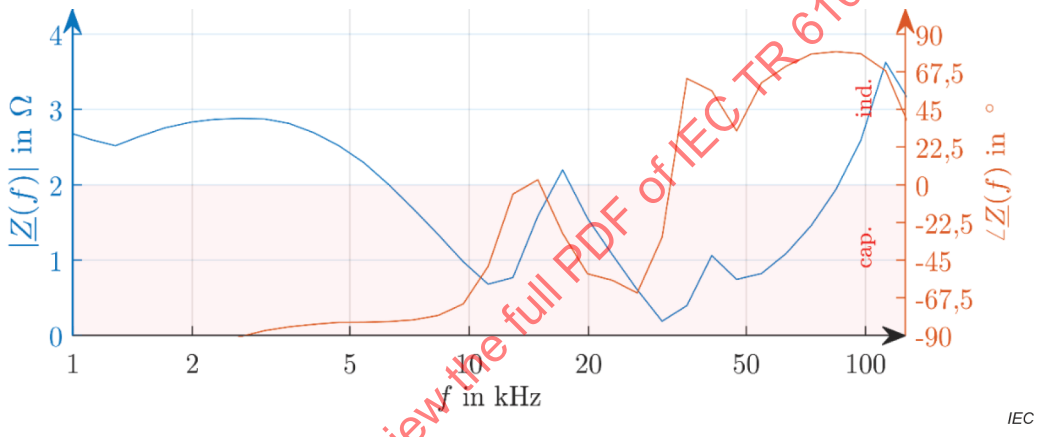

Figure 34 – Measured impedance (magnitude and phase) of the DC charger in idle mode

b) Three-phase injection

In a second experiment, the battery electric vehicle (switching frequency of 10 kHz) with which the resonance was firstly observed is used as a three-phase supraharmonic injection source at the transformer busbar BB. Figure 35 presents the results at 10 kHz for the highest individual spectral component (5 Hz resolution) and a group band of 2 kHz around the switching frequency. The three-phase injection results in transfer ratios twice as high compared with the single-phase injection. The deviation between phases results from the asymmetrical impedance conditions at the junction box JB. This means that a single-phase injection might not be representative for the case of a three-phase injection, for which a significantly higher amplification might be observed.

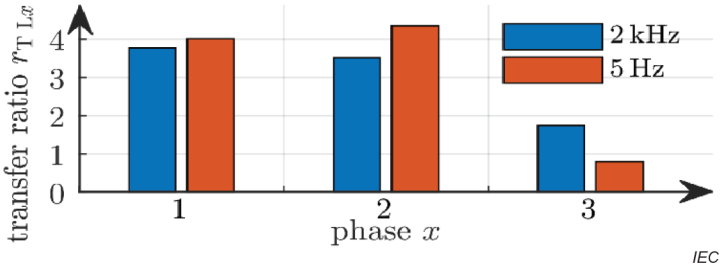

Blue: Highest individual spectral component (no grouping)

Red: Aggregation into 2 kHz bands

Figure 35 – Transfer ratio along the cable for all three phases in case of three-phase injection at the transformer busbar BB

5.2.3 Simulation results

In 5.2.3, the measured supraharmonic amplification presented in 5.2 is verified using simulations [17]. The fully coupled three-phase model used for these simulations is shown in Figure 36.The supraharmonic source is assumed as a single-phase, constant voltage U_T. The grid of the remaining phases is modelled as network loop impedances. The charger is also modelled as loop impedances, while ground potential and coupling with ground are neglected. The impedance of the DC charger is determined by measuring its three phase-to-neutral input impedances (phase L1-N is shown as an example in Figure 34).

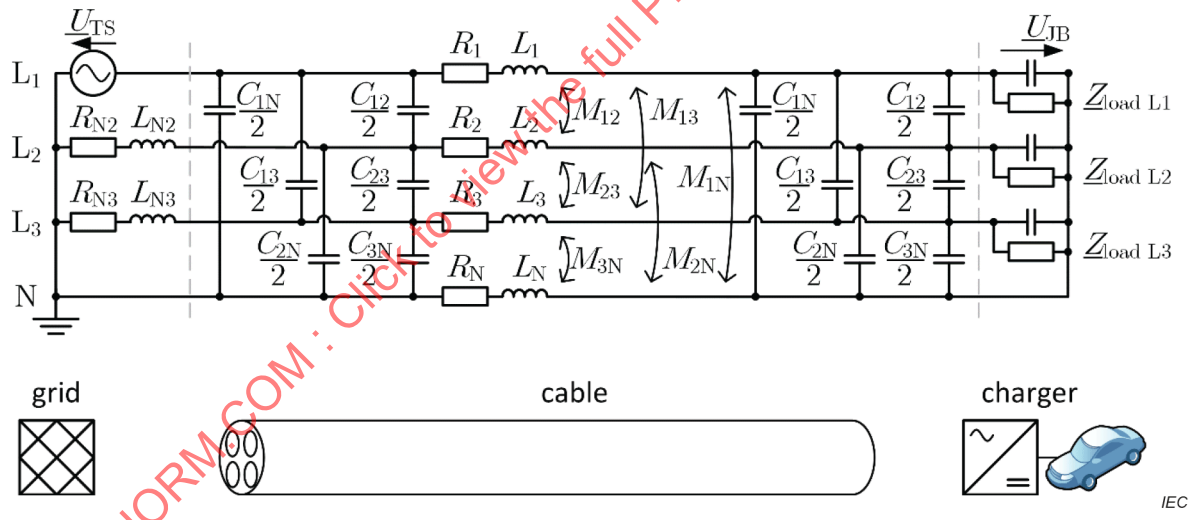

Figure 36 – Fully coupled three-phase simulation model

The line parameters of the cable are calculated using the finite element method (FEM) simulating the cable geometry. Due to the very short length of the cable (62 m), all capacitances can be neglected. The resistance of the cable increases with the frequency due to the skin effect. However, the increase is less than proportional, so that the cable impedance becomes nearly purely inductive above 5 kHz and the resistance can be neglected. The grid impedance in the phases L2 and L3 are determined by respective impedance measurements.

The simplified model is shown in Figure 37. The measured and simulated transfer ratio is shown in Figure 38. The results show a very good match between simulations and measurements up to the first resonance at 10 kHz.

In Figure 39 the transfer ratio is shown for simulations with varying cable length. For a higher resolution in the frequency, the measured input impedance of the DC charger is linearly interpolated. The amplification around 20 kHz is increasingly damped with increasing cable length and the amplification disappears for cable lengths larger than 150 m. The amplification at 10 kHz exists already for very short cable lengths. With increasing cable length, it shifts to lower frequencies (7 kHz at 300 m) while increasing in amplification. The low magnitude and highly capacitive input impedance of the charger results in pronounced resonances with highly amplified supraharmonic voltages across a wide range of frequencies and cable lengths.

The results confirm that especially in the downstream direction the input impedance of a device can have a significant impact on the supraharmonic voltage distortion. This in turn means that a certain control of the input impedance can efficiently avoid such unwanted supraharmonic resonance amplifications.

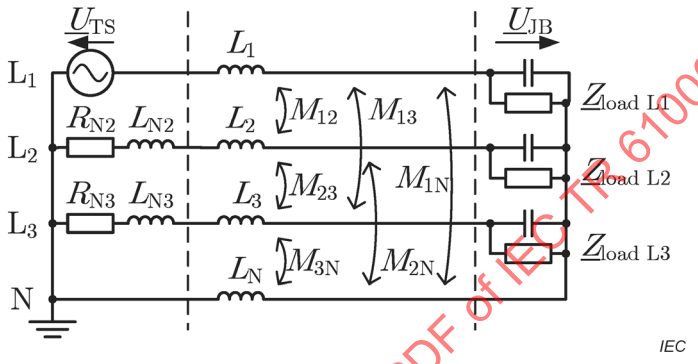

Figure 37 – Simplified simulation model for supraharmonic transmission along a low voltage cable

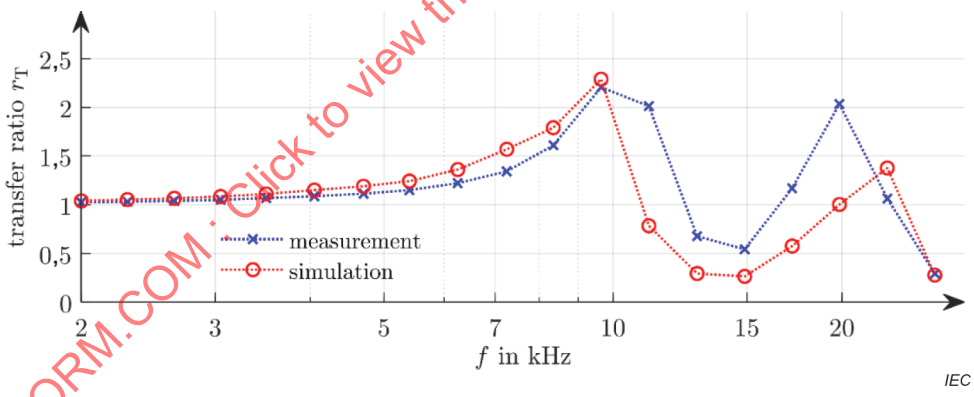

Figure 38 – Comparison of measured and simulated transfer ratios along a low voltage cable

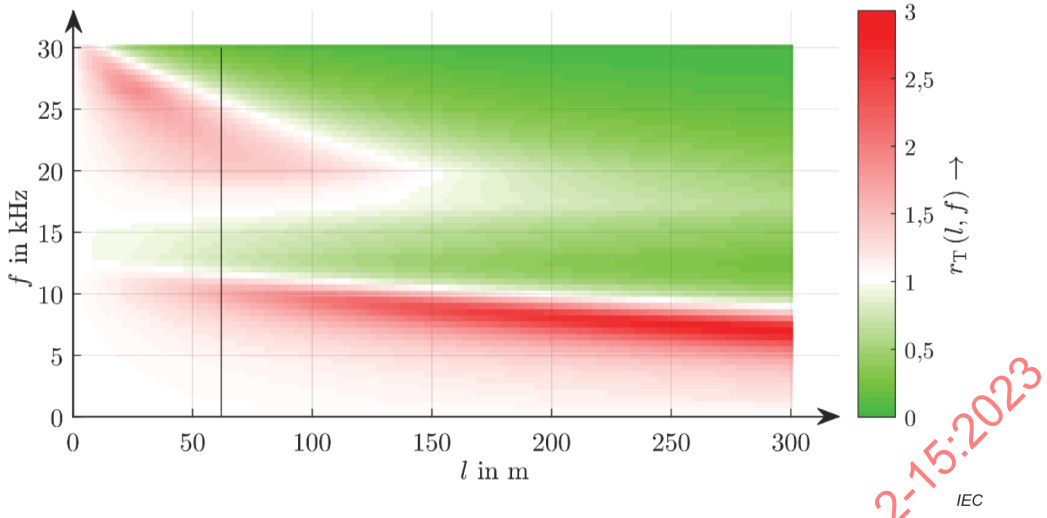

The red areas indicate amplification, the green areas indicate damping, the vertical line marks the original length of the cable.

Figure 39 – Transfer ratio of supraharmonic voltages along a low voltage cable of varying length

5.3 Supraharmonic amplification in a residential low voltage network with PV converters

The same procedure as used in 5.2.1 is also used to measure the propagation of supraharmonic voltages in a radial public low voltage network with residential customers (single-family houses with high penetration of rooftop PV installations). A sinusoidal current with variable frequency is injected into the grid, the resulting voltages at different locations are measured and the transfer ratio according to Formula (2) is calculated.

The grid consists of several feeders with several junction boxes distributed along them, which enable suitable access for measurements. Figure 40 presents the relevant part of the network as a single-line diagram. In two feeders the propagation of supraharmonic voltages is measured in the upstream direction (injection at open end JB3 and JB5, measurement at junction boxes JB2/JB1 (route I) and JB4/JB1 (route II)) and downstream direction (injection at junction box JB1, measurement at junction boxes JB2/JB3 (route I) and JB4/JB5 (route II)). Each route is approximately 200 m long with about 10 houses supplied along each route. About one-half of the houses is equipped with a photovoltaic rooftop system.

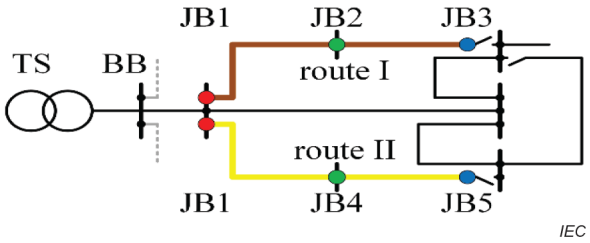

Figure 40 – Single-line diagram of the analysed low voltage network, two routes, and measurement locations on each route in red, green and blue

Figure 41 shows the measured transfer ratios along the two routes. In the upstream direction, a significant damping is observed at all frequencies and in all sections of both routes. In the downstream direction, however, significant amplification of supraharmonic voltages by a factor of 1,8 (route I) and 1,6 (route II) is observed. These resonances are located at relatively low frequencies between 4 kHz and 6 kHz.

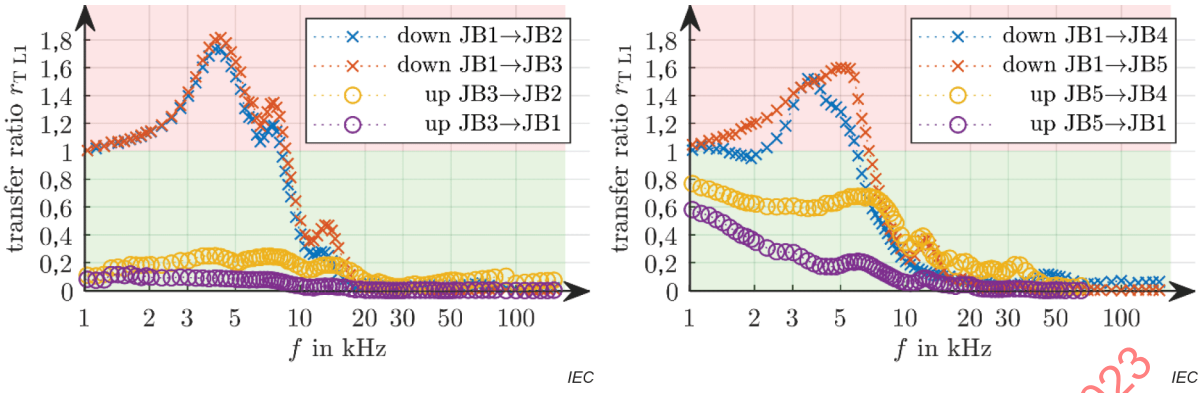

Figure 41 – Transfer ratios along two routes in a low voltage network with residential customers, upstream direction as circles, downstream direction as crosses

Similar to the case explained in 5.2, the amplification is mainly caused by the capacitive input characteristic of the equipment connected in the single-family houses. In particular, modern power electronics based on self-commutating topologies (e.g. PV converter, electric vehicle charger) require grid-side filter circuits introducing (distributed) capacitance to the network, which compose resonances in the supraharmonic range. Consequently, the introduction of requirements for the input impedance characteristic of electronic equipment might be considered in the future. As shown in this case study, the probability of downstream supraharmonic resonances is significant. As stronger supraharmonic emission sources (e.g. central charging infrastructures) are more likely to be connected close to the transformer busbar BB, this phenomenon can be considered in defining emission limits, in order to fairly share the risk of too high disturbance levels between network operators and manufacturers.

5.4 Generic supraharmonic emission models for PWM based converters

a) Single-phase power converters

Supraharmonic emission of single-phase, hard-switching, self-commutated, voltage-source power converters can be modelled using Thévenin equivalent circuits. This is shown for the design process of the AC side filter network of voltage source power converters in [11]. The two-level converter and the filter network are simplified to a Thévenin equivalent circuit consisting of a voltage source and a complex impedance. Black-box models are parameterized based on measurements and do not require information about internal circuit layout and control algorithms, which is usually not disclosed by the manufacturers. The same approach using a voltage source and impedance is used for qualitative analysis in [12] and for quantitative analysis in [14],[15]. The Thévenin equivalent circuit of a single-phase voltage-source power converter connected to a low-voltage network is shown in Figure 42. The validation measurements in [14], [15] and [16] show typical errors of such black-box models of less than ±5%. With high confidence, the errors do not exceed ±10 %.

This black-box model approach is based on representing the energy around integer multiples of the PWM carrier frequency into individual emission bands within a narrow frequency range represented by a single source. The grouping is performed by the root sum square, which corresponds to an energy equivalence and is used in IEC 61000-4-7:2002/AMD1:2008 [65], Annex B. A group band of B = 800 Hz is considered as an optimal size for pulse-width modulated power converters with a static carrier frequency. The approach will likely work on any group band size, for example of 200 Hz as used as default band in IEC 61000-4-7:2002/AMD1:2008 [65], Annex B. However, wider group sizes make measurements more robust against leakage and frequency shifts and reduce the overall complexity of the resulting models.

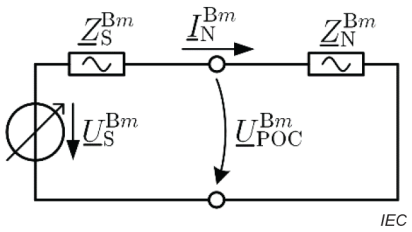

$\underline{Z}_S^{Bm}$	source impedance
$\underline{Z}_N^{Bm}$	network loop impedance
$\underline{U}_S^{Bm}$	emission band source voltage
$\underline{U}_{POC}^{Bm}$	emission band voltage at POC
$\underline{I}_{POC}^{Bm}$	emission band current at POC

Figure 42 – Equivalent circuit (model) for the supraharmonic emission of single-phase voltage-source power converters for the m^{th} emission band

The source voltage depends on the AC voltage, DC voltage, active power output and AC distortion, as shown as an example in Figure 43.

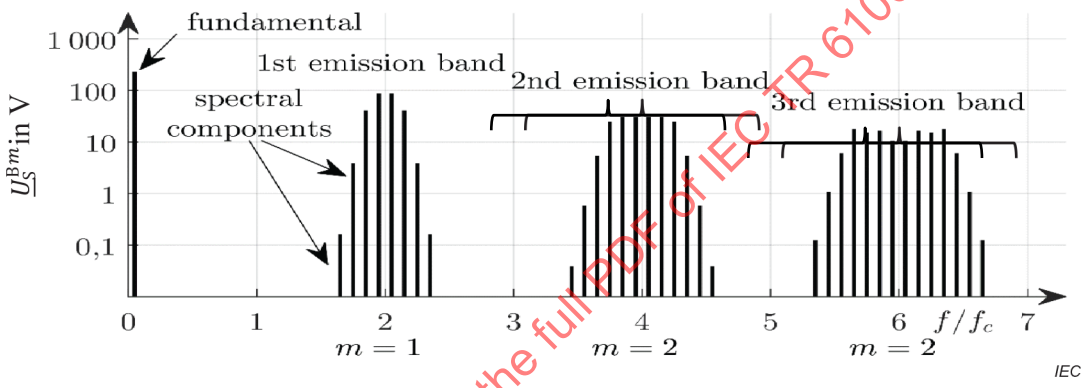

f_c is the carrier frequency, m is the order of the emission band.

Figure 43 – RMS voltage spectrum U_S at the output terminals of a single-phase power converter H-bridge using unipolar PWM

b) Three-phase power converters

As of now, no black-box models for the supraharmonic emission of true three-phase power converter topologies have been published.

5.5 Assessment of optimal impedance angles for power electronic devices to minimize risk of amplification

Based on the equivalent circuit presented in Figure 42, a resonating behaviour can also be caused by the interaction of the source impedance of an emitting device (power converter) itself and the grid. The supraharmonic voltage, in an emission band at the POC of a single device, can be calculated as:

$$\underline{U}_{POC}^{Bm} = \underline{U}_S^{Bm} \cdot \frac{\underline{Z}_N^{Bm}}{\underline{Z}_S^{Bm} + \underline{Z}_N^{Bm}} \tag{4}$$

When the device is connected to the network, two cases can be distinguished:

1) The voltage at the POC $\left|\underline{U}_{POC}^{Bm}\right|$ is smaller than the source voltage $\left|\underline{U}_S^{Bm}\right|$. This is considered a damped or non-resonating case. The minimum voltage at the POC is obtained, if the two impedances have the same phase angles.

2) The voltage at the POC $\left|\underline{U}_{\mathrm{POC}}^{\mathrm{B}m}\right|$ is greater than the source voltage $\left|\underline{U}_{\mathrm{S}}^{\mathrm{B}m}\right|$. This is considered an amplified or resonating case. The maximum voltage at the POC is obtained, if the two impedances have opposite phase angles.

Case 1 can be considered as a rather “grid-friendly behaviour”, while case 2 represents a rather “grid-unfriendly” behaviour. However, the magnitude of the POC voltage depends also significantly on the magnitude of the source voltage and the magnitude ratio of the impedances, so that the final impact on the grid has to be assessed by considering both the source voltage and the impedance configuration.

The border case between damping and amplification is located on a line in the complex impedance plane, where the real part of the ratio of the two impedances $\underline{Z}_{\mathrm{N}}^{\mathrm{B}m}$ and $\underline{Z}_{\mathrm{S}}^{\mathrm{B}m}$ is -1/2.

$$\left|\frac{\underline{U}_{\mathrm{POC}}^{\mathrm{B}m}}{\underline{U}_{\mathrm{S}}^{\mathrm{B}m}}\right| = 1 \;\rightarrow\; \mathrm{Re}\left(\frac{\underline{Z}_{\mathrm{N}}^{\mathrm{B}m}}{\underline{Z}_{\mathrm{S}}^{\mathrm{B}m}}\right) = -\frac{1}{2} \tag{5}$$

Curves of constant voltage at the POC $\underline{U}_{\mathrm{POC}}^{\mathrm{B}m} = \mathrm{const.}$ exist in the complex impedance plane of $\underline{Z}_{\mathrm{N}}^{\mathrm{B}m}$. These locus curves for $\underline{U}_{\mathrm{POC}}^{\mathrm{B}m} = \mathrm{const.}$ are circles.

$$\underline{Z}_{\mathrm{N}}^{\mathrm{B}m} = \underline{M} + r \cdot \mathrm{e}^{\mathrm{j}\varphi} \qquad 0 \le \varphi < 2\pi \tag{6}$$

with

$$\underline{M} = \underline{Z}_{\mathrm{S}}^{\mathrm{B}m} \cdot \frac{\left|\underline{U}_{\mathrm{POC}}^{\mathrm{B}m}\right|^2}{\left|\underline{U}_{\mathrm{S}}^{\mathrm{B}m}\right|^2 - \left|\underline{U}_{\mathrm{POC}}^{\mathrm{B}m}\right|^2} \tag{7}$$

$$r = \left|\underline{Z}_{\mathrm{S}}^{\mathrm{B}m}\right| \cdot \frac{\left|\underline{U}_{\mathrm{POC}}^{\mathrm{B}m} \cdot \underline{U}_{\mathrm{S}}^{\mathrm{B}m}\right|}{\left|\underline{U}_{\mathrm{S}}^{\mathrm{B}m}\right|^2 - \left|\underline{U}_{\mathrm{POC}}^{\mathrm{B}m}\right|^2} \tag{8}$$

The described characteristics of the ratio between $\left|\underline{U}_{\mathrm{POC}}^{\mathrm{B}m}\right|$ and $\left|\underline{U}_{\mathrm{S}}^{\mathrm{B}m}\right|$ and its dependency on the impedances are illustrated in Figure 44.

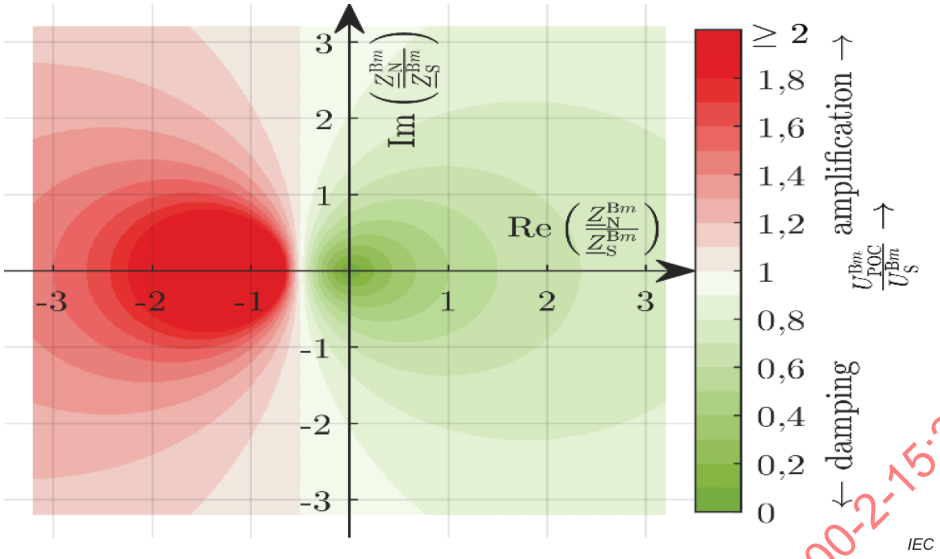

Figure 44 – Amplification and damping of supraharmonic emission at the POC relatively to the source voltage depending on the network to source impedance

Using Formula (7) and Formula (8), plots (nomograms) can be created from which the voltage at the POC can be directly obtained for a particular configuration of the source voltage, the source impedance and the network impedance at the considered emission band. Such nomograms are illustrated as examples for two photovoltaic inverters in Figure 45. More details about the inverters, including the parameters (source voltage and source impedance for the considered emission band), can be found in [14],[26]. For both plots the maximum possible source voltage $\left|\underline{U}_S^{Bm}\right|$ is assumed, which is the required practice in accordance with the CISPR 16 series. Regarding the network impedance, a total of 187 measured network loop impedances from [19] are used to get an idea about the range of voltage magnitudes to be expected under different realistic grid impedance conditions (red dots in Figure 45).

The best overall behaviour of a device with respect to the variation in the network impedances is achieved, if the angle of the source impedance of the device is located in the centre of the possible network loop impedance angles. This can be estimated calculating the prevailing phase angle of all network loop impedances $\angle\Sigma\underline{Z}_N^{Bm}$ (angle of the sum of all measured network loop impedances) which is indicated in Figure 45 as blue dotted line.

For inverter A (see Figure 45) the maximum POC voltage reaches 2,24 V at a maximum source voltage of 6,5 V. This represents a generally good damping of the source voltage by about a factor of 3, which is caused by the good matching impedance angles. On the other hand, for inverter B (see Figure 45) the maximum expected POC voltage reaches 1,94 V at a source voltage of 1,93 V. This represents no damping and virtually no amplification of the source voltage. Nevertheless, the expected POC voltage for inverter A is higher than for inverter B due to the higher source voltage of inverter A. This confirms that the final level of “grid-friendliness” of a device depends on the magnitude of the source voltage, the ratio of impedance magnitudes and the difference in impedance angles.

The frequency-dependency of the prevailing phase angle of the network loop impedance is shown in Figure 46. It is approximately 45° inductive at 10 kHz and 60°inductive at 20 kHz and above. This behaviour suggests that the impedance of a power converter at the centre frequency of its dominant emission band would rather be resistive-inductive to minimize its contribution to the supraharmonic voltage distortion in the grid. However, the number of analyzed measurements is limited. Further, all measurements are taken at LV transformer busbars (1/3 of the measurements) and junction boxes with different distance to the transformer busbar (2/3 of the measurements), but not directly at household terminals. Therefore, the conclusions above are more representative of larger converters. For converters usually applied in households, further studies on the network impedance characteristics are required for reliable suggestions on a preferred range for the source impedance angle.

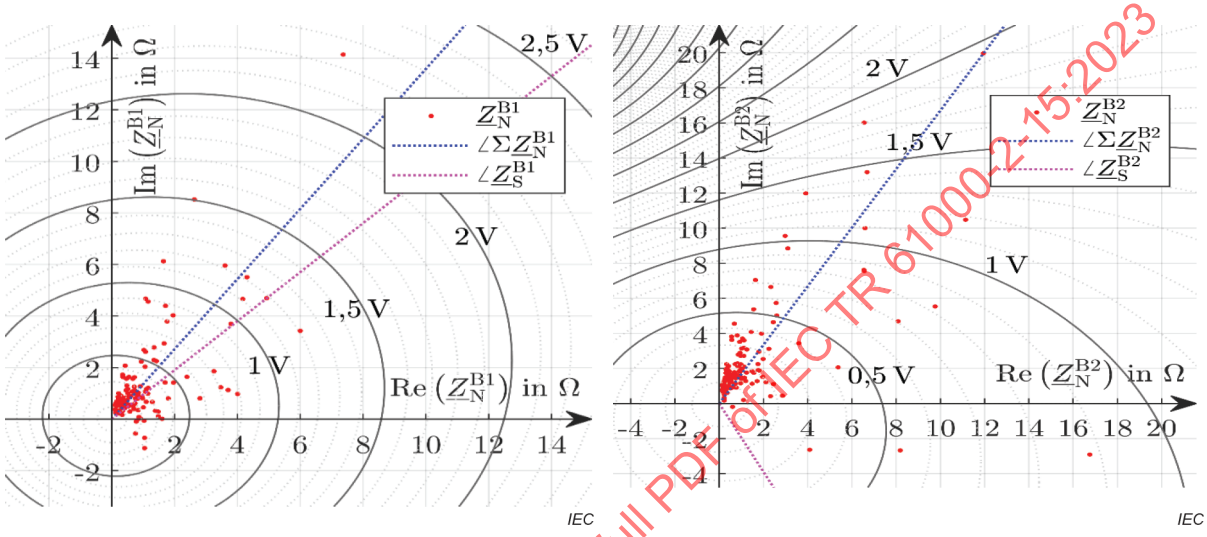

a) inverter A, 1st emission band at 16 kHz

b) inverter B, 2nd emission band at 36 kHz

Figure 45 – Circles of constant POC voltage in the dominant emission band of two photovoltaic inverters [29]

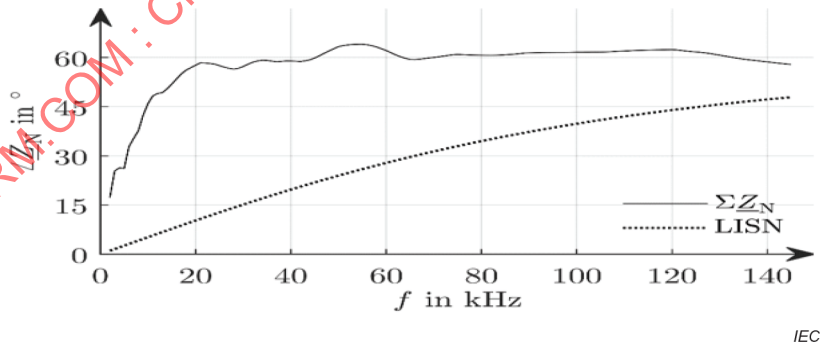

Figure 46 – Prevailing phase angle of 187 measured network loop impedances [34]between 2 kHz and 150 kHz, phase angle of the line impedance stabilization network from CISPR 16-1-2

6 Cases of a large amount of converters

6.1 General

The expansion of renewables and smart grids leads to a growing number of power electronics conversion stages in the distribution grid. Due to their electronic design, power supplies, batteries, heat pumps and solar inverters as well as frequency inverters inject in the grid a non-sinusoidal current and influence the frequency-dependent grid impedance (FdGI).

Consequently, non-intentional emissions and resonance effects can occur in the frequency bandwidth between 2 kHz to 150 kHz (see Figure 47, Figure 48 and Figure 49), which highly affect the power quality by distorting the voltage and by even leading to instabilities [12], [20], [21] and [22]. Furthermore, the lifetime of the components affected by such disturbances can be significantly reduced. This case is described in [20].

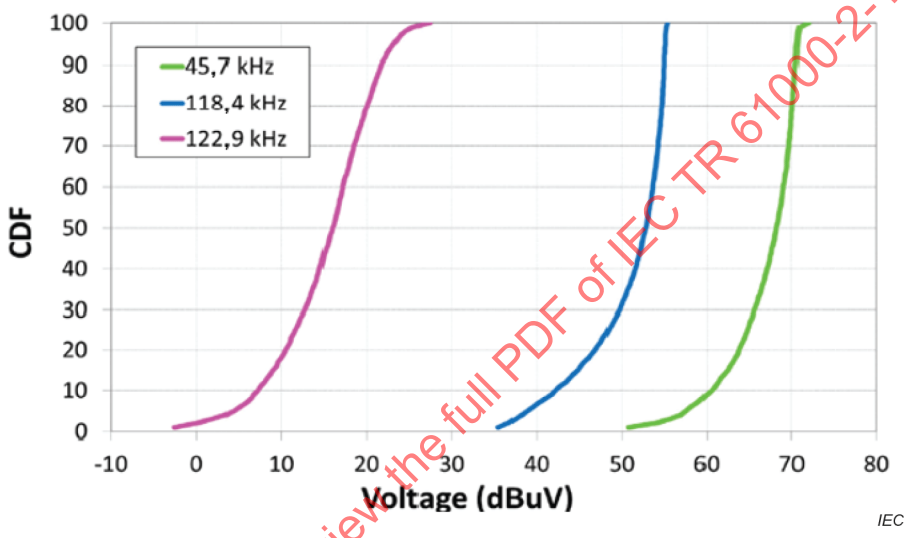

Figure 47 – Cumulative distribution function (CDF) of non-intentional emissions due to distributed energy sources at two different frequencies (45,7 kHz and 118,4 kHz) and noise present in the electrical grid (122,9 kHz)

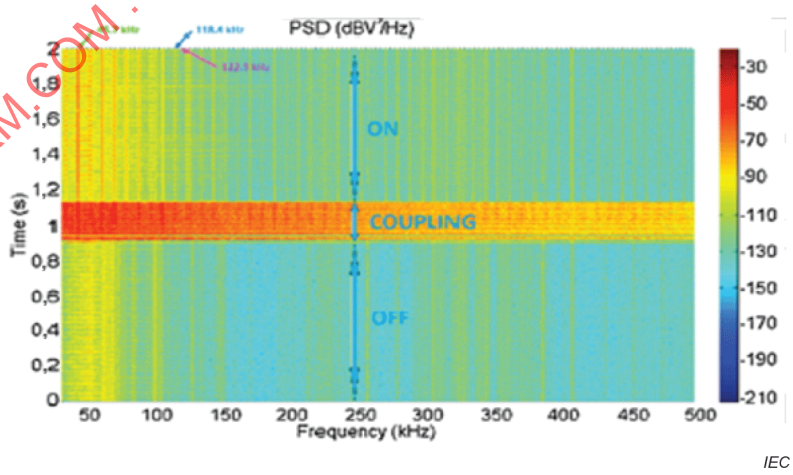

Figure 48 – Identification of the frequencies in the frequency response

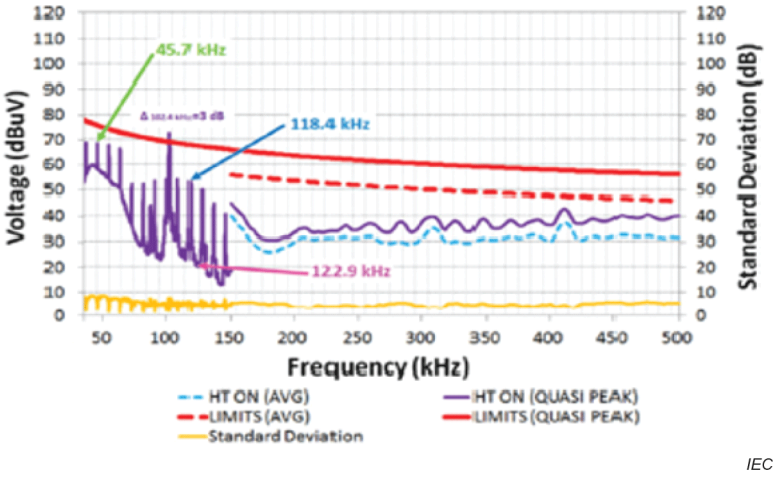

Figure 49 – Identification of the frequencies in the spectrogram of the measurements (see case study [23])

Furthermore, power electronics converters connected to the grid are typically equipped with an LCL filter to provide sufficient harmonic attenuation and with an EMI filter, according to the application requirements. Installations featuring several converters connected in parallel and requiring static reactive compensation by capacitor banks typically show additional resonance peaks in the frequency ranges 2 kHz to 9 kHz and 9 kHz to 150 kHz due to the interactions of parallel-connected filters stages.

In addition, especially with large installations, they might be built over a long period of time, which means that there can well be grid-connected converters equipped with different types of filters and different ratings in parallel. This leads to different grid filter parameters, hence to differences in the resonance frequencies of the system over the time [27].

6.2 Large PV installations

The conventional discussion about the resonance problem caused by LCL filters is mainly based on a single converter system. In the practical application, due to the distributed characteristic in a renewable energy system, multiple converters would be considered. The converters are commonly connected in parallel to meet the increased power-rating requirement. It is noted that due to cost issues, many small inverters may be used instead of a single larger one. Therefore, installations with multiple converters need to be considered as well as installations using multiple micro-inverters in parallel.

Therefore, the analysis of the resonance problem can be expanded to parallel LCL filters. Meanwhile, considering local reactive power compensation, the resonance frequency is further influenced by the capacitor connected to the common bus.

In solar farms, multiple converters are connected in parallel. Figure 50 represents the case of a large PV farm [26].

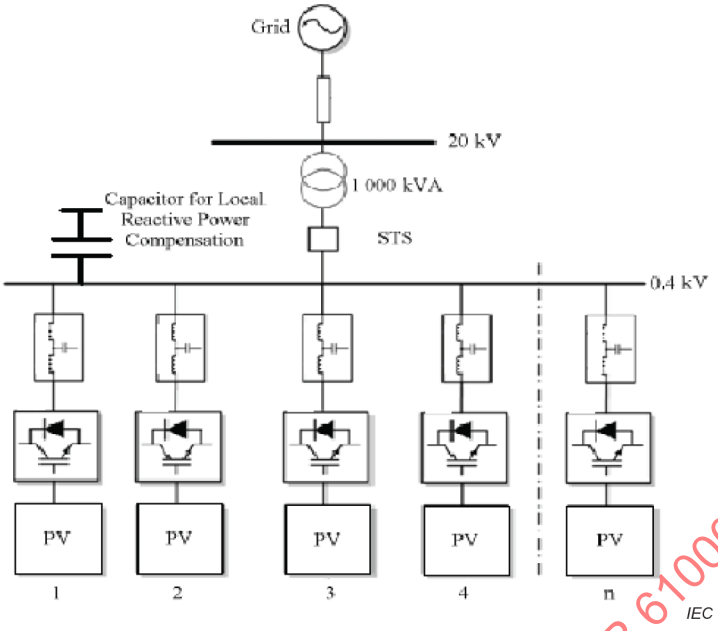

Figure 50 – Parallel-connect configuration in large photovoltaic (PV) farm

For the sake of convenience, a parallel system with two converters in parallel with a capacitor for reactor compensation C_Q and closed on a common grid impedance L_g is considered in Figure 51 [26],[27]. The Bode plots of the resulting systems resonances are shown in Figure 52. In the lower frequency range, a resonance and anti-resonance appear due to the effect of the capacitor for reactive compensation. In the upper frequency range, two resonance peaks instead of one are due to the two LCL filters in parallel. By adding to the circuit other branches in parallel, the number of poles of the system's transfer function will increase, hence the number of resonances.

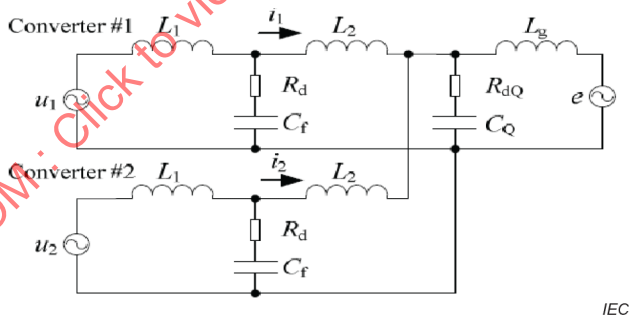

Figure 51 – Simplified parallel of two converters featuring LCL filter and capacitor on common bus for reactive compensation in the grid (see Table 7)

Table 7 – Values of the system parameters [23]

Inv-side Inductance L_1 (mH)	1,8	Filter Capacitor C_f (µF)	4,7	Reactive power comp. cap. C_Q (µF)	20	Passive damping Resistance R_{dQ} (Ω)	0 ~0,6
Grid-side Inductance L_2 (mH)	1,8	Grid Inductance L_g (mH)	2	Passive damping Resistance R_d (Ω)	0 ~0,6		

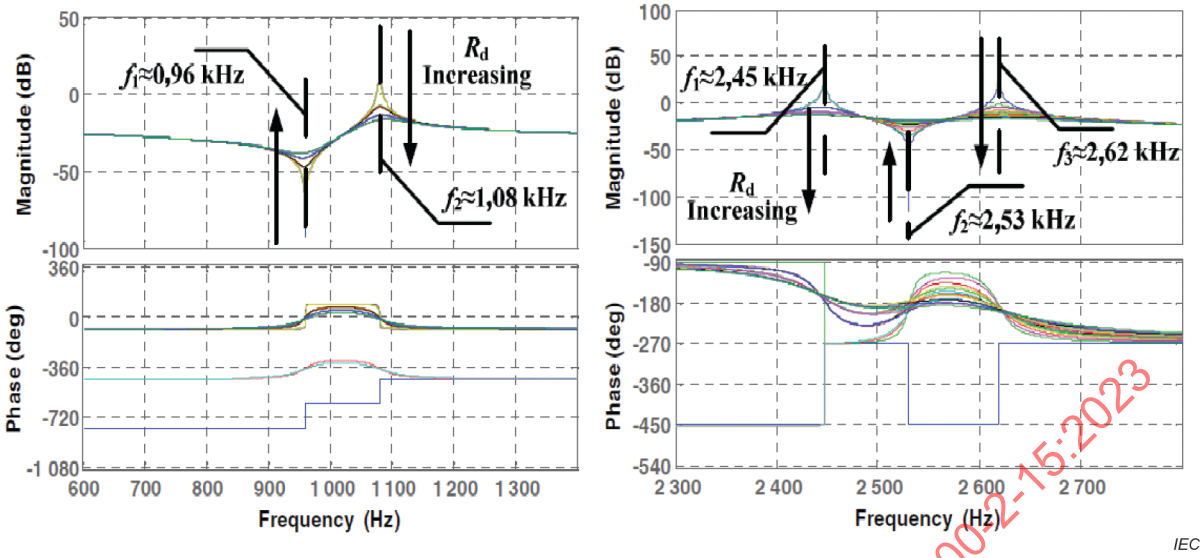

Figure 52 – Frequency domain results of parallel LCL filter system with reactive power compensation capacitor represented in two frequency ranges

The blue lines in Figure 52 are the phase curves at the asymptote. The values of magnitude and phase are neither mentioned in Figure 52 nor in the reference.

In the lower frequency range, the resonance and anti-resonance are due to the effect of the capacitor for reactive compensation; in the upper frequency range, the two resonance peaks are due to the two LCL filters in parallel [23].

The value of the resonance frequency is dependent on the grid impedance. Changing the grid impedance leads therefore to drift the resonance frequencies in the system. On one side this decreases the performance of the control and the efficiency of the system; on the other side, this can lead to unexpected consequences in terms of decreased power quality.

For a system of N parallel connected inverters equipped with LCL filter interfaces connected to a common grid impedance (see the equivalent circuit in Figure 53), each individual inverter sees an equivalent grid impedance, proportional to the grid inductance multiplied by N, where N is the number of parallel inverters [24]. This means that a system of N parallel inverters equipped with LCL filters is more sensitive to variations in grid impedance, as illustrated in Figure 54. In order to test the position of the resonant peak, a disturbance term can be added to the current control loop to give an excitation of different frequencies, as in Figure 55. For an LC-filter topology instead, for N parallel inverters, as in the case of LCL-filter interface, the common grid-side inductor seen from each individual inverter is equal to the original grid side inductor multiplied by N. This decreases the sensitivity to grid variations, if the grid-side inductor is larger than the grid inductance [23].

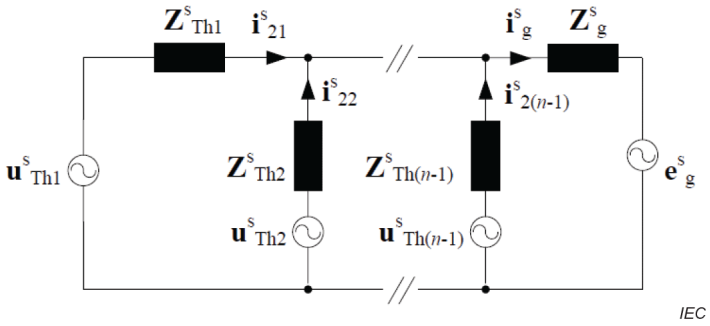

$Z_{Th\,s} = Z_{L2\,s} + (Z_{L1\,s} \,||\, Z_{C\,s})$; L1 inverter side inductor; C filter capacitor, L2 grid side inductor [24].

Figure 53 – N parallel connected equivalent inverter models equipped with LCL filter interfaces connected to common grid impedance Z_g as parallel connection of Thévenin's equivalent voltage sources and equivalent impedances

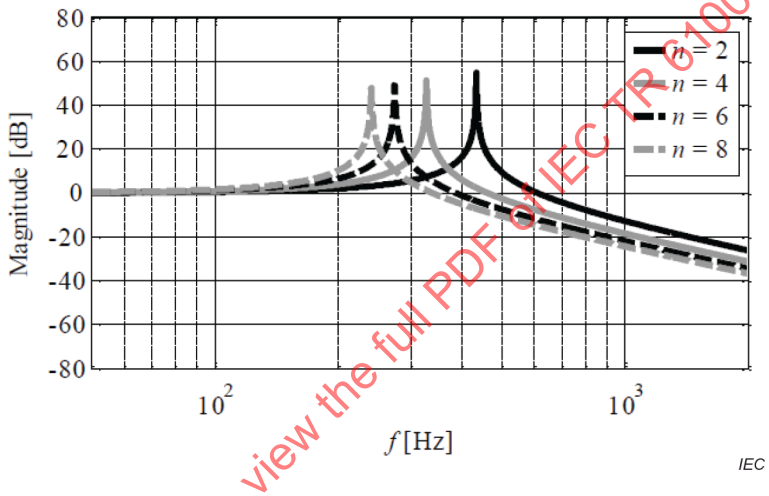

Figure 54 – Change in Bode plot of i_{sg}/i_{s11} (ratio of grid and inverter side currents respectively) or LCL-filter topology when the number of parallel connected inverters n increases from 2 to 8 with increments of 2

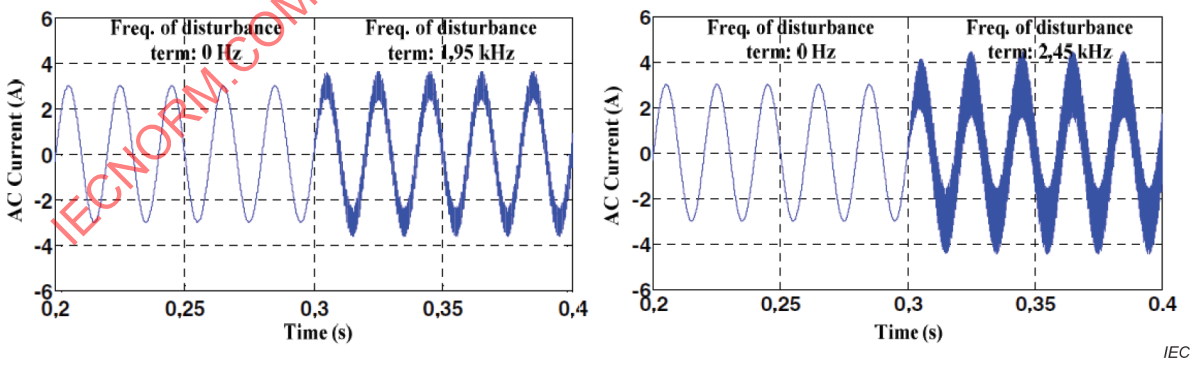

Figure 55 – Time domain simulations of parallel LCL system without reactive power compensation capacitor dependent on (in dependency of) a small sinusoidal disturbance term added in the control loop – Duty cycle

The plots show how a slow change of the disturbance term leads to the excitation of different frequencies, which is used to identify the position of the resonant peak [24].

A frequency dependent grid impedance measured at a 2,1 MW PV plant with 59 inverters shared on two roofs [29] can be considered as an illustration of this. FdGI measurements in the lower frequency range with different inverter configurations are represented in Figure 56. The dashed curves have been measured at the MV/LV transformer station (TS) and solid curves at the point of common connection of the inverters. It can be noted that the magnitude of the impedance is increasing at the frequency of the main parallel resonance at about 2 kHz, when adding working inverters to the system. The power line impedance measured between 1 kHz and 200 kHz is presented in Figure 57. The magnitude of the impedance is decreasing at the frequency of the main series resonance and a shift of the resonance frequencies towards lower frequencies at the point of connection is observed, when the number of working inverters increases.

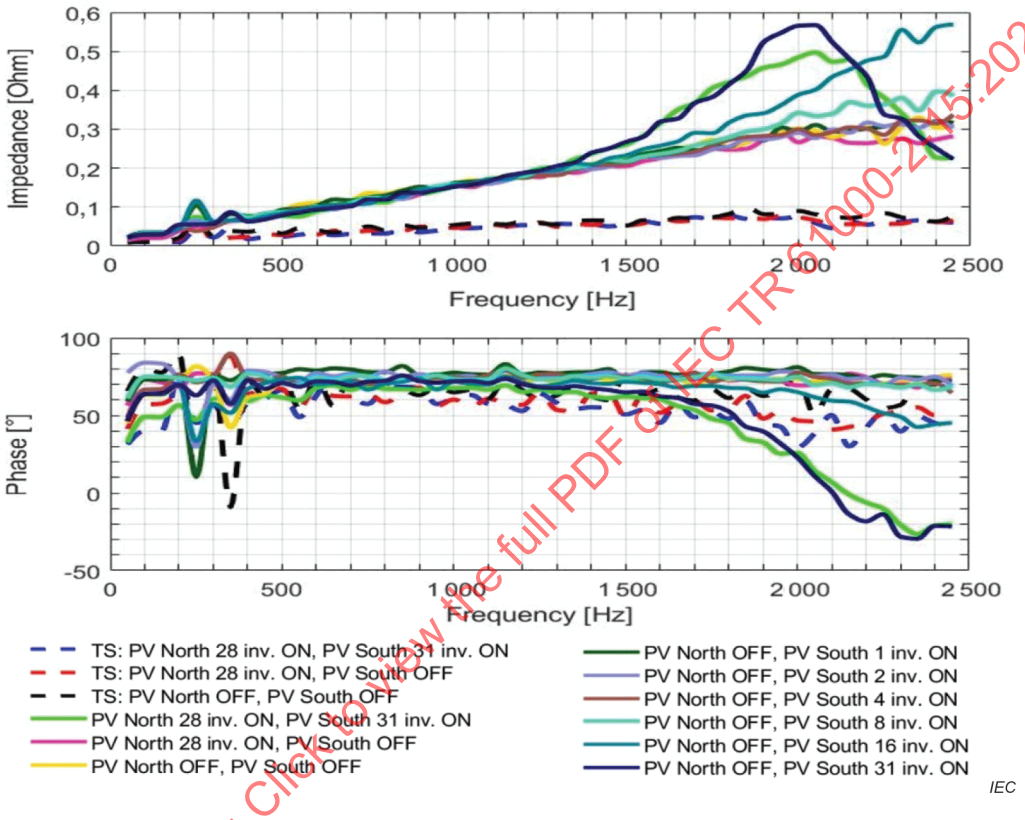

Figure 56 – Power line impedance in lower frequency range measured with 0 to 59 inverters activated in a 2,1 MW PV plant

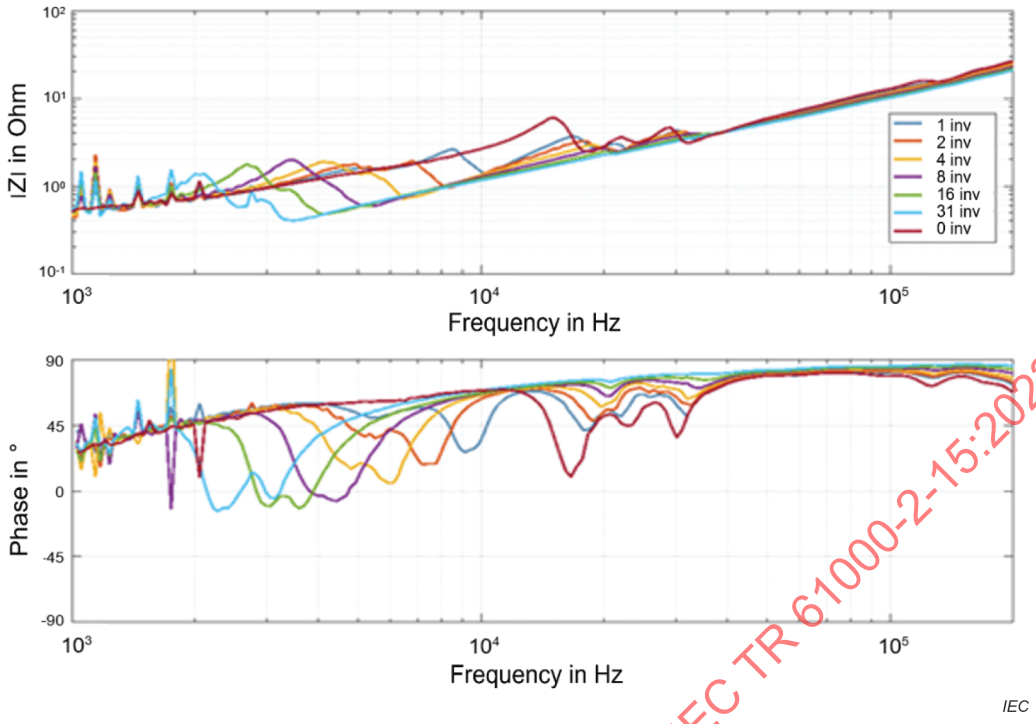

Figure 57 – Power line impedance measured with 0 to 59 inverters activated in a 2,1 MW PV plant

Considering the low frequency range, a parallel resonance with a small impedance increase at a frequency below 1,5 kHz is commonly observed in most of the measured LV grid situations. In the case of parallel connection of a large number of inverters, the value of the impedance at resonance is doubled and the resonance frequency is moving toward the frequency below 2 kHz. In this case, the chances for the following phenomena to occur are increasing:

- loss of stability of converters controller due to the increase of line impedance at critical frequency for the converter controller, as described in Clause 7;
- increase of the parallel resonance and resulting boost of voltage oscillations as described in Clause 4.

Considering the high frequency range, a non-predictable and time-variating reduction of the line impedance can result in:

– attenuation of power line communication signals used by smart meters in the CENELEC A band;

– increase of supraharmonics current exchanges between converters and EMC filters, as described in Clause 5.

6.3 Industrial grids

A three-phase industrial grid is typically constituted by several active loads represented by variable speed drives. Due to the heterogeneous nature of such installations, power inverters of different ratings and manufacturers are interfaced to the feeder through passive or active rectifier systems equipped with L, LC, LCL filters, with EMI filters according to the application requirements and cables of different length, shielded or unshielded, as depicted in Figure 58 [25]. This scenario leads to several types of interactions between power electronics systems within the industrial grid (see Figure 59) and to the generation of non-intentional emissions in the frequency range of 2 kHz to 150 kHz [54].

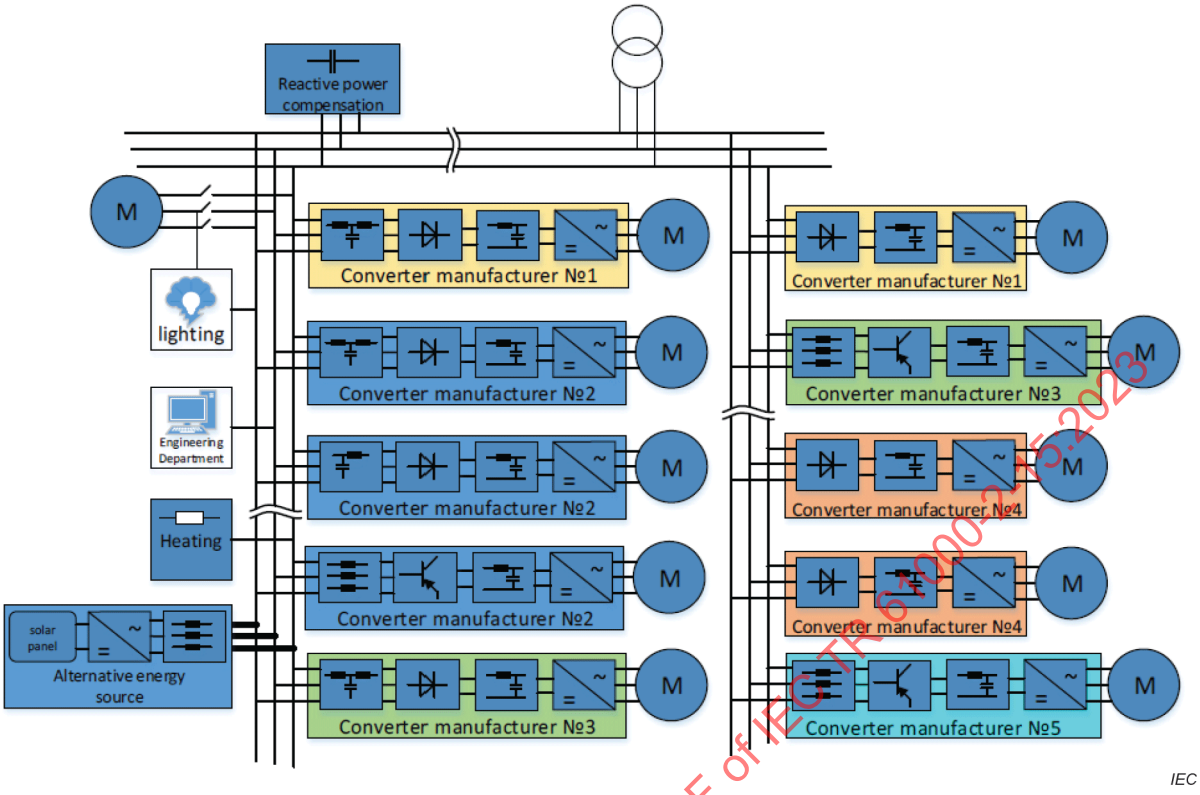

Figure 58 – Configuration of an industrial grid

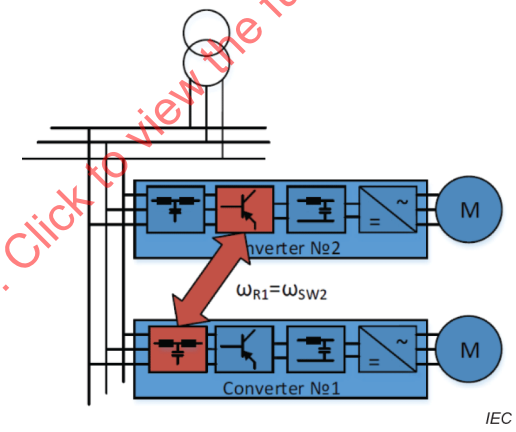

Figure 59 – Interaction between two converters, which can lead to resonances and generate non-intentional emissions in the 2 kHz to 150 kHz frequency range

The simplest configuration of interaction is made up of a noise source and noise sink (see Figure 60), constituted by two different converters, where the EMI filter of the sink converter can be, for instance, of the 2nd, 3rd or 4th order [25].

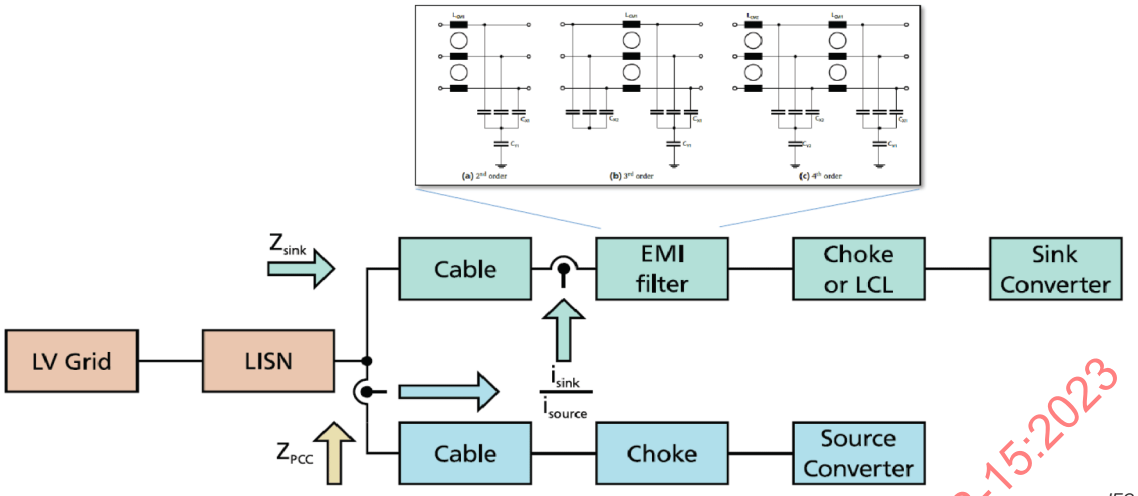

Figure 60 – Modeling of a simple configuration of noise source and noise sink, where the EMI filter of the sink converter can be of 2nd, 3rd or 4th order [25]

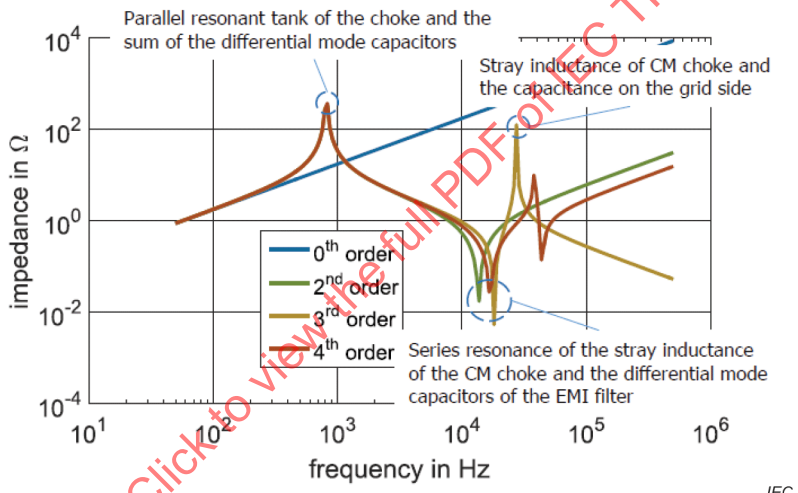

a) differential mode impedance

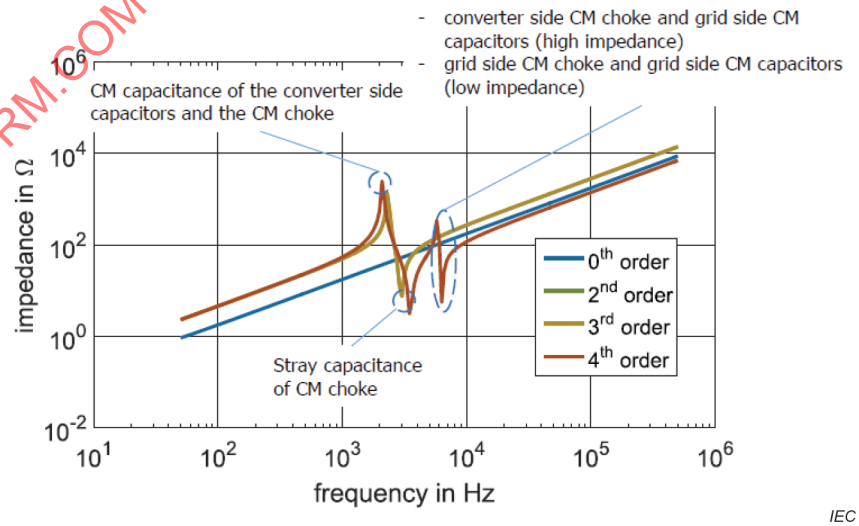

b) common mode impedance

Figure 61 – Impedance into the noise sink converter Z_{sink} with different EMI filter types with simple choke interface only and different EMI filter configurations

Figure 61 and Figure 62 represent the impedance into the noise sink converter Z_{sink} with different EMI filter types with simple choke interface and with LCL filter, respectively, and highlight the number and types of resulting resonances, which can lead to the generation of disturbances [25].

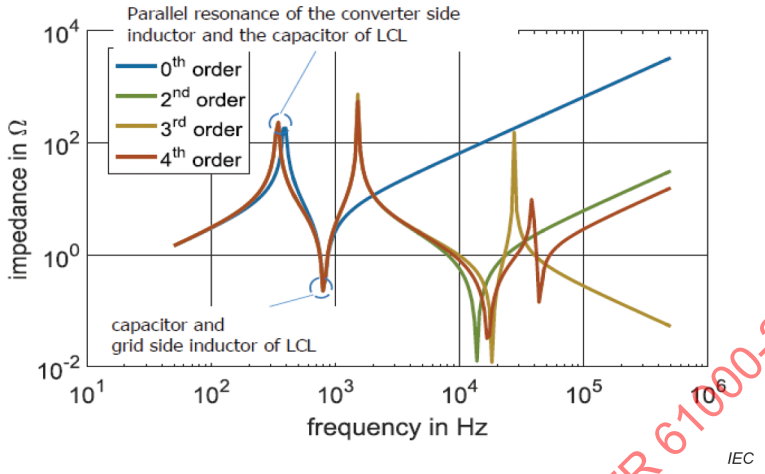

a) differential mode impedance

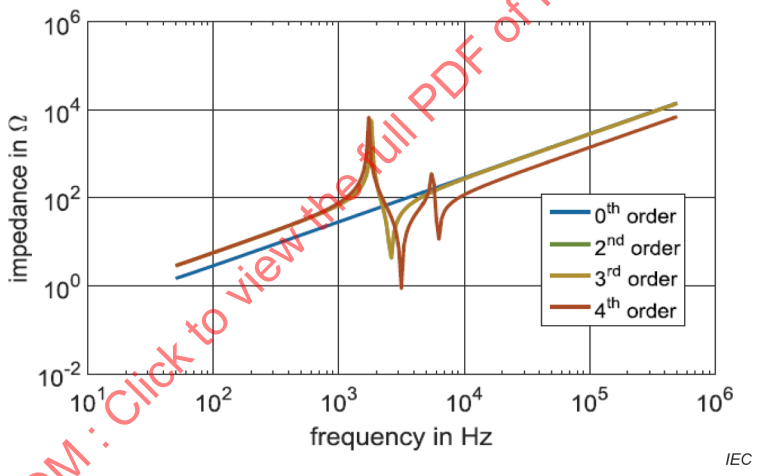

b) common mode

Figure 62 – Impedance into the noise sink converter Z_{sink} with different EMI filter types with LCL interface and different EMI filter configurations

Furthermore, the length and type of cables, shielded or unshielded, has also a crucial influence on the generation of disturbances in the frequency range of 2 kHz to 150 kHz.

As cables introduce asymmetry, the voltages and currents at the PCC will contain common mode and differential mode signals although the excitation at the noise source converter is purely common mode or differential mode, as depicted in Figure 63:

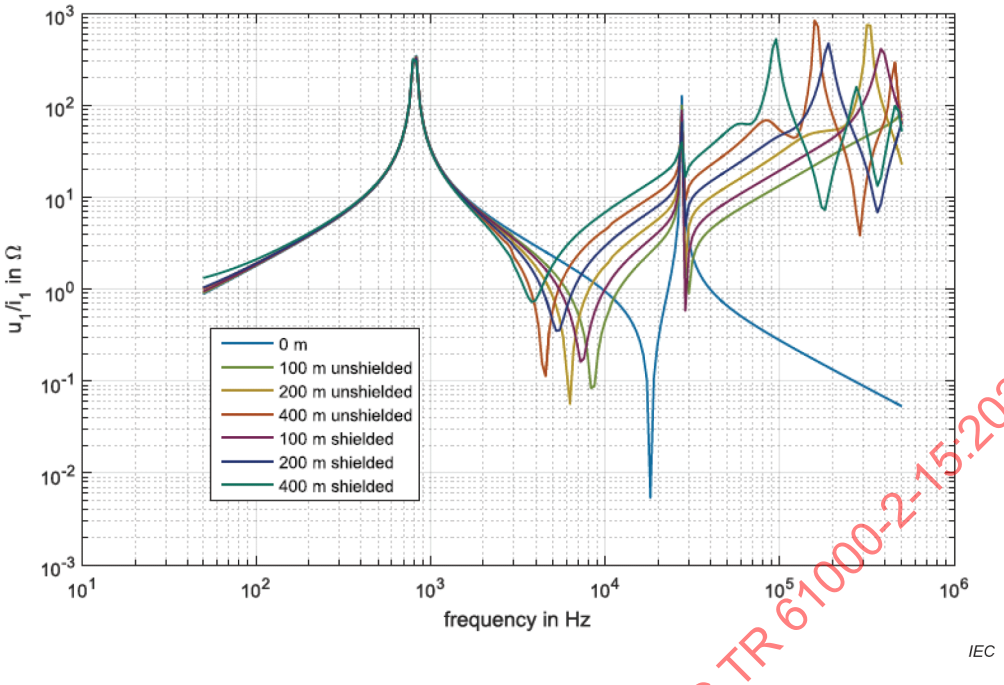

a) DM excitation

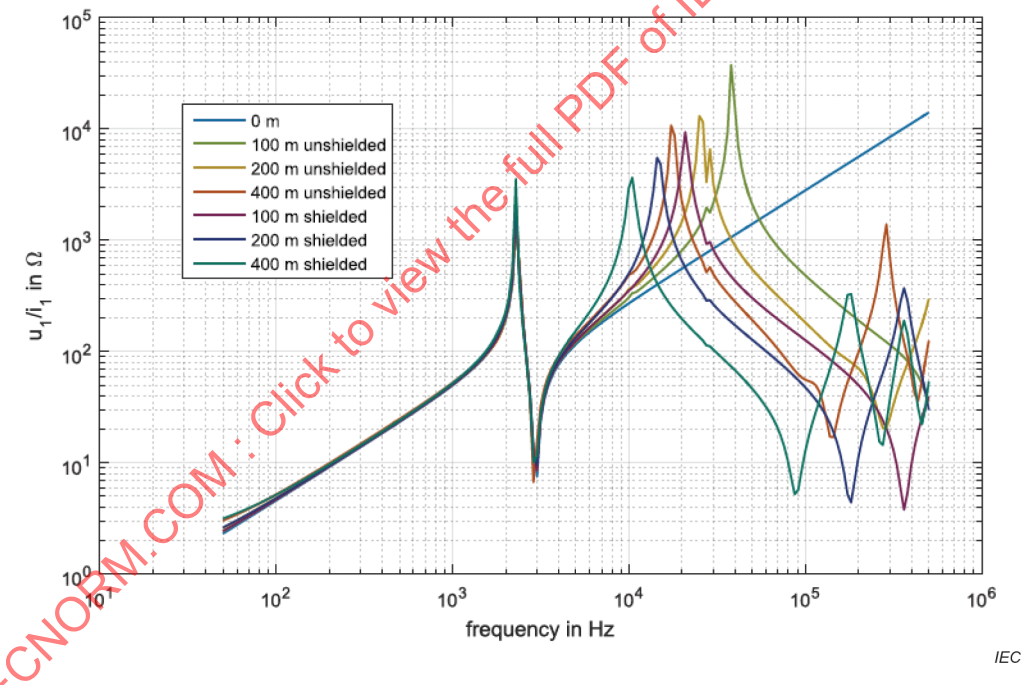

b) CM excitation

Figure 63 – Ratio of voltage and current in phase 1 with a third-order EMI filter and different cables with: a) DM excitation and b) CM excitation

6.4 Multiple EV chargers in a central charging infrastructure

6.4.1 General

This example case discusses the emission and interaction of multiple onboard chargers of battery electric vehicles (BEVs) of the same type regarding the supraharmonic voltage and current distortion. In general, the behaviour is representative for any other type of power converter based on self-commutating topology. Each device acts both as a source and a sink for supraharmonic emission.

6.4.2 Measurements

Measurements were taken in a central BEV fleet charging installation consisting of four charging stations (CSs) with two AC charging points (CPs) each. They are connected to a junction box, which is supplied from the LV busbar of the MV/LV supply transformer by a dedicated cable. The voltages and currents were measured at the four charging stations and the LV busbar (total current of the cable supplying the charging stations). In the experiment six BEVs of the same make have been connected step by step in the following sequence: BEV1 to CS1/CP1, BEV2 to CS2/CP1, BEV3 to CS3/CP1, BEV4 to CS4/CP1, BEV5 to CS1/CP2, and BEV 6 to CS2/CP2. Figure 64 shows the voltage around the dominant emission frequency of 10 kHz of these BEVs as emission bands (group band size B = 800 Hz) using 20 ms measurement windows along with the average RMS value (dotted line).

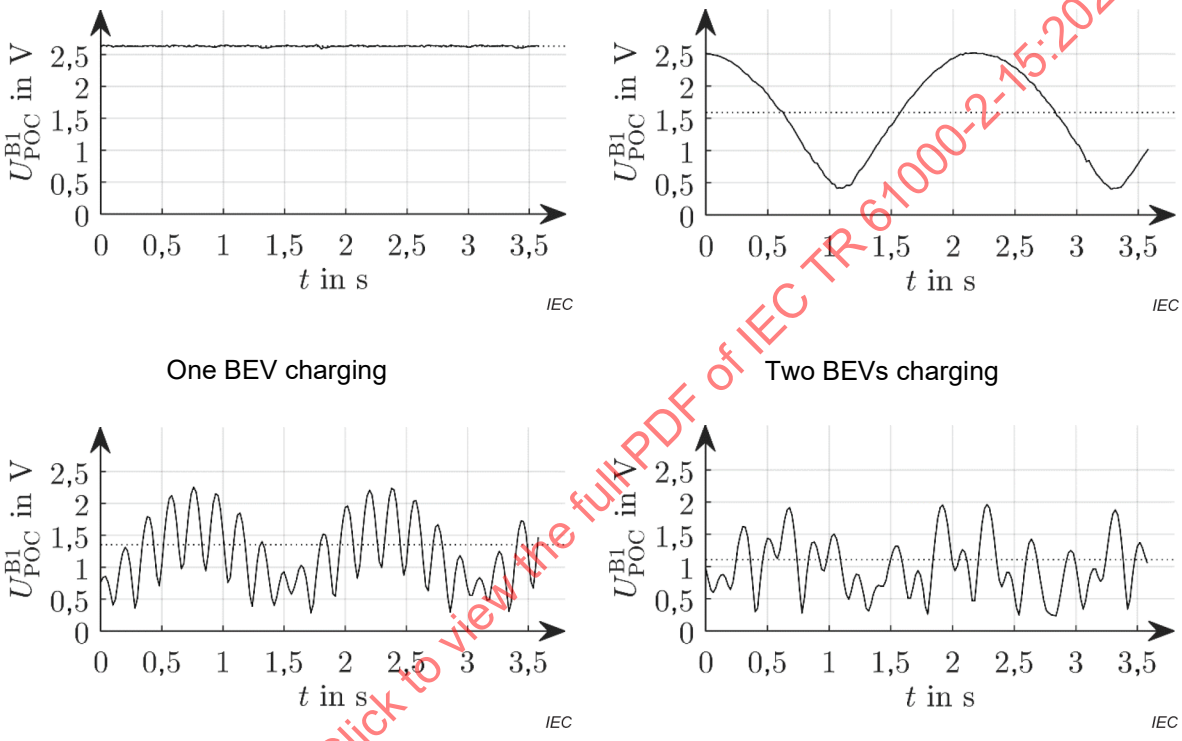

Figure 64 – Voltage at 10 kHz of one to four BEVs charging at a common POC, time varying values as solid line (20 ms measurement windows), overall RMS as dotted line

With a single emission source, the distortion at 10 kHz is constant. With more than one source significant beating of the supraharmonic voltage magnitude is observed, which results from the slightly different switching frequencies of the BEVs. With two sources, a clear periodicity of approximately 1,6 s exists, which indicates a difference in switching frequency between the two BEVs of 625 mHz. This is usually caused by manufacturing tolerances. With three sources, periods of 1,6 s and 0,1 s are visible. With four or more emission sources, the variation of voltage in the emission band becomes pseudo-random. The maximum of the magnitude based on 20 ms significantly deviates from the long-term RMS (e.g. 10 min value) in all cases except with a single source. Such higher supraharmonic voltages over short periods might cause malfunctions, which would not be indicated by the overall RMS value at all. Frequently, a chirping noise is reported in the presence of beating effects.

The magnitude of voltages and currents for up to six BEVs is shown in Figure 65. In Figure 65 a), the RMS voltage decreases monotonously with an increasing number of vehicles. For two and three BEVs, the maximum voltage due to the beating (see Figure 65) is approximately $\sqrt{N}$ times larger than the average RMS voltage, as also predicted in [26]. The minimum drops to very low values, but not the expected value of zero for two or more BEVs. Two aspects mainly cause the deviation from theoretical expectations. For higher numbers N, the frequency of occurrence of the overall maximum and overall minimum reduces significantly and is most likely not captured due to the limited charging time of the BEVs. Further, the emission magnitudes of the BEVs slightly deviate from each other.

In Figure 65 b), the individual RMS currents in the dominant emission band (10 kHz) of the first three charging stations and the total current of the charging infrastructure are shown for the stepwise connection of four BEVs. The RMS current in the cable is directly proportional to the RMS voltage and decreases monotonously. The current injected by the first BEV more than doubles when the second BEV is connected and the current flowing between the BEVs is much higher compared to the total current of the charging infrastructure flowing to the transformer. This results from the input impedance of the BEVs at 10 kHz, which is much lower than the network impedance at this frequency. For more than one BEV, the current injected by each source remains relatively constant with each additional source (plotted lines show average RMS current).

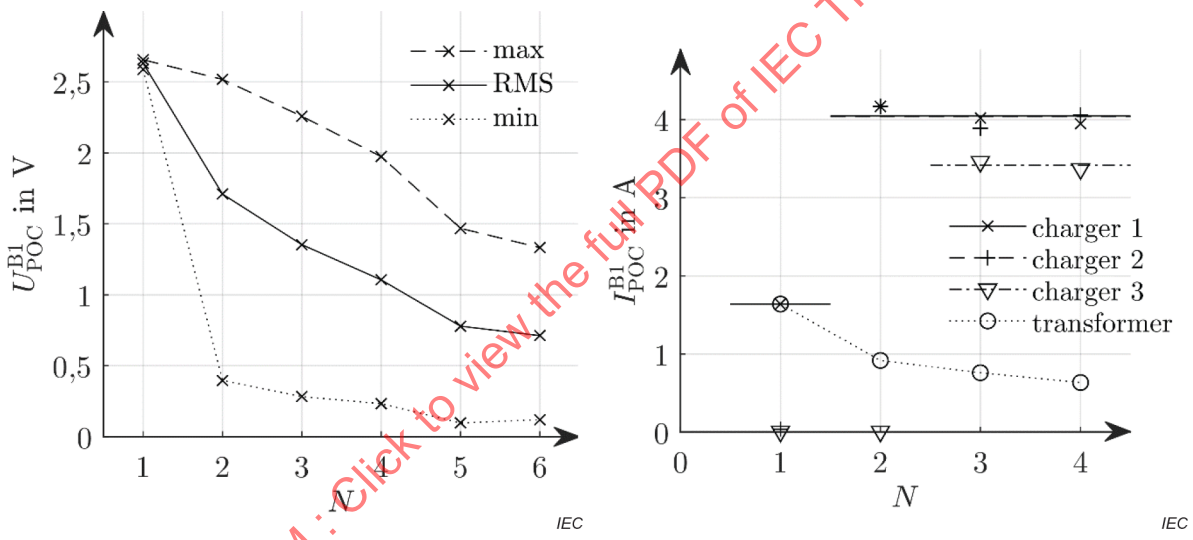

a) Supraharmonic voltage

b) Supraharmonic RMS current

Figure 65 – Supraharmonic voltages and currents at the POC of multiple AC charging points, first emission band (800 Hz) centred around 10 kHz

6.4.3 Modelling of interactions between N similar single-phase power converters

6.4.3.1 General

Figure 66 shows the single-line diagram for an arbitrary number N of similar converters (same make and model assumed). Since all converters have their own carrier signal generator, all supraharmonic emissions are asynchronous and each emission can be treated individually. The corresponding supraharmonic emission model based on a Thévenin equivalent is shown in Figure 67.

In general, an increasing number of power converters connected to a single POC will change the resulting supraharmonic voltages. Each additional power converter will contribute to the voltage distortion, but also act as a sink for the contributions of neighbouring power converters at the same time. Consequently, it depends on the ratio of the additional damping and contribution of an additional power converter, whether the total supraharmonic voltage at the POC decreases or increases.

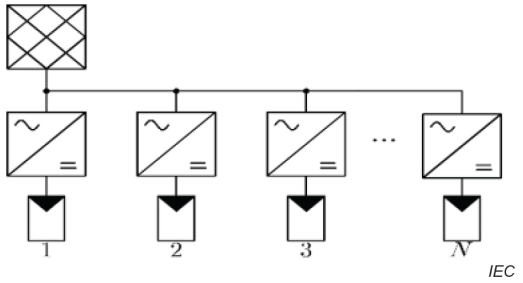

Figure 66 – Single-line diagram of an arbitrary number N of power converters operating in parallel on a single network phase

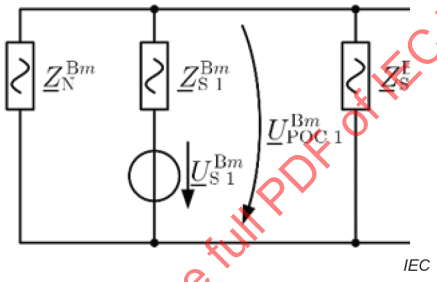

Figure 67 – Supraharmonic emission model for an arbitrary number N of power converters operating in parallel

6.4.3.2 Modelling of beating

According to [28] the supraharmonic voltage in an emission band m at the H-bridge of a single-phase self-commutated power converter can be expressed by an amplitude-modulated sinusoidal voltage, which can be represented by an amplitude-modulated rotating RMS voltage phasor:

$$\underline{U}_{\mathrm{AB}}^{\mathrm{B}m}(t) = a_{\mathrm{AB}}^{\mathrm{B}m}(t) \cdot U_{\mathrm{AB}}^{\mathrm{B}m} \cdot \exp\left(\mathrm{j}\omega_{\mathrm{AB}}^{\mathrm{B}m} t + \varphi_{\mathrm{AB}}^{\mathrm{B}m}\right) \tag{9}$$

Supraharmonic beating occurs, if the emission of multiple converters falls into the same emission band (frequency range). In this case, the asynchronous superposition of the emissions of the different converters will be considered. For simplification, the amplitude modulation of the voltage can be neglected here. Thus, each source n with emission in emission band m is characterized by an individual rotating RMS phasor:

$$\underline{U}_{\mathrm{S}\,n}^{\mathrm{B}m}(t) = U_{\mathrm{S}\,n}^{\mathrm{B}m} \cdot \exp\left(\mathrm{j}\Delta\omega_{\mathrm{S}\,n}^{\mathrm{B}m} t + \varphi_{\mathrm{S}\,n}^{\mathrm{B}m}\right) \tag{10}$$

where $U_{\mathrm{S}\,n}^{\mathrm{B}m}$ is the RMS source voltage, $\Delta\omega_{\mathrm{S}\,n}^{\mathrm{B}m}$ is the difference between the emission frequency and the centre frequency of the emission band and $\varphi_{\mathrm{S}\,n}^{\mathrm{B}m}$ is an arbitrary phase angle at $t = 0$. This source voltage is damped by the AC side filter of the converter to its contribution to the voltage at the POC in the considered emission band m.

$$\underline{U}_{\mathrm{POC}\,n}^{\mathrm{B}m}(t) = \underline{D}_{n}^{\mathrm{B}m} \cdot \underline{U}_{\mathrm{S}\,n}^{\mathrm{B}m}(t) \tag{11}$$

Here, $\underline{D}_{n}^{\mathrm{B}m}$ is the complex damping (and phase shift) factor, $\underline{U}_{\mathrm{S}\,n}^{\mathrm{B}m}(t)$ is the rotating phasor of the source voltage and $\underline{U}_{\mathrm{POC}\,n}^{\mathrm{B}m}(t)$ is the rotating phasor of the contribution of the n^{th} converter to the emission band voltage at the POC. The resulting (beating) voltage at time instant t is the absolute value of the sum of the rotating phasors of all contributing sources at this time instant:

$$U_{\mathrm{POC}}^{\mathrm{B}m}(t) = \left| \sum_{n=1}^{N} \underline{U}_{\mathrm{POC}\,n}^{\mathrm{B}m}(t) \right| \qquad n, N \in \mathbb{N} \tag{12}$$

For one up to three contributing sources with slightly different emission frequencies falling in the same emission band this is shown in Figure 68. The resulting shapes of the supraharmonic beating are qualitatively similar to the measured voltages in Figure 64.

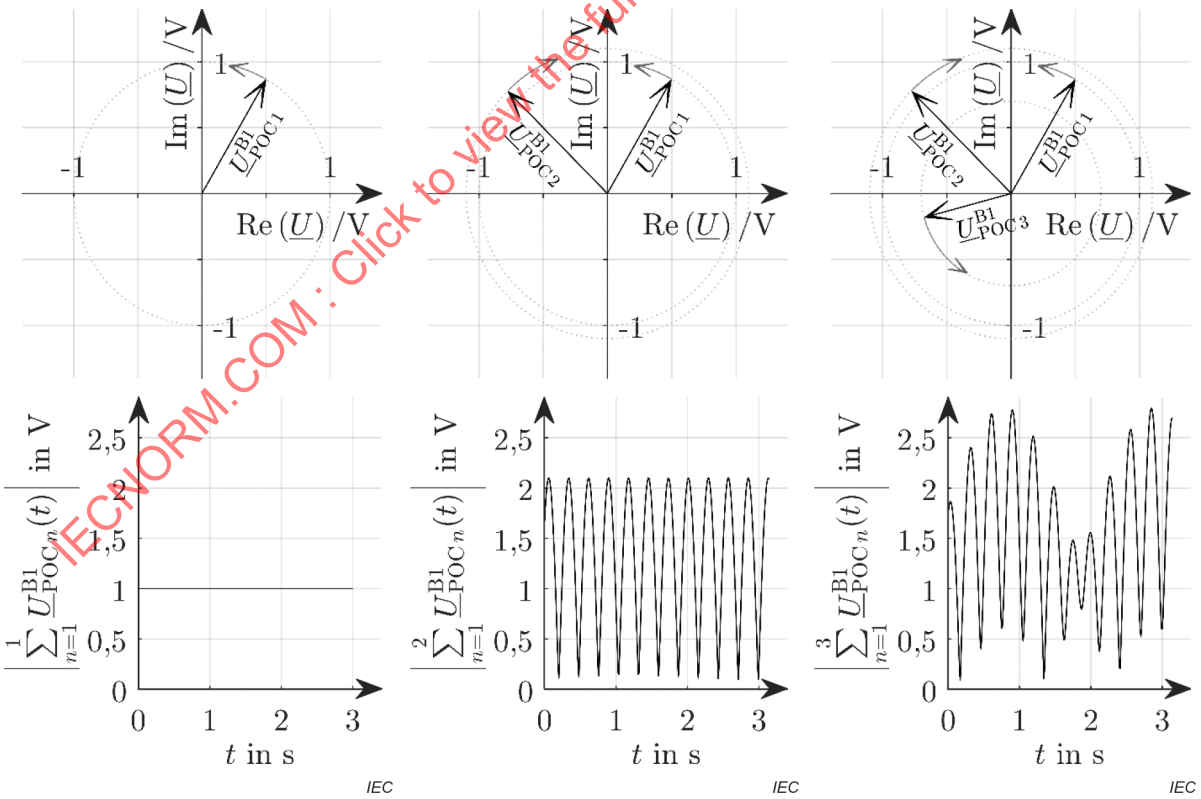

Figure 68 – Simulation of supraharmonic beating using summation of rotating phasors, for one up to three sources with different frequencies and magnitudes of contribution, first emission band

6.4.3.3 Modelling of summation

- General formula for N sources

  All sources are assumed to have identical source impedances $\underline{Z}_{\mathrm{S}\,n}^{\mathrm{B}m} = \underline{Z}_{\mathrm{S}}^{\mathrm{B}m}$ and source voltages $U_{\mathrm{S}\,n}^{\mathrm{B}m} = U_{\mathrm{S}}^{\mathrm{B}m}$. Using this assumption, the magnitude of the supraharmonic voltage at the POC of a single source n in an emission band can be simplified to

$$U_{\mathrm{POC}\,n}^{\mathrm{B}m} = U_{\mathrm{S}}^{\mathrm{B}m} \left| \frac{\dfrac{1}{\dfrac{1}{\underline{Z}_{\mathrm{N}}^{\mathrm{B}m}} + \sum_{n=2}^{N} \dfrac{1}{\underline{Z}_{\mathrm{S}}^{\mathrm{B}m}}}}{\underline{Z}_{\mathrm{S}}^{\mathrm{B}m} + \dfrac{1}{\dfrac{1}{\underline{Z}_{\mathrm{N}}^{\mathrm{B}m}} + \sum_{n=2}^{N} \dfrac{1}{\underline{Z}_{\mathrm{S}}^{\mathrm{B}m}}}} \right| = \frac{U_{\mathrm{S}}^{\mathrm{B}m}}{\left| \dfrac{\underline{Z}_{\mathrm{S}}^{\mathrm{B}m}}{\underline{Z}_{\mathrm{N}}^{\mathrm{B}m}} + N \right|}. \tag{13}$$

  As expected, the contribution of a single source n to the supraharmonic voltage at the POC depends on the total number of sources N. The (overall) RMS value of the superposition of N sources calculates as

$$U_{\mathrm{POC}}^{\mathrm{B}m}(N) = \sqrt{\sum_{n=1}^{N} U_{\mathrm{POC}\,n}^{\mathrm{B}m\,2}} = \frac{\sqrt{N} \cdot U_{\mathrm{S}}^{\mathrm{B}m}}{\left| \dfrac{\underline{Z}_{\mathrm{S}}^{\mathrm{B}m}}{\underline{Z}_{\mathrm{N}}^{\mathrm{B}m}} + N \right|}. \tag{14}$$

  As explained in 6.4.3.1 and 6.4.3.2, the operation of multiple supraharmonic sources in parallel causes a beating of the voltage with magnitudes deviating considerably from the overall RMS value (see Figure 64). The maximum of the beating occurs when all individual sources are in phase.

$$\hat{U}_{\mathrm{POC}}^{\mathrm{B}m}(N) = \sum_{n=1}^{N} U_{\mathrm{POC}\,n}^{\mathrm{B}m} = N \cdot U_{\mathrm{POC}\,n}^{\mathrm{B}m} = \sqrt{N} \cdot U_{\mathrm{POC}}^{\mathrm{B}m} = \frac{N \cdot U_{\mathrm{S}}^{\mathrm{B}m}}{\left| \dfrac{\underline{Z}_{\mathrm{S}}^{\mathrm{B}m}}{\underline{Z}_{\mathrm{N}}^{\mathrm{B}m}} + N \right|} \tag{15}$$

  This means that the maximum of the beating supraharmonic voltage can reach $\sqrt{N}$ times the size of the average RMS voltage in an emission band. It is noted that the calculation of the average RMS voltage based on measurements will include at least one full cycle of the "beating pattern" caused by the N sources.

- Maximum supraharmonic voltage

  Formula (14) has a single maximum for

$$N_{\max} = \left| \frac{\underline{Z}_{\mathrm{S}}^{\mathrm{B}m}}{\underline{Z}_{\mathrm{N}}^{\mathrm{B}m}} \right| \tag{16}$$

  contributing sources. At this number of sources $N = N_{\max}$ the overall RMS voltage in an emission band equals

$$U_{\mathrm{POC\,max}}^{\mathrm{B}m} = \frac{\sqrt{\left|\frac{\underline{Z}_{\mathrm{S}}^{\mathrm{B}m}}{\underline{Z}_{\mathrm{N}}^{\mathrm{B}m}}\right|}\cdot U_{\mathrm{S}}^{\mathrm{B}m}}{\left|\frac{\underline{Z}_{\mathrm{S}}^{\mathrm{B}m}}{\underline{Z}_{\mathrm{N}}^{\mathrm{B}m}}+\left|\frac{\underline{Z}_{\mathrm{S}}^{\mathrm{B}m}}{\underline{Z}_{\mathrm{N}}^{\mathrm{B}m}}\right|\right|} = \frac{1}{\left|\exp\left(\mathrm{j}\left[\angle\underline{Z}_{\mathrm{S}}^{\mathrm{B}m}-\angle\underline{Z}_{\mathrm{N}}^{\mathrm{B}m}\right]\right)+1\right|}\cdot\frac{1}{\sqrt{\left|\frac{\underline{Z}_{\mathrm{S}}^{\mathrm{B}m}}{\underline{Z}_{\mathrm{N}}^{\mathrm{B}m}}\right|}}\cdot U_{\mathrm{S}}^{\mathrm{B}m} \tag{17}$$

Applying the condition (16) to (15), the maximum voltage caused by the beating is calculated by

$$\hat{U}_{\mathrm{POC\,max}}^{\mathrm{B}m} = \sqrt{\left|\frac{\underline{Z}_{\mathrm{S}}^{\mathrm{B}m}}{\underline{Z}_{\mathrm{N}}^{\mathrm{B}m}}\right|}\cdot U_{\mathrm{POC\,max}}^{\mathrm{B}m} = \frac{1}{\left|\exp\left(\mathrm{j}\left[\angle\underline{Z}_{\mathrm{S}}^{\mathrm{B}m}-\angle\underline{Z}_{\mathrm{N}}^{\mathrm{B}m}\right]\right)+1\right|}\cdot U_{\mathrm{S}}^{\mathrm{B}m} \tag{18}$$

According to Formula (17) the resulting overall RMS voltage at the POC depends on three criteria:

1) the magnitude of the source voltage $U_{\mathrm{S}}^{\mathrm{B}m}$;

2) the ratio of the magnitudes of the impedances $\left|\frac{\underline{Z}_{\mathrm{S}}^{\mathrm{B}m}}{\underline{Z}_{\mathrm{N}}^{\mathrm{B}m}}\right|$;

3) the phase angle difference between the impedances $\underline{Z}_{\mathrm{S}}^{\mathrm{B}m}$ and $\underline{Z}_{\mathrm{N}}^{\mathrm{B}m}$.

If representative value ranges are available for the magnitude and phase angle of the network loop impedance $\underline{Z}_{\mathrm{N}}(f)$, these criteria allow manufacturers of power converters to design their devices so that the POC voltage does not exceed a given limit. Due to the degrees of freedom (source voltage and source impedance), a large variety of combinations exists, which would fulfill such a condition. A possible conservative approach is:

a) The magnitude of the source voltage does not exceed the given limit. $U_{\mathrm{S}}^{\mathrm{B}m} \le U_{\mathrm{limit}}^{\mathrm{B}m}$ (19)

b) The magnitude of the source impedance is higher than any known or reasonable magnitude of the network loop impedance. $\left|\underline{Z}_{\mathrm{S}}^{\mathrm{B}m}\right| \ge \left|\underline{Z}_{\mathrm{N}}^{\mathrm{B}m}\right|$ (20)

c) The phase angle of the source impedance is within ±120° of any known or reasonable network loop impedance (the phase angle of the LISN defined in IEC 61000-1-2 [69] or the prevailing phase angle based on comprehensive measurements might be a reasonable estimate). $-120° \le \left(\angle\underline{Z}_{\mathrm{S}}^{\mathrm{B}m} - \angle\underline{Z}_{\mathrm{N}}^{\mathrm{B}m}\right) \le +120°$ (21)

With regard to the maximum voltage due to the beating according to Formula (18) only the first and the third condition are relevant, which emphasize that during the design of the device particular care needs to be taken with regard to the phase angle of the source impedance and the magnitude of the source voltage.

The application of the phase angle criterion is shown as an example in Figure 69 for two photovoltaic inverters studied in [29]. Considering all measured network loop impedances from [19], [34], inverter A meets the criterion for all impedances, while inverter B does not for a majority of the measurements. In case the two other criteria would meet only the worst-case border conditions ($U_{\mathrm{S}}^{\mathrm{B}m} = U_{\mathrm{limit}}^{\mathrm{B}m}$ and $\left|\underline{Z}_{\mathrm{S}}^{\mathrm{B}m}\right| = \left|\underline{Z}_{\mathrm{N}}^{\mathrm{B}m}\right|$), the POC voltage would exceed the limit at certain locations.

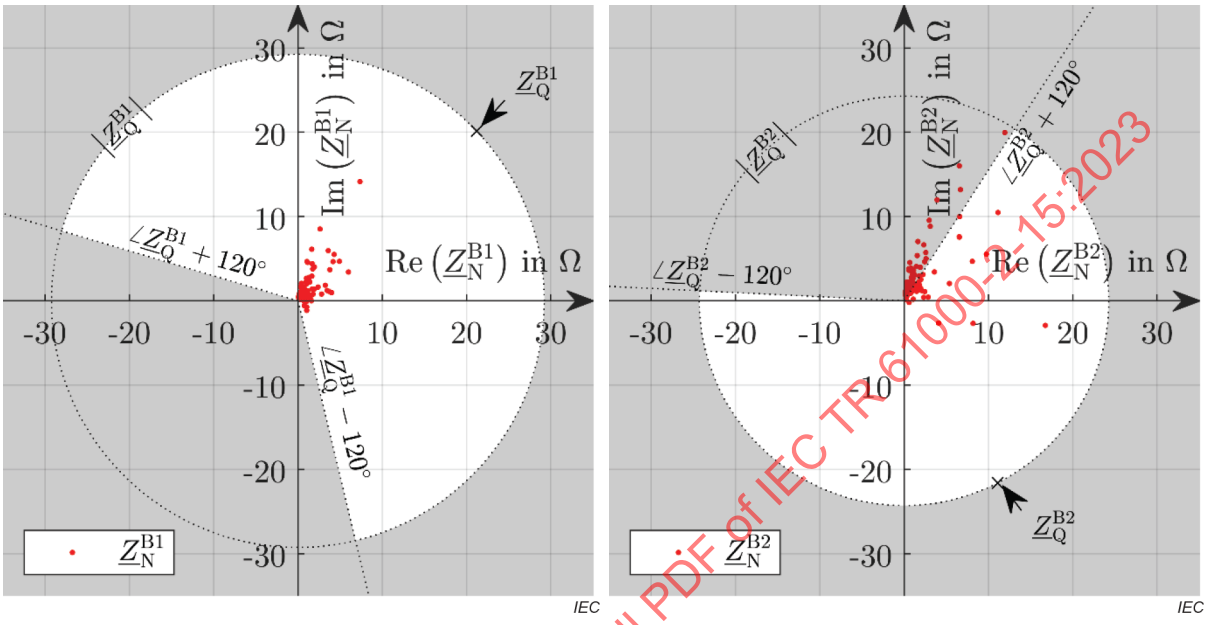

a) Inverter A, 1st emission band at 16 kHz **b) Inverter B, 2nd emission band at 36 kHz**

Red dots mark 187 measured network loop impedances from [41]; network loop impedances in the white area meet the criterion.

Figure 69 – Exemplary assessment of the supraharmonic emission of two photovoltaic inverters using the criteria in Formula (19) to Formula (21), and photovoltaic inverters from [15]

It can be desirable to estimate whether an increasing number of sources results always in a monotonous reduction of the supraharmonic voltage at the POC. As Formula (14) has only a single maximum, it is sufficient to show that the voltage with two sources is less than or equal to the voltage with a single source in order to achieve this behaviour.

$$U_{\mathrm{POC}}^{\mathrm{B}m}(N=1) \geq U_{\mathrm{POC}}^{\mathrm{B}m}(N=2) \tag{22}$$

$$\frac{\sqrt{1}\cdot U_{\mathrm{S}}^{\mathrm{B}m}}{\left|\frac{\underline{Z}_{\mathrm{S}}^{\mathrm{B}m}}{\underline{Z}_{\mathrm{N}}^{\mathrm{B}m}}+1\right|} \geq \frac{\sqrt{2}\cdot U_{\mathrm{S}}^{\mathrm{B}m}}{\left|\frac{\underline{Z}_{\mathrm{S}}^{\mathrm{B}m}}{\underline{Z}_{\mathrm{N}}^{\mathrm{B}m}}+2\right|} \tag{23}$$

This inequation is fulfilled if

$$\left|\underline{Z}_{\mathrm{S}}^{\mathrm{B}m}\right| \leq \sqrt{2}\cdot\left|\underline{Z}_{\mathrm{N}}^{\mathrm{B}m}\right|. \tag{24}$$

For all network loop impedances $\underline{Z}_{\mathrm{N}}^{\mathrm{B}m}$ which fulfill Formula (24), the supraharmonic voltage in an emission band will decrease with each additional (identical) source. However, minimizing the non-intentional supraharmonic voltages by lowering the source impedance might also have an adverse effect on intentional emission, such as unwanted high damping of mains communication system (MCS/PLC) signals. On the other hand, Formula (17) shows that the maximum overall RMS voltage at POC at $N = N_{\mathrm{max}}$ decreases with increasing source impedance (criterion 2), assuming the other two criteria remain unchanged. This dependency is illustrated as an example for different impedance magnitude ratios (equal impedance phase angles) in Figure 70.

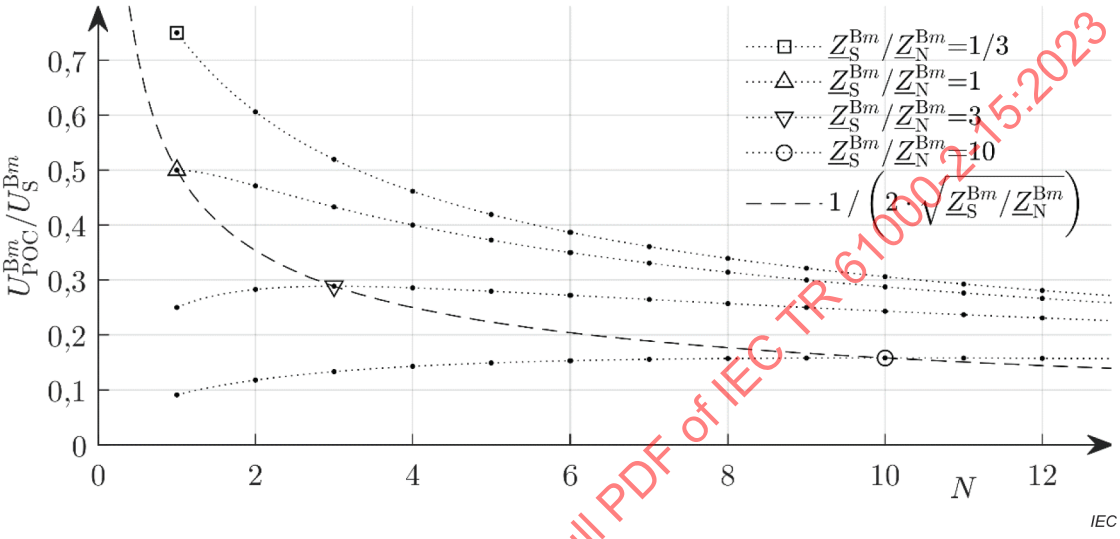

Figure 70 – Dependency of the POC voltage on the number of sources N for different magnitude ratios of source impedance to network impedance assuming phase angles of source impedance and network impedance are equal

Concluding the results of the above considerations,

– a source impedance magnitude higher than the network impedance at low source voltage magnitude, and

– a low phase angle difference between the source impedance and the network (loop) impedance

provide the most “grid-friendly” supraharmonic source behaviour. The results can serve as guidance to manufacturers, installation planners and network operators to manage supraharmonic disturbance levels in LV networks efficiently and to share the risks and costs for ensuring EMC fairly between the stakeholders.

All descriptions and derivations apply primarily to single-phase power converters connected to the same phase. In three-phase systems, it is likely that multiple similar converters are distributed to the three phases. In this case, the converter in one phase will contribute to some extent to the supraharmonic voltages at the POC in another phase. The coupling between the phases depends on several factors but is usually low. Therefore, the results are also a valid estimate for single-phase converters connected to different phases in three-phase networks, as long as each phase is considered individually.

7 Impact of grid conditions on the operation of converters

7.1 Analysis of a single-phase inverter model with an LCL filter using the Nyquist criterion

Clause 7 presents an application example of the Nyquist stability criterion for the assessment of the stability of a current controller in accordance with [30], [36]. The analysis of a simple active infeed converter demonstrates the impact of the grid line impedance on the stability of the converter controller. Figure 71 shows an inverter connected to the AC grid trough an LCL-filter. The system can be split into three parts from left to right: the grid with its impedance, the LCL filter, and a full-bridge inverter with its DC bus. State variables for the LCL filter are also represented in Figure 71:

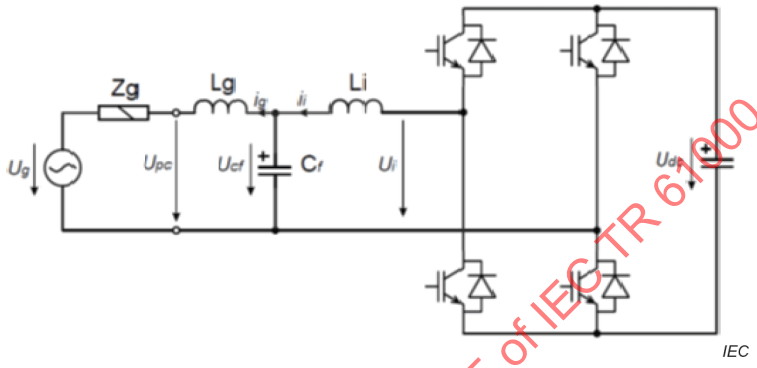

Figure 71 – Single phase inverter with an LCL filter and corresponding state variables

The state variables of the system are described as follows:

$$\begin{cases} \dot{u}_{cf} = \dfrac{1}{C_f}.\left(i_i - i_g\right) \\ \dot{i}_i = \dfrac{1}{L_i}.\left(u_i - u_{cf}\right) \\ \dot{i}_g = -\dfrac{1}{L_g}.\left(u_{pc} - u_{cf}\right) \end{cases} \tag{25}$$

The formulae in (25) and corresponding impedances in the Laplace domain are represented in the form of a block scheme on Figure 72:

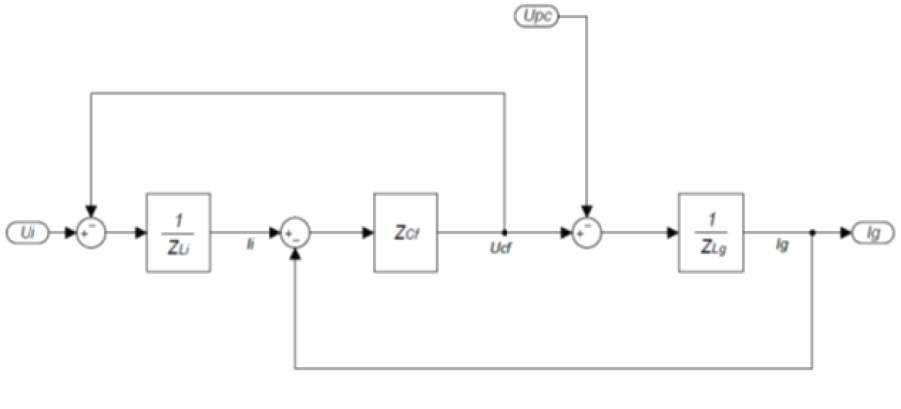

Figure 72 – Block scheme equivalent to the formula system of Figure 71

The impedances are described as follows:

$$Z_{L_i} = L_i \cdot s$$

$$Z_{L_g} = L_g \cdot s \tag{26}$$

$$Z_{L_i} = \frac{1}{C_f \cdot s}$$

The following relations can be established on the basis of Figure 71 and Figure 72:

$$I_g(s) = \frac{Z_{C_f}}{Z_{C_f} + Z_{L_g}} \cdot i_i(s) - \frac{1}{Z_{C_f} + Z_{L_g}} \cdot u_{pc}(s) \tag{27}$$

$$U_i(s) = \frac{Z_{C_f} Z_{L_g} + Z_{C_f} Z_{L_i} + Z_{L_g} Z_{L_i}}{Z_{C_f} + Z_{L_g}} \cdot i_i(s) + \frac{Z_{C_f}}{Z_{C_f} + Z_{L_g}} \cdot u_{pc}(s) \tag{28}$$

The linearized control loop for the injected current is shown in Figure 73. The current controller is represented by $G_{\mathrm{Ci}}(s)$. The block F_{feed} corresponds to the feed-forward of the point of connection voltage. The function F_{curr} corresponds to a filter for the injected current measurement. The corresponding transfer functions for blocks F_{feed} and F_{curr} are represented in Figure 73. The non-linear PWM modulator has been replaced by a transfer function with a constant gain U_{dc}. This linearization makes the model valid only at frequencies much lower than the switching frequency of the converter.

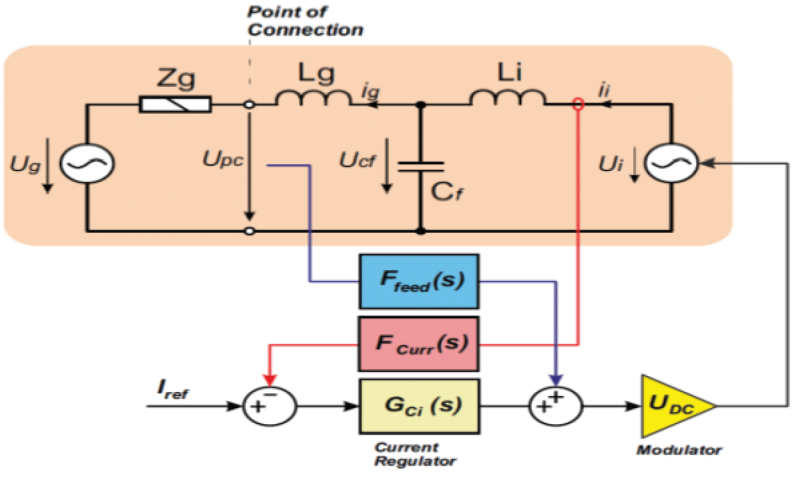

Figure 73 – Linearized control loop for the in-feed converter and transfer functions for feed forward and current measurement filter

The transfer blocks are expressed as follows:

$$F_{\text{feed}} = \frac{K_{\text{feed}}}{\frac{s}{2\pi f_{\text{cu}}} + 1} \tag{29}$$

$$F_{\text{curr}} = \frac{K_{\text{curr}}}{\frac{s}{2\pi f_{ci}} + 1} \tag{30}$$

From the perspective of the controller, the voltage generated by the inverter U_{i} can be described by Formula (31), where I_{ref} is the current reference, G_{Ci} the current regulator and U_{DC} is the bus voltage.

$$U_i(s) = \left[\left(I_{\text{ref}}(s) - I_i(s) \cdot F_{\text{curr}}(s)\right) \cdot G_{C_i}(s) + u_{pc}(s) \cdot F_{\text{feed}}(s)\right] \cdot U_{DC} \tag{31}$$

Formula (31) equalized with Formula (28) results in Formula (32):

$$\left[\left(I_{\text{ref}}(s) - I_i(s) \cdot F_{\text{curr}}(s)\right) \cdot G_{C_i}(s) + u_{pc}(s) \cdot F_{\text{feed}}(s)\right] \cdot U_{DC} = \frac{Z_{C_f} Z_{L_g} + Z_{C_f} Z_{L_i} + Z_{L_g} Z_{L_i}}{Z_{C_f} + Z_{L_g}} \cdot i_i(s) + \frac{Z_{C_f}}{Z_{C_f} + Z_{L_g}} \cdot u_{pc}(s) \tag{32}$$

The inverter current I_i is described in Formula (33) as a function of U_{pc} and I_{ref}:

$$I_i = \frac{U_{dc} \cdot \left(G_{C_i} I_{ref} + F_{feed} U_{pc}\right)\left(Z_{C_f} + Z_{L_g}\right) - U_{pc} Z_{C_f}}{Z_{C_f} Z_{L_g} + Z_{C_f} Z_{L_i} + Z_{L_g} Z_{L_i} + F_{curr} G_{C_i} U_{dc} \cdot \left(Z_{C_f} + Z_{L_g}\right)} \tag{33}$$

Formula (34) is obtained by replacing I_i in Formula (27) with I_i out of Formula (33). The Norton equivalent circuit for the whole converter and its controller obtained from Formula (34) is represented in Figure 74.

$$I_g = \frac{G_{C_i} U_{dc} Z_{C_f}}{Z_{C_f} Z_{L_g} + Z_{C_f} Z_{L_i} + Z_{L_g} Z_{L_i} + F_{curr} G_{C_i} U_{dc} Z_{C_f} + F_{curr} G_{C_i} U_{dc} Z_{L_g}} \cdot I_{ref}$$

$$- - \frac{Z_{C_f} + Z_{L_g} + F_{curr} G_{C_i} U_{dc} - F_{feed} U_{dc} Z_{C_f}}{Z_{C_f} Z_{L_g} + Z_{C_f} Z_{L_i} + Z_{L_g} Z_{L_i} + F_{curr} G_{C_i} U_{dc} Z_{C_f} + F_{curr} G_{C_i} U_{dc} Z_{L_g}} \cdot U_{pc}$$

where:

$$G_{C_i} U_{dc} Z_{C_f} = G_{Norton} \tag{34}$$

$$\frac{Z_{C_f} Z_{L_g} + Z_{C_f} Z_{L_i} + Z_{L_g} Z_{L_i} + F_{curr} G_{C_i} U_{dc} Z_{C_f} + F_{curr} G_{C_i} U_{dc} Z_{L_g}}{G_{C_i} U_{dc} Z_{C_f}} \cdot I_{ref} = I_{conv}$$

$$\frac{Z_{C_f} + Z_{L_g} + F_{curr} G_{C_i} U_{dc} - F_{feed} U_{dc} Z_{C_f}}{Z_{C_f} Z_{L_g} + Z_{C_f} Z_{L_i} + Z_{L_g} Z_{L_i} + F_{curr} G_{C_i} U_{dc} Z_{C_f} + F_{curr} G_{C_i} U_{dc} Z_{L_g}} = Y_{conv}$$

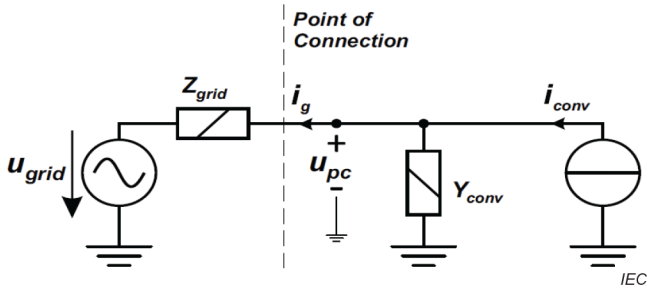

Figure 74 – Norton equivalent circuit of the single-phase inverter

Formula (34) can be represented in a simplified manner by Formula (35) and Formula (36) respectively:

$$i_g = i_{conv} \cdot \frac{\frac{1}{Y_{conv}}}{Z_{grid} + \frac{1}{Y_{conv}}} - \frac{u_{grid}}{Z_{grid} + \frac{1}{Y_{conv}}} \quad (35)$$

$$i_g = \left(i_{conv} - u_{grid} \cdot Y_{conv}\right) \cdot \frac{1}{1 + Z_{grid} Y_{conv}} \quad (36)$$

As explained in 7.1 a current-source system is stable if:

1) the current source itself is stable when unloaded, i.e., when the load is a short-circuit;
2) the load is stable when supplied by an ideal current source;
3) the ratio of the source output admittance to the load input admittance satisfies the Nyquist criterion.

By assuming that i_{conv} and the product $u_{grid} \cdot Y_{conv}$ in Formula (36) are stable, the stability analysis focuses on the ratio:

$$\frac{1}{1 + Z_{grid} \cdot Y_{conv}} \quad (37)$$

The Nyquist plot in Figure 75 shows that a control loop with a unity open loop and a feedback gain of $Z_{grid} \cdot Y_{conv}$ as represented in Formula (36) will not satisfy to the Nyquist stability criterion when the line inductance becomes equal to or larger than 2 mH. For this example, the system components and parameter values are listed in Table 8.

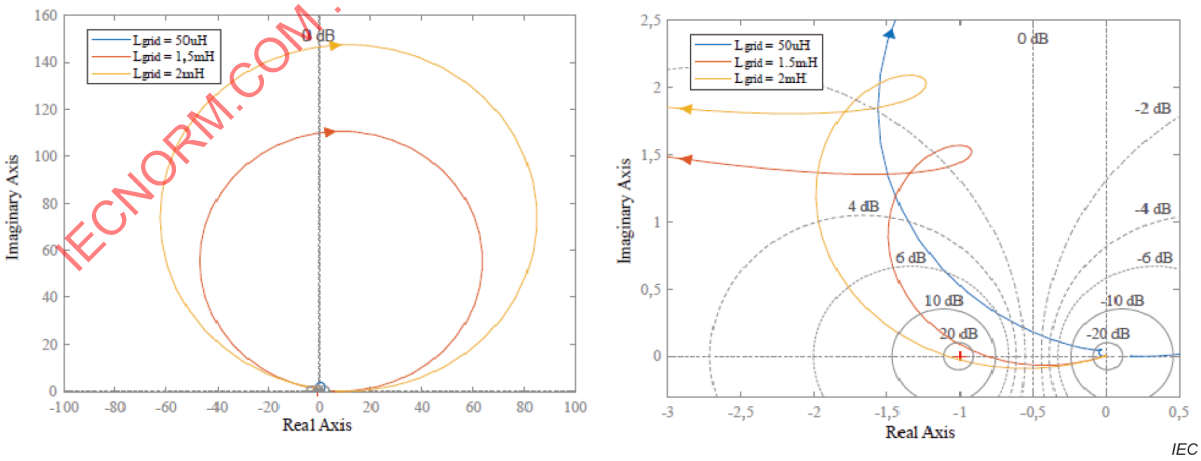

Figure 75 – Nyquist stability analysis of the control loop with parameters listed in Table 8

Table 8 – Example of system parameters and components for the Nyquist stability analysis

System parameter	Symbol	Value	Units	Component	Symbol	Value	Units
Grid voltage	U_{grid}	230	Vrms	Inductance inverter side	L_i	2,2	mH
Grid frequency	F_{grid}	50	Hz	Inductance grid side	L_g	300	uH
Switching frequency	F_{sw}	20	kHz	LCL filter capacitance	C_f	5	uF
DC bus voltage	U_{dc}	450	V	Current measure gain	K_{curr}	1	
Controller prop. coeff.	K_p	0,03		Current meas. bandwidth	F_{curr}	100	kHz
Contr. integral coeff	K_i	500		Voltage feedforward gain	K_{feed}	1/450	
				Voltage Feedf. badwidth	F_{feed}	1	kHz

For verification purposes, the same inverter and controller topologies were implemented in PLECS software as represented in Figure 76 and Figure 77, respectively:

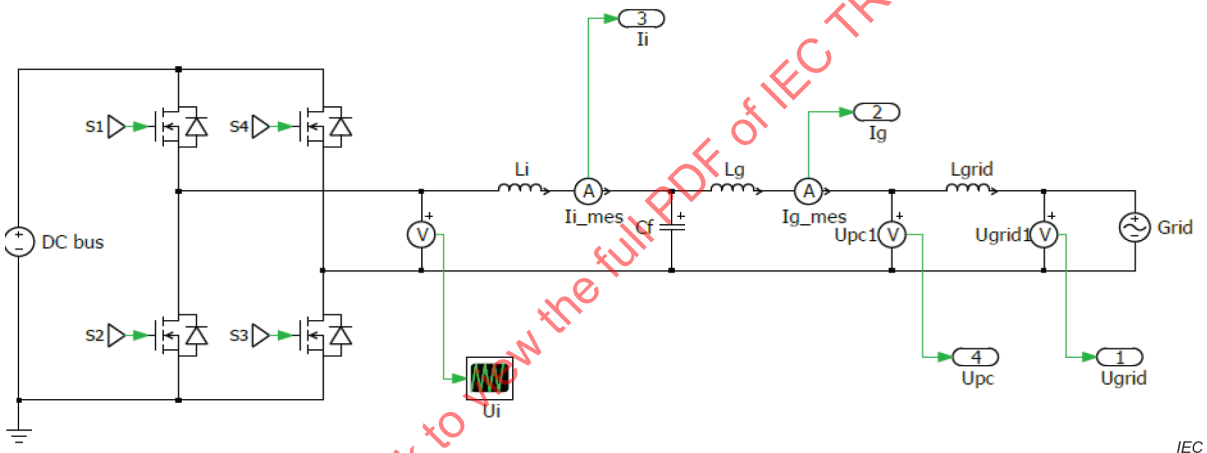

Figure 76 – PLECS model of the single-phase inverter with LCL filter

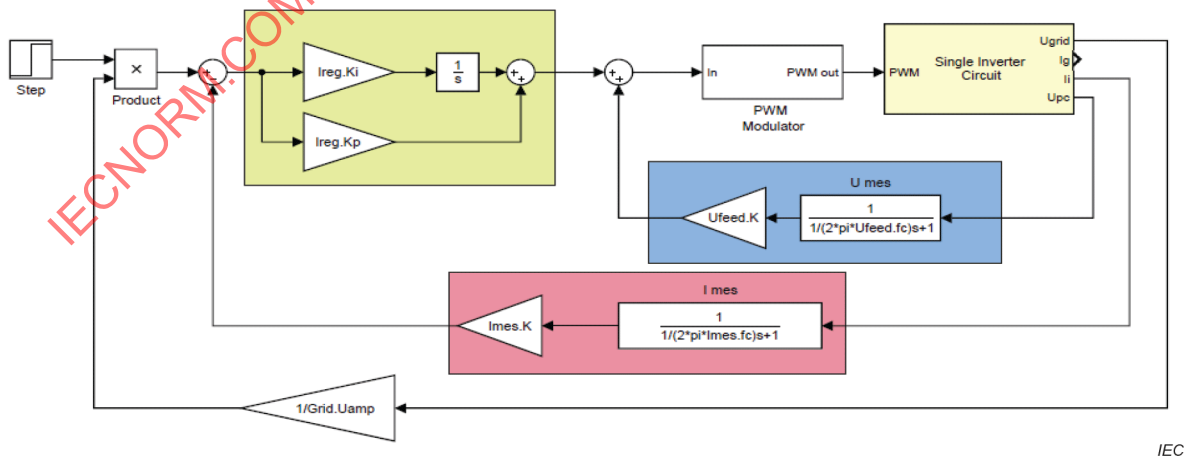

Figure 77 – PLECS model of the single-phase inverter controller with Feedforward of the connecting point voltage

The simulation results with a current reference step from 0 A to 10 A applied to the converter with the components and values listed in Table 8 are presented in Figure 78. The results show that the system becomes instable for a grid impedance L_{grid} larger than a value located between 1,5 mH and 2 mH.

Other controller parameters or topologies would maintain the stability of the system with even larger values of grid impedance. The feed forward plays a negative role in the converter stability in this particular case. But the example demonstrates both the effectiveness of the Nyquist criterion method and the impact of grid impedance on converter controller stability.

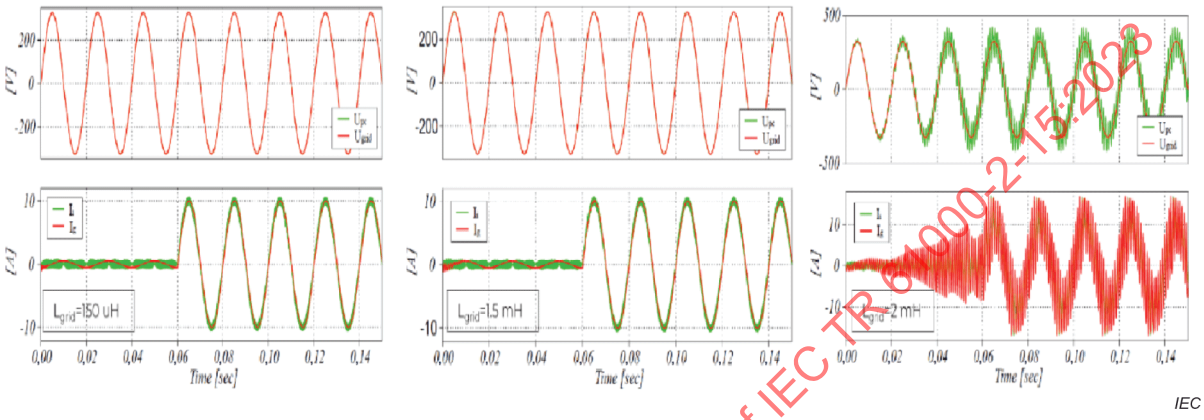

Figure 78 – Simulation result of a current reference step of 0 A to 10 A for the converter

Renewable energy generators are typically connected to the power grid via power electronic (PE) devices, specifically inverters (DC-AC power conversion). A current that is injected into the power grid by these inverters causes an interaction at the point of connection (PoC), which leads to a voltage drop over a network impedance Z_g. As a result, the voltage at the PoC becomes distorted and will in its turn affect the control of the inverter and the injected current.

For modelling and analysis purposes, the small signal characteristic of the linearized inverter behaviour at a frequency f can be represented in terms of an admittance Y_{Inv} and a current source.

Modelling and simulation as described above require detailed knowledge about the device, which is not always available, especially in case of commercial mass-market devices for use in low voltage networks. Alternatively, black-box identification methods can be used to identify the admittance characteristic of the device by performing specific measurements at the AC-side terminals of the device. At first a reference voltage $\underline{U}_{ACref}(f_U)$, for example a sinusoidal voltage at fundamental frequency (50 Hz or 60 Hz) is applied, which results in a current response $\underline{I}_{ACref}(f_I)$. Next a single-frequent voltage distortion component $\underline{U}_{ACi}(f_U)$ is swept over the considered frequency range, which results in respective current responses $\underline{I}_{ACi}(f_I)$ [55]. This way, for a particular operating point of the device, i.e. a particular power level of a single-phase inverter, the admittance characteristic of a device for each measuring point i, which represents the dependency between voltage and current at a particular frequency $(f_U = f_i)$, is obtained in terms of

$$\underline{Y}_{conv}(f_U, f_I) = \frac{\underline{I}_{ACi}(f_I) - \underline{I}_{ACref}(f_I)}{\underline{U}_{ACi}(f_U) - \underline{U}_{ACref}(f_U)} \quad (38)$$

With this method, so-called frequency coupling components (dependencies between voltage and current at different frequencies), which result from the time periodic characteristic of the device compared to the time invariant characteristic, can also be identified. In case only the admittance characteristic is of interest, a fast approach has been developed recently [56]. Based on the measured admittance characteristic, the harmonic stability of a device can now be assessed without knowing the internal parameters.

To illustrate the example of a measurement-based stability assessment, the admittance characteristic obtained for a commercially available single-phase inverter is depicted as an example in Figure 79.

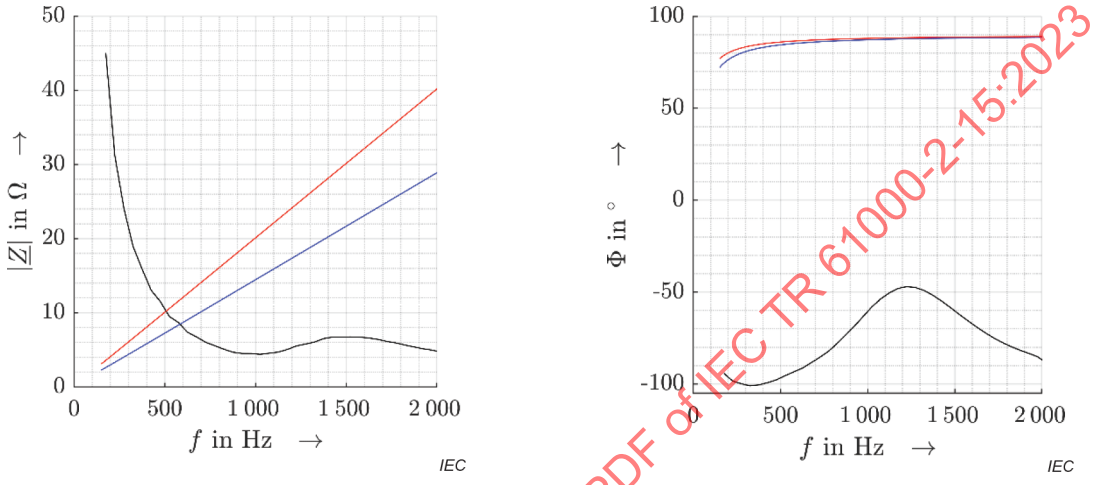

Figure 79 – Impedance magnitude (a) and phase angle characteristic (b) of commercially available single-phase inverter (black), network impedance with inductance of 2,3 mH (blue) and 3,2 mH (red)

By applying the Nyquist stability criterion as described above, the phase margin criterion and the amplitude criterion can be applied in order to determine possible grid impedances, which can result in an instable behaviour. For the studied inverter this is predicted for any R-L-equivalent as a network impedance with an inductance value of 3,2 mH. For a smaller inductance value, for example 2,3 mH, the formal analysis predicts a stable operation of the inverter. Figure 80 depicts the results, which confirms the prediction. While the inverter behaves stably at 2,3 mH, it trips after a few cycles while using 3,2 mH as grid inductance. Further details on the study can be found in [57].

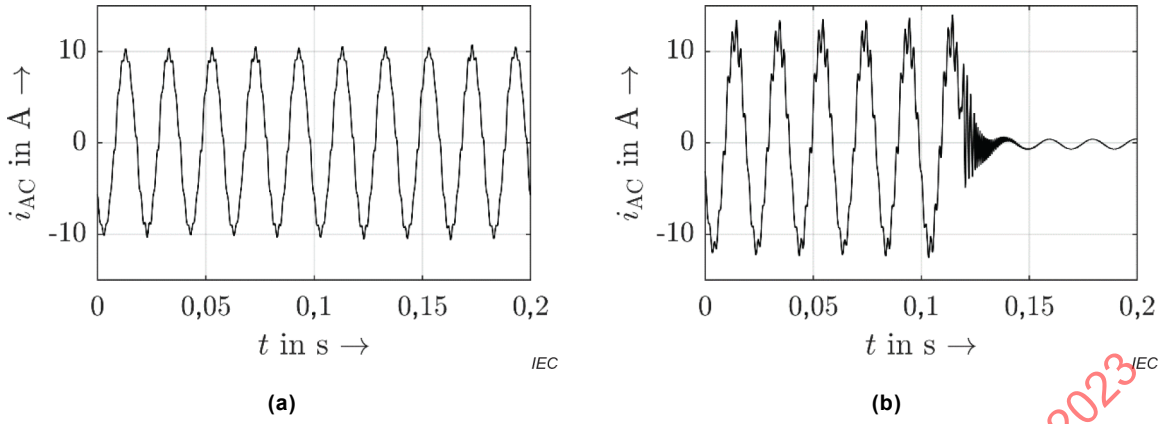

Figure 80 – Grid-side current measurements for *LR*-equivalent network impedance with inductance values of 2,3 mH (a) and 3,2 mH (b)

It can be noted that frequency-coupling components can also impact the device stability, which would be in particular considered for networks, where dominant frequency coupling components are expected.

7.2 Probabilistic stability analysis for commercial low power inverters based on measured grid impedances

This representation is typically used for grid-following inverters, as usually found in low power applications in low voltage (LV) networks (see Figure 81):

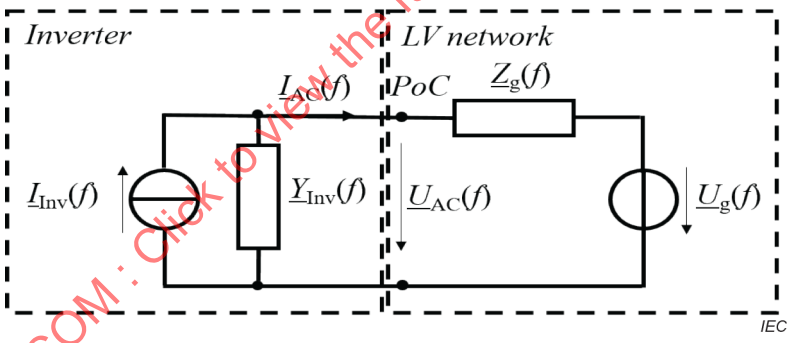

Figure 81 – Small signal model of an inverter and the low voltage network

The grid impedance and the device impedance that includes the linearized control and switching behaviour as well as further device components, for example the grid-side filter circuit, define the interaction of the inverter with the power grid and can be used to analyze the inverter stability. An instable operation of the inverter that is caused by the interaction between the control and the network impedance is often called a harmonic instability. The inverter can be studied with regard to harmonic instabilities in terms of the impedance-based stability criterion [30]. The system is considered stable, if the system provides a positive phase margin for the phase angle of the network impedance Φ_g and the phase angle of the inverter impedance Φ_{Inv} in terms of

$$180 - \Phi_g + \Phi_{Inv} > 0 \tag{39}$$

at the intersection of the magnitudes of the frequency dependent grid impedance (FdGI) and the inverter impedance. The challenge for the stability analysis is the large diversity of inverters with individual, impedance characteristics usually not disclosed by manufacturers, but also the significantly varying and often unknown LV grid impedance characteristics. The inverter impedance characteristic can be measured in the laboratory, for example by applying the method described in [31]. It can be noted that for one individual inverter the input impedance characteristics can also change with the operating point, for example DC power level. The impedance characteristics of LV networks can also be measured. The measurement campaign performed in central Europe, i.e. Germany, Switzerland, Austria and the Czech Republic [31] shows that the impedance characteristics of LV networks exhibit variations in the range of 2 decades and contain more or less pronounced resonances spread over a large frequency range. Due to the large variations both for the inverter-side impedance characteristics and the grid-side impedance characteristics, a probabilistic approach seems suitable for harmonic stability assessment.

The probabilistic approach is illustrated using network impedances measured at 120 different sites (see Figure 82) [32]. Furthermore, the input impedance characteristics of six commercially available inverters are measured in the laboratory (see Figure 83).

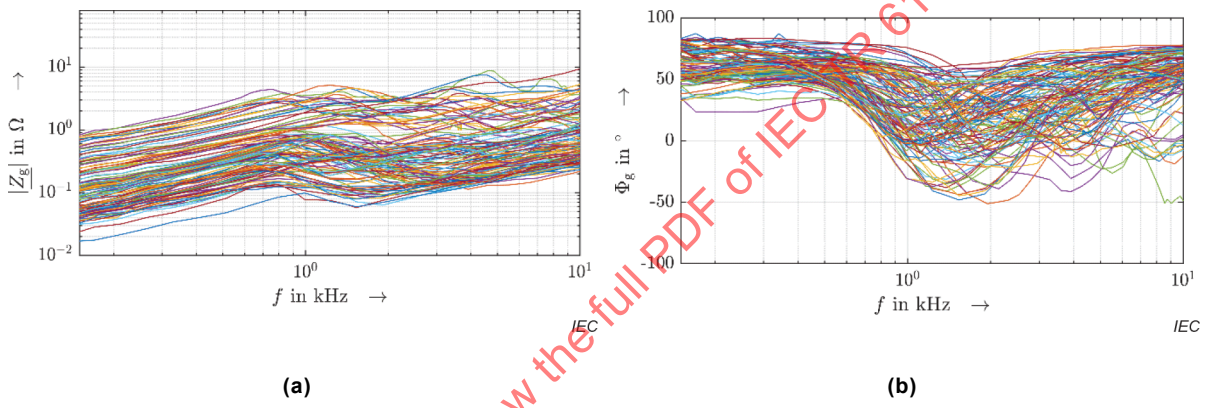

Figure 82 – Magnitude (a) and phase angle of low voltage network impedance measurements at 120 measurement sites

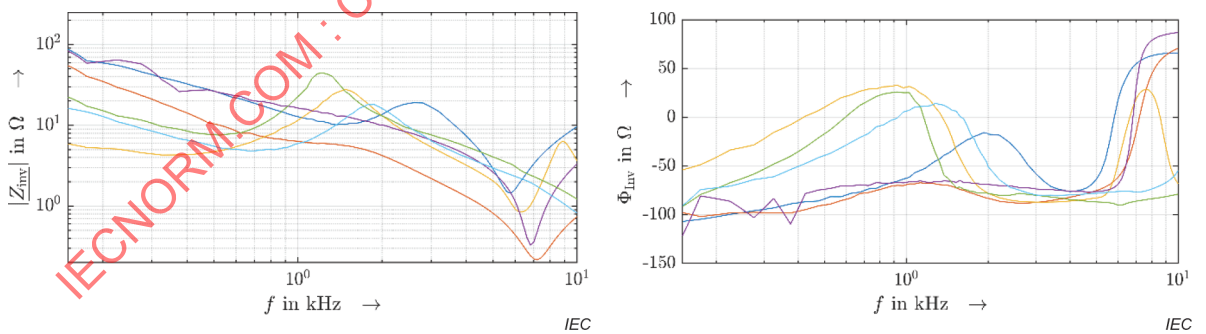

Figure 83 – Magnitude (a) and phase angle of the impedance of six commercially available inverters

Next, the impedance-based stability criterion is applied to all combinations of inverter impedances and grid impedances in order to detect those measurement sites that are expected to be critical for a stable inverter operation.

In order to include a certain stability margin, the minimum required phase margin is defined as 30°. To quantify the performance of a specific inverter regarding its probability to become instable, a grid-compatibility index gci is introduced that relates for an individual inverter the number of critical measurement sites n_c to the entire set of measurement sites n_{tot}:

$$\text{gci} = 1 - \frac{n_c}{n_{tot}} \tag{40}$$

Table 9 presents the grid-compatibility index for all six evaluated inverters. In accordance with other studies, Inverter 1 is the most reliable.

Table 9 – Grid-compatibility index of commercially available single-phase inverters

N° of inverters	1	2	3	4	5	6
Grid-compatibility index gci	1	0,966 9	0,958 7	0,966 9	0,925 6	0,983 5

With regard to the critical measurement sites, the frequency regions that indicate an instable inverter operation can be plotted with regard to the inverters and with regard to the measurement sites (see Figure 84). As an example, the critical frequency regions have been plotted up to 10 kHz, while for the gci, frequencies up to 39 kHz have been analyzed. Typically, not the entire frequency range is problematic, but only specific frequency regions challenge the stable inverter operation. Manufacturers can use this information to adapt their inverter designs to improve the device stability, for example by using the gci as an optimization criterion.

Further details on this study can be found in [33], [50].

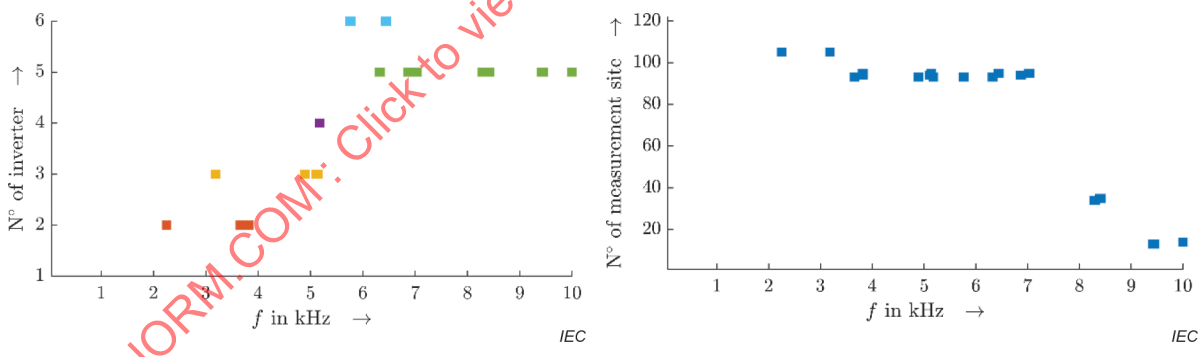

(a) (b)

Figure 84 – Critical frequency regions of commercially available inverters (a) and measurement sites in LV networks (b)

7.3 Description of electric vehicles connected to a weak network

7.3.1 General

- General

  The continuity of operation of charging stations, located within industrial or commercial sites, but also used on domestic installations, sometimes connected directly to public distribution grids, is an important matter in terms of quality and image of e-mobility services offered. The aim is to carry out the charging service without interruption of the charging process, or damage of the charging installation equipment that could be caused by possible instability phenomena appearing during the routine operation of the LV installation at the charging site.

  At the AC input of an EV charging station connected to an installation, and in relevant cases to the LV public distribution grid, the voltage wave can exhibit some distortion, especially if the impedance seen from the upstream supplying network has a high value. The voltage appearing can be much higher than the nominal voltage, up to twice this value, with an important distortion of the rated power sine waveform. This is reported in [33], and more recently in [39], where a strange behaviour is reported.

  The case where several electric vehicles are connected is generally more severe, as described also in [34] and [39].

- Types of network

  The general case involving electric vehicles is described in Figure 85:

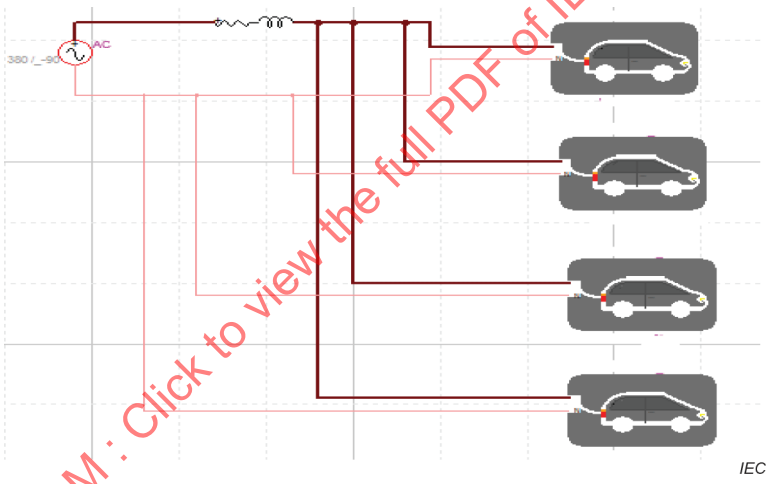

Figure 85 – Electrical network including the network and four electrical vehicles connected (described in the EMTP program)

  In [33], the case of a weak network is described with a 3 kW electric vehicle connected to it. Instabilities were encountered, with the charging operating correctly, suddenly stopping, then restarting again. This pattern has been observed as repeating several times.

  A feedback from Norway, owner of one of the largest fleet of electric vehicles in Europe, is described in [39],[40] with different entities concerned, with mention that a strange behaviour could appear in some cases.

7.3.2 Modeling of the equipment involved

As the interactions between the electrical network and the equipment are at stake ([32] to [34]), considering the non-linear behaviour involved, a proper equilibrium on the modeling aspects has to be found between the upstream network on one side and the charger on the other side with its filter and other components (see Figure 86):

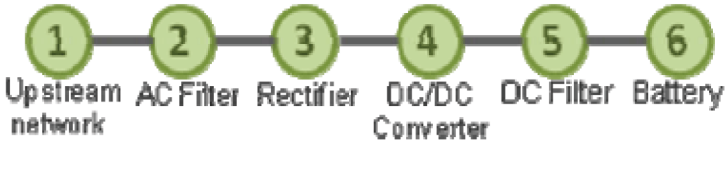

Figure 86 – Description of the different elements considered

Not all the components need to be modeled in detail, only the main ones, enabling a proper representation of the low frequencies' phenomena involved. In that case, the following elements have been represented, that is, the upstream network, the low-pass filter, the boost including its inductance, the power electronics and its capacitance, and the 3 kW battery, from the information derived from the network characteristics and also provided by the manufacturer on the charger itself.

The EMI (electromagnetic interference) filter prior to the boost is built to prevent the main harmonics generated by the power electronics as well as high frequency surges, such as switching or lightning surges, which can enter into the charger. It is made of two cells as described by Figure 87:

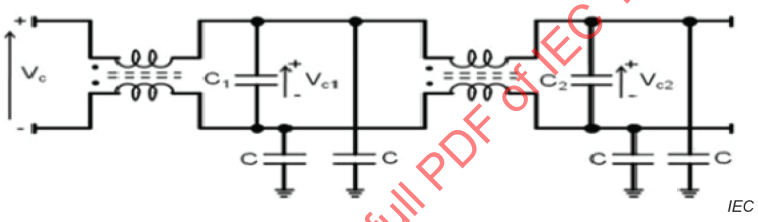

Figure 87 – Description of the filter connecting the boost to the electrical network

Figure 88 describes the modeling of the low frequency filter:

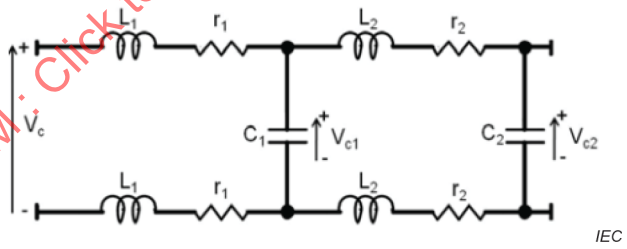

Figure 88 – Description of the low frequency filter

Figure 89 [33] shows the AC/DC rectifier of the charger mainly constituted by a PFC boost converter:

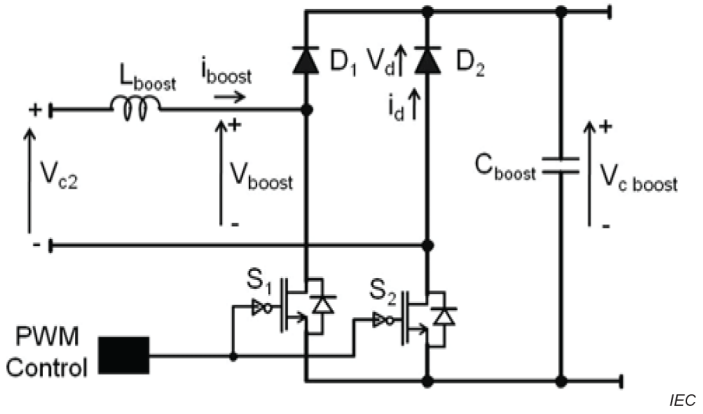

Figure 89 – Description of the converter of the boost PFC converter, including its AC/DC rectifier

In that case, the PFC (power factor corrector) boost converter has been represented with its diodes and IGBTs (insulated-gate bipolar transistors), including the PWM (pulse width modulation) and the regulation. The electronic elementary components have been modeled with their i_d (V_d) saturation curve as described in Figure 90.

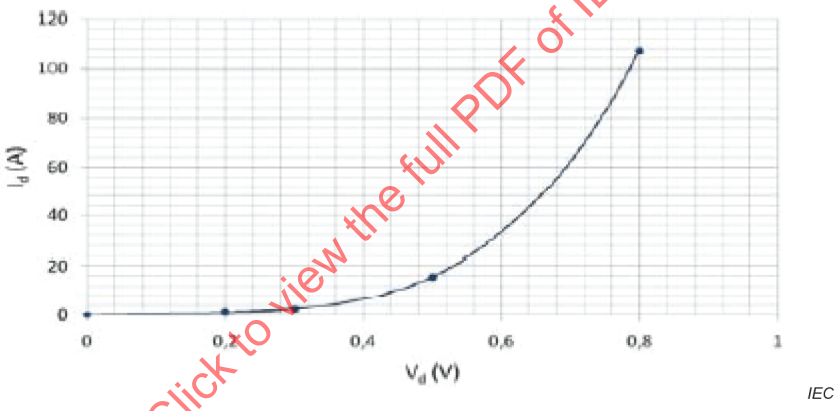

Figure 90 – Current i_d flowing in the electronic components (diodes, IGBTs) versus positive values of the applied voltage V_d

7.3.3 Determination of the voltage at the entrance of the charger, for different impedance values of the upstream network

Simulations have been performed with the EMTP-RV program, considering only one charger connected to the distribution network under steady state conditions. In the case of Figure 91 a), the impedance of the upstream network has a low value corresponding to strong networks, typically for inductances having values ranging between 100 µH to 300 µH, which means short-circuit powers ranging between 30 kVA and a few hundred kVA.

There is a transition for a value of 475 µH in this case, as shown in Figure 91 b), where a change in the solution appears; the voltage at the entrance of the charger is no longer sinusoidal. This corresponds to a bifurcation [8],[33] from a sinusoidal solution to a less stable one, as shown in Figure 91.

Figure 91 gives the voltage V_c at the entrance of the charger, the inductive part of the upstream network being respectively 200 µH in a), 450 µH in b) and 750 µH in c) (wave shape and zoom on it in d)):

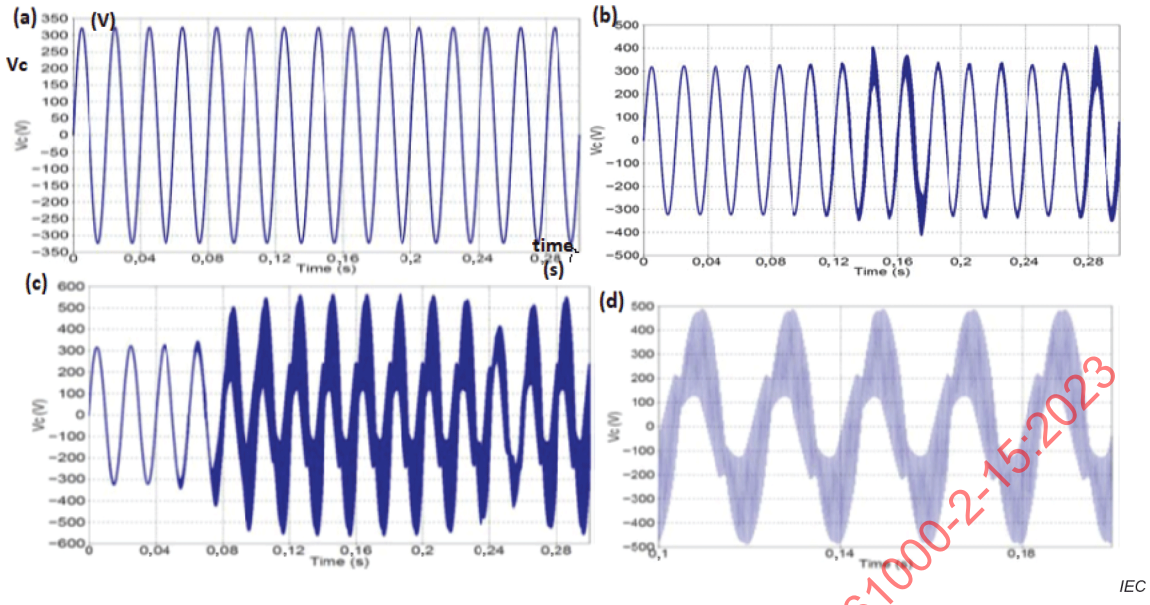

Figure 91 – Voltage V_c at the entrance of the charger, obtained by simulations, for different values of the upstream network

The case in Figure 91 a) corresponds to a strong upstream network, with a low value of the upstream impedance, while the cases b) and c) correspond to weaker ones. Simulations have been performed, Figure 91 giving the phase-to-ground voltage V_c at the entrance of the charger, with a zoom in Figure 91 d). There is a very good match between the simulations and the tests performed, see 7.3.4.

In addition to time domain simulations, phase-space diagrams can give also additional information, which is useful when non-linear aspects are raised. The phase space diagram [34] describes the state variables of the system in 3D, as illustrated in Figure 92; it is constituted by circles in the case of regular sinusoidal variables.

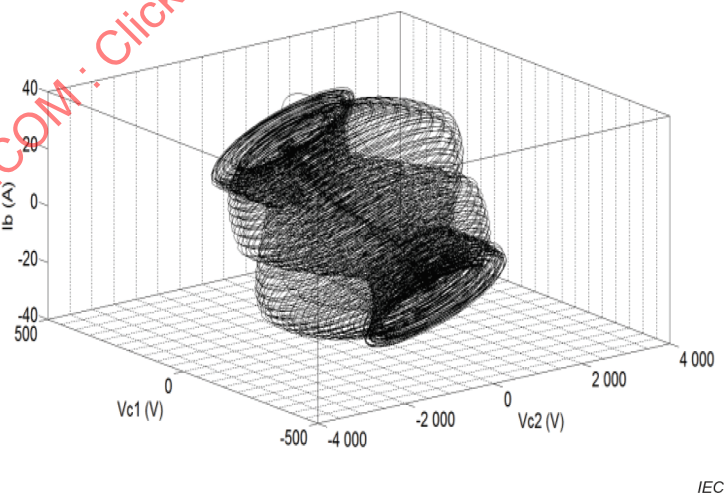

Figure 92 – Description of the phase-space diagram corresponding to the main state-variables of the system

In fact, those phenomena can appear when the upstream network is very weak, or when the equivalent (R, L, and C) upstream network forces the converter to operate in its non-linear region, as specified in [43] to [48].

Figure 93 also gives the current crossing an IGBT of the power electronics:

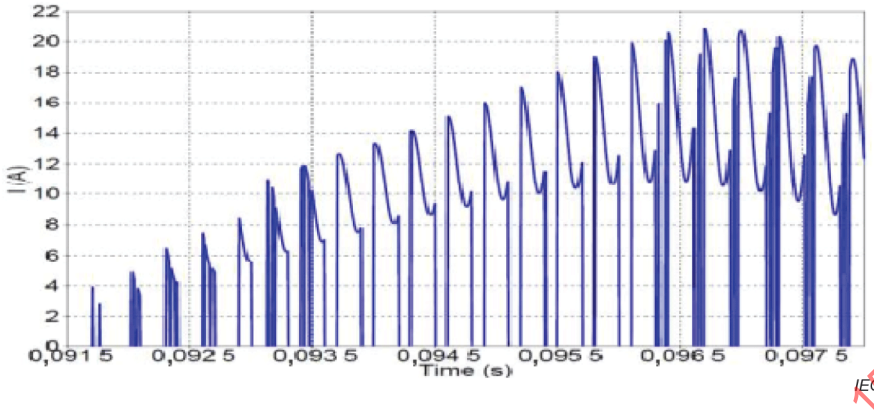

Figure 93 – Current crossing an IGBT obtained by simulations, with an inductance value of 600 µH for the upstream network

While the current remains regular in normal steady-state operations conditions, which is also the case of the PWM signal, it shows in Figure 93 a highly chaotic behaviour in the electronic components, despite a more regular voltage, as described in Figure 91 d), at the terminals of the charger. In fact, as this current is a parameter for the PWM block, a more erratic behaviour of the current also has an impact on the PWM.

7.3.4 Measurements performed at the manufacturer's laboratory

On-site tests have been performed by the manufacturer in a laboratory in [33], under the same operating conditions, for example with the same upstream network impedance. Figure 94 gives the voltage V_c at the entrance of the charger under the steady state conditions:

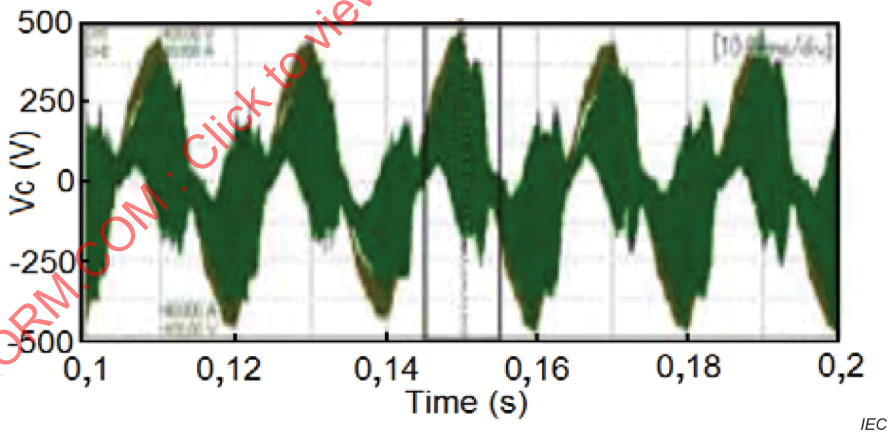

Figure 94 – Voltage V_{cmeas} at the entrance of the charger, measured at the manufacturer's laboratory, for a value of 750 µH for the inductance of the upstream network

There is a very good match between the simulations described in Figure 91 and the tests performed at the manufacturer's laboratory.

It can be noted that the modeling in this case is rather different from the one described in Clause 4 and Clause 5, as it is more focused on the behaviour between the equipment and the grid, with stronger interactions caused by the non-linearity present in the system. The question is less the modeling of the upstream network, the determination of the poles of the upstream impedance Z and the levels of harmonics generated by the power electronics and injected in the grid, than the stability of the whole system constituted by a linear part and a nonlinear one, having a strong influence and operated in its highly nonlinear region, that can lead, in extreme cases, to chaotic phenomena.

- Impact on the equipment

  The fact that very high overvoltages can occur at the interface between the AC/DC converter and the grid, will also lead to the fact that the protection against high overvoltages will operate. However, in some cases, as mentioned by manufacturers, the regulations can be damaged, due to excessive currents flowing in them.

- Conditions of appearance of these phenomena

  In fact, in addition to that, the question raised, which is a quite difficult one, is the “entropy” of the system, which means that the system receives a small amount of energy, as in the case presented here and dissipates a small amount too through the losses generated in the circuit. As soon as an oscillatory circuit exists, under certain conditions, a trigger can lead to oscillations, with almost no damping, due to the low level of the losses. In fact, a sudden amplitude change of the steady state voltage, as an example, can trigger it. This aspect is also found in electrotechnics in the case of transformers' energization, where nonlinear aspects can be raised due to the magnetic saturation of the iron core of the transformer [35] to [37].

- Discussion with CIGRE WGs

  Discussions have taken place with the convenor of the CIGRE WG C4.49 [35] [38] named “Multi-frequency stability of converter-based modern power systems” in order to adopt, as much as possible, the same vocabulary for the same phenomena, which can be also encountered in HV or EHV systems, despite the fact that the areas considered are different. On the HV or EHV networks, it can concern the connection of large offshore windfarms to the terrestrial grid through an HVDC substation and submarine DC cables, as soon as these windfarms are distant from the shore, thus limiting the losses which could be rather high with an AC connection to the grid.

7.4 Other interactions between the grid and power converters

7.4.1 PV connected to a weak network

Three cases are considered, which correspond to cases when the solar farms are connected to weak networks or lightly loaded PV farms. The following cases are described:

- a PV–micro turbine grid interface connected to a rural grid [40];
- a PV solar farm and the chaotic behaviour of its DC/DC converters [43].

a) Solar farms associated with a micro-turbine connected to the LV grid

   The first case below describes a solar farm in combination with a micro-turbine, the electrical circuit being given by Figure 95 [37] [40].

   In this case, the solar PV arrays and the micro-turbine are connected to a rural grid, which is a rather weak network. In fact, the solar PV–micro turbine hybrid system can be used to complement the existing grid supply to improve the service and provide power when the grid is not present. The loads can be agricultural loads, lighting, fans, etc.

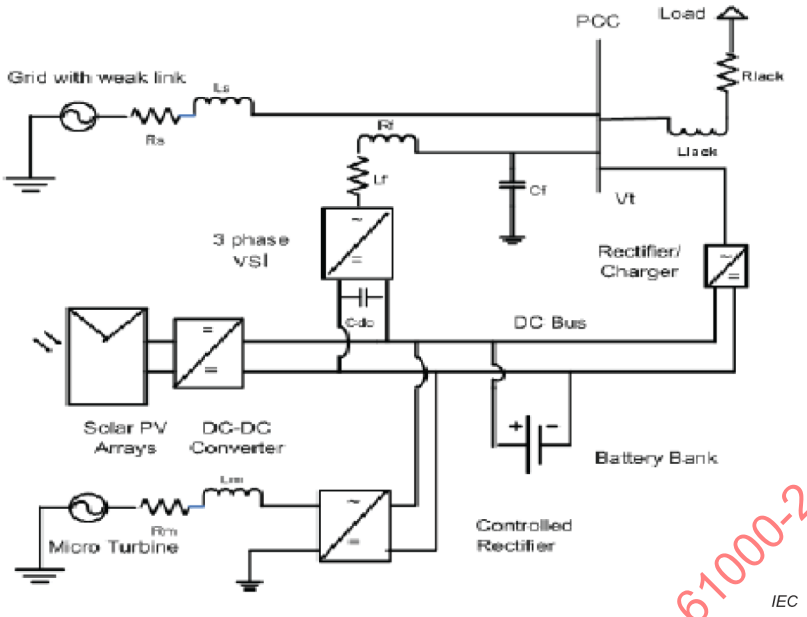

Figure 95 – Description of the circuit including a solar PV–micro turbine based power system with battery backup

The PV arrays are connected to the DC bus which is further connected to the inverter. The output of the PV arrays is assumed to be interfaced to the DC bus, through a suitable DC-DC converter stage.

When the grid feeds the loads, the PCC (point of common coupling) can be highly distorted, as described in Figure 96, because of the interactions between the loads and this weak network:

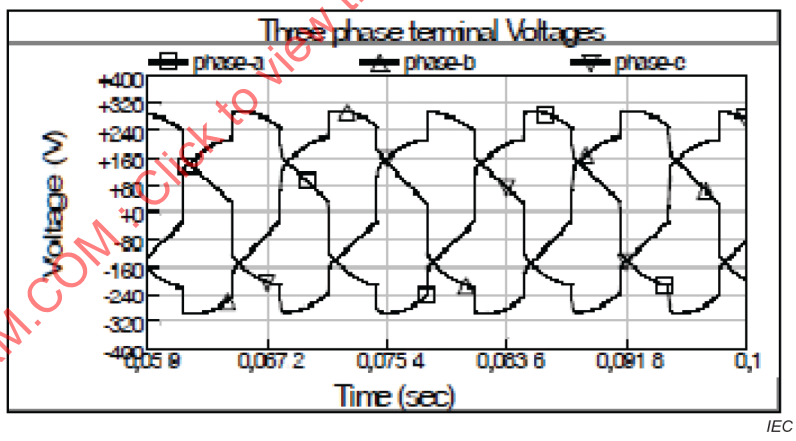

Figure 96 – PCC (grid) voltage with linear and non-linear loads in the absence of any VSI (voltage source inverter)

Figure 97 shows the case in the presence of a VSI, when the VSI is switched on after 0,5 s:

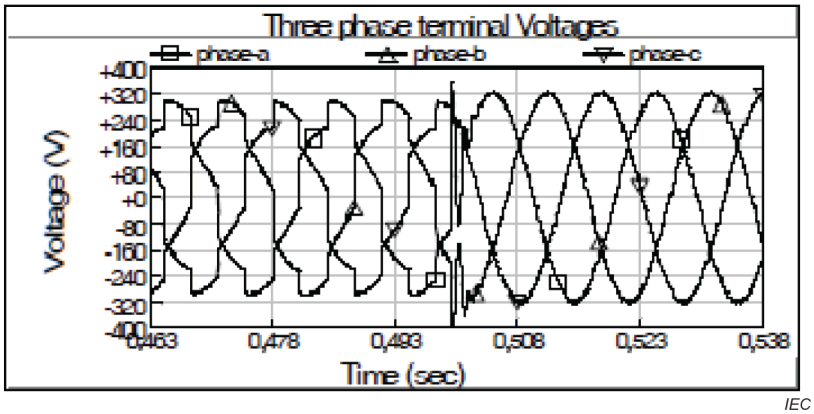

Figure 97 – Grid working and VSI switched on at t = 0,5 s

This configuration (mode 1) describes the operation mode when the grid is available and there is enough solar irradiation too during the daytime. In that case, the sliding mode control of the VSI ensures that the PCC voltage remains sinusoidal, and free from harmonics.

In fact, in that case, as the VSI does the work of converting the PV, battery and micro turbine power to AC, it appears that the PCC at the low side is higher, leading to the re-stabilization of the system or its capability to operate back in the linear region, leading to the sinusoidal shape of the voltage.

b) Stability of solar farms associated with a micro-turbine connected to a rural grid

In that case [41], the switching power converters that form the integral solar PV system turn out to be the prime source of non-linearity, with non-linear components such as diodes and IGBTs. The current voltage (I-V) properties of PV arrays exhibit a non-linear characteristic that can create phenomena that can lead to chaos in a few and extreme cases. A very large variety of different behaviours can be derived in non-linear systems, such as sub-harmonics, quasi-periodic oscillation, intermittency, and also random motion.

Reference [41] presents the stability issues of photovoltaic and wind turbine grid-connected inverters for a large set of grid impedance values. They are shown in Figure 98:

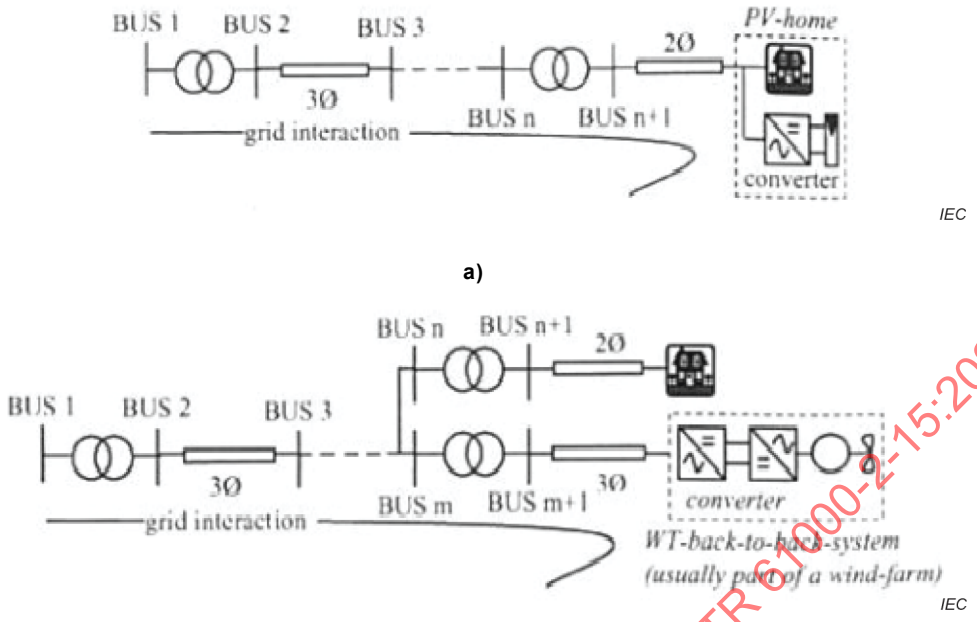

Figure 98 – Grid working and VSI switched on at t = 0,5 s

Grid impedance values can be wide ranging, as distributed generation is suited for remote areas with radial distribution plants, but they challenge the stability and the effectiveness of the LCL filter-based current controlled system.

Depending on the grid configuration, a large set of grid impedances can challenge the control of both the PV-inverter and WT-inverter and the LCL filter design in term of stability. In fact, the effect of an inductive grid reactance (long cable and low power transformers) is the decrease of the resonant frequency, as shown in Figure 99, while the effect of a capacitive reactance leads to the creation of other resonant peaks.

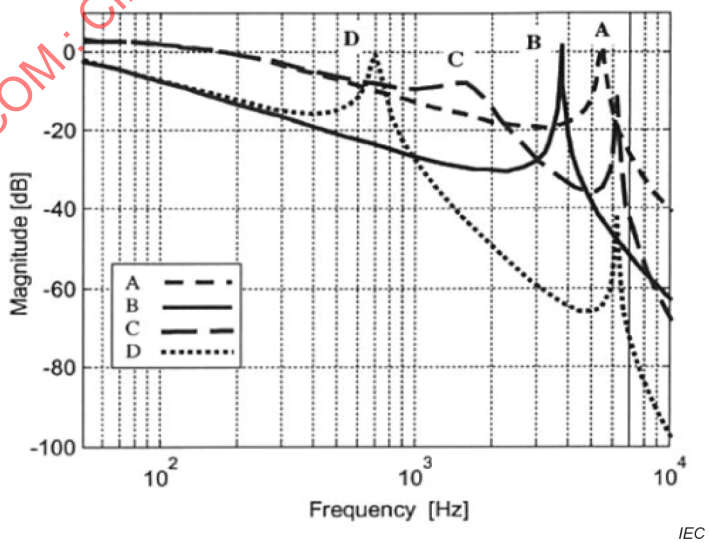

Figure 99 – Frequency characteristic of the 3 kW PV system with L-C-L filter in the following grid conditions: A) 0,1 mH, B) 3 mH, C) 0,1 mH, 100 µF and D) 3 mH, 100 µF

Two sets of parameters have been chosen, found for a 500 kW WT plant and a 3 kW plant, respectively. Figure 100 describes the resonant frequency variation in per cent of the rated resonance frequency as function of grid impedance in per cent:

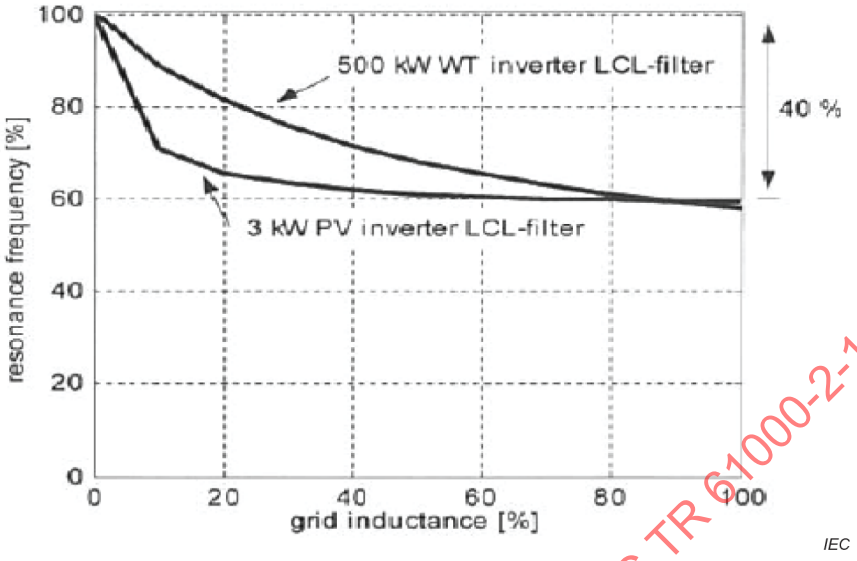

Figure 100 – Resonance frequency variation in per cent of the rated resonance frequency as a function of grid inductance in per cent

In fact, the resonant controllers have an influence mainly only on the frequency they compensate and very little on the dynamics and stability. The use of active damping can help the stabilization of the system [41].

In the case of weak networks, the system can become unstable [43]. If the controller of the PV system has been designed to work in strong grid conditions, and if the PV system is connected to a weak system, the resonant controllers can trip the overcurrent protection. In that case, active damping can be more suitable to stabilize the system considered.

c) Bifurcations and chaos in converter interfaces in solar PV systems

AC/DC and DC/DC converters can generate harmonics, supra-harmonics which are consequently injected in the nearby grid [51], and under extreme conditions chaotic phenomena as well, due to the nonlinear components such as diodes, IGBTs and feedback controls [42], [43], [44], [48], [49].

The current-voltage (I-V) properties of PV arrays exhibit a non-linear characteristic that varies under environmental conditions and can create a phenomenon called chaos [43]. In that context, a large variety of strange behaviours are also mentioned in [39]. The major traditional approaches to model the switching DC-DC converters rely on small signals analysis based on linearization and state space averaging using PWM switch model, that might not be adapted in a context of significant and large perturbations. Modelling techniques for nonlinear analysis are reported in [43].

The bifurcation diagram constitutes a power tool to investigate the nonlinear phenomena, the system being initially represented by its equations (ODEs (ordinary differential equations)), when investigating the evolution of its state variables versus time. These variables can then by plotted in 2D or 3D, constituting a space diagram, as shown also in Figure 92.

Investigations have revealed the quasi-periodic route to chaos in boost, buck-boost and load resonant converters under various operating conditions [43]. When varying the input voltage as a bifurcation parameter, the system describes the numerical and experimental results of the period doubling route that is illustrated in time in Figure 101: